Politecnico di Milano

FACOLTÀ DI SCUOLA DI INGEGNERIA INDUSTRIALE E DELL'INFORMAZIONE
Corso di Laurea Magistrale in Ingegneria Fisica

Tesi di laurea magistrale

R&D ON THE LHCb SciFi TRACKER
Characterisation of Scintillating Fibres and SiPM Photo-detectors

Relatore:
Prof. Marco Marangoni

Candidato:
Cesare Alfieri
Matricola 786638

Anno Accademico 2013-2014

R&D ON THE LHCb SciFi TRACKER. Characterisation of Scintillating Fibres and SiPM Photo-detectors

Cesare Alfieri

October 2014

Table of Contents

List of Figures

Abstract / Sommaire / Sommario

ENGLISH

During the 2-year long shut down, CERN is preparing LHC's upgrade. The instantaneous luminosity of the accelerator will pass from the previous $\mathcal{L} \approx$ 2 - 5 x $10^{32} cm^{-2} s^{1}$ to the previewed 1 - 2 x $10^{33} cm^{-2} s^{-1}$. To profit from this increased research prospective, also the CERN major experiments (ALICE, ATLAS, CMS, LHCb) entered a phase of upgrade. In particular, LHCb will substitute its tracking stations. The present detector, based on large straw detectors in the outer part and on Silicon micro-strip in the high track density region around the beam-pipe, will be substituted by a Scintillating Fibre Tracker read out by Silicon Photo-Multipliers photodetectors.
The SciFi Tracker is in a R&D phase and will be installed in the second part of 2019.
The work here presented, carried out at CERN between April 2014 and August 2014, describes the construction of the experimental equipment used to characterise different SiPMs' and fibres' technologies as well as the obtained results. The purpose was to determine the devices that best satisfy the LHCb SciFi Tracker requirements and help to decide the definitive detector's structure before the beginning of the procurement phase.

FRANÇAIS

Pendant la pause de LHC durée deux ans, au CERN on a profité de l'absence de faisceau pour apporter des améliorations et augmenter les performances de l'accélérateur. En particulier on verra la luminosité instantanée de LHC augmenter de la valeur passée $\mathcal{L} \approx$ 2 - 5 x $10^{32} cm^{-2} s^{1}$ à la nouvelle valeur attendue 1 - 2 x $10^{33} cm^{-2} s^{-1}$. Toutes les expériences principales du CERN (c'est-à-dire ALICE, ATLAS, CMS, LHCb) sont maintenant en train de se mettre à jour pour pouvoir mieux exploiter l'énergie à disposition et collectionner des nouvelles données. En particulier, LHCb aura besoin de rem-

placer l'actuel détecteur de trajectoire (désormais en obsolescence), avec un nouveau basé sur des fibres optiques scintillantes, lues par de photomultiplicateurs de Silicium. Ce projet étant assez considérable même pour le standard du CERN, il se trouve encore dans une phase de R&D, quand son installation est prévue pour la fin 2019.
Le rapport qui suit se focalise sur le travail effectué au CERN à partir d'April et terminé en Aout 2014. Il s'agit de la description des expérience construites pour la caractérisation des différentes technologies de fibres et SiPMs, de l'analyse et des commentaires sur les données collectionnées. Le but étant celui de déterminer les composants le plus adaptés pour le projet, on a aidé à faire progresser le détecteur vers sa structure définitive.

ITALIANO

Durante il lungo periodo di spegnimento di LHC durato due anni, al CERN si è approfittato della mancanza di radiazione nell'acceleratore per apportare migliorie e soprattutto aumentare tanto l'energia del centro di massa delle particelle collidenti quanto la luminosità istantanea del fascio; essa passerà dai precedenti $\mathcal{L} \approx 2$ - 5 x $10^{32} cm^{-2} s^{1}$ ai previsti 1 - 2 x $10^{33} cm^{-2} s^{-1}$. I quattro esperimenti principali del CERN (ALICE, ATLAS, CMS, LHCb), per poter beneficiare dell'accresciuta energia e raccogliere nuovi dati, sono intenti a integrare nelle loro strutture le modifiche necessarie alle mutate condizioni.
In particolare LHCb dovrà rivedere il suo sistema di rilevazione di traiettoria di particelle, sostituendo l'attuale obsolescente rivelatore (formato nella regione esterna da camere di gas ionizzante e in quella interna, più vicina alla conduttura del fascio, da strisce di Silicio) con un indicatore di posizionamento basato su fibre ottiche scintillanti lette da foto-moltiplicatori di Silicio. Attualmente il progetto si trova in piena fase di ricerca e sviluppo, essendo l'installazione prevista entro la fine del 2019.
Il lavoro di tesi qui presentato e condotto al CERN tra l'Aprile e l'Agosto 2014 verte sulla caratterizzazione di diverse tecnologie di SiPM e fibre, sulla costruzione degli apparati sperimentali necessari alle misure e sull'analisi dei dati ricavati delle misure stesse. Lo scopo essendo quello di determinare i dispositivi che meglio rispondessero alle delicate esigenze del rivelatore prima dell'inizio della fase di approvvigionamento, si è aiutato il progetto ad avvicinarsi a quella che sarà la sua forma finale.

Chapter 1

Introduction

1.1 CERN

CERN (Conseil Européen pour la Recherche Nucléaire) with an annual budget of over 1 billion Euros, with about 14000 fully, part-time and hosted employees of 113 different nationalities, with 608 representing universities and research institutes, is the most important research centre in the world for Particle Physics [1].
Established in 1954, CERN is located in the suburbs of Geneva, it crosses the Franco-Swiss borderline and counts nowadays 21 European States and Israel as Member States. CERN's function is to provide particle accelerators able to obtain extremely high energy particle beams to finally make them collide in apposite detective areas, called experiments.
The products of such collisions are detected, recorded and analysed, being the final goals on one hand to confirm by experience theoretical predictions or, on the other, to search new theoretical explanations for previously unseen phenomena and new particles through experiments.
To remember some of the most important achievements and discoveries carried out at CERN, we could mention here:

- The discovery of neutral currents (1973)
- The discovery of W and Z bosons (1983, Nobel Prize to Carlo Rubbia and Simon van der Meer in 1984)
- The determination of the number of light neutrino families (1989)
- The first creation of anti-hydrogen (1995)
- The first experimental evidence of the so-long sought Higgs Boson (2012).

Even if CERN can be considered as the greatest effort Mankind ever faced just for pure Knowledge and Science, one should underline that high technology, huge data transfer and data analysis methods required in Particle Physics and initially developed at CERN inevitably penetrated into applied research and market. The world wide web is the most resounding example: the information web that surrounds Earth and dramatically changed every aspect of our lives, was invented and firstly developed at CERN.

1.2 LHC

The LHC (Large Hadron Collider) is a circular particle accelerator built at CERN, the largest and most powerful of the world at the present day [1].
It can accelerate Hadrons (protons and heavy ions) up to 99,9999991% of the light speed and make them collide [3] with a centre of mass' energy of 8 TeV, that should rise up to 14 TeV in 2015.
LHC is 27 km long, shared between France and Switzerland and built in a tunnel that lies on average at 100m below the ground level between the Lac Léman and the Jura mountains.
The charged particle (mostly protons obtained by ionisation of Hydrogen atoms) are pre-accelerated, in the order, by a liner accelerator, a Proton Syncrotron booster, to pass afterwards in the Proton Synchrotron (PS) from which they will continue their path in the Super Proton Synchrotron (SPS). From SPS they will finally enter LHC (Fig.1.1).

Here protons are still accelerated by RF cavities and maintained in a circular trajectory through superconductive electro-magnets able to create a 8T magnetic field. The whole LHC is cooled at 1,9K by He superfluid in order to preserve superconductivity. The LHC's cryogenic system is the greatest of the world.
Inside LHC there are two vacuum tubes, each of them containing an accelerated particle beam moving in the opposite direction respect to the other. The vacuum tubes cross and provide collisions in correspondence to the 4 experimental caves where the great detectors (ATLAS, ALICE, CMS, LHCb) are situated.
LHC was built with the hope that it could answer some fundamental open questions in the basic laws of Physics. Especially data were required from such high energy particle experiments to validate the Standard Model or to shift toward the so-called Higgsless models [2]. Any further development of future theoretical Physics will so have to pass through a LHC confirmation.

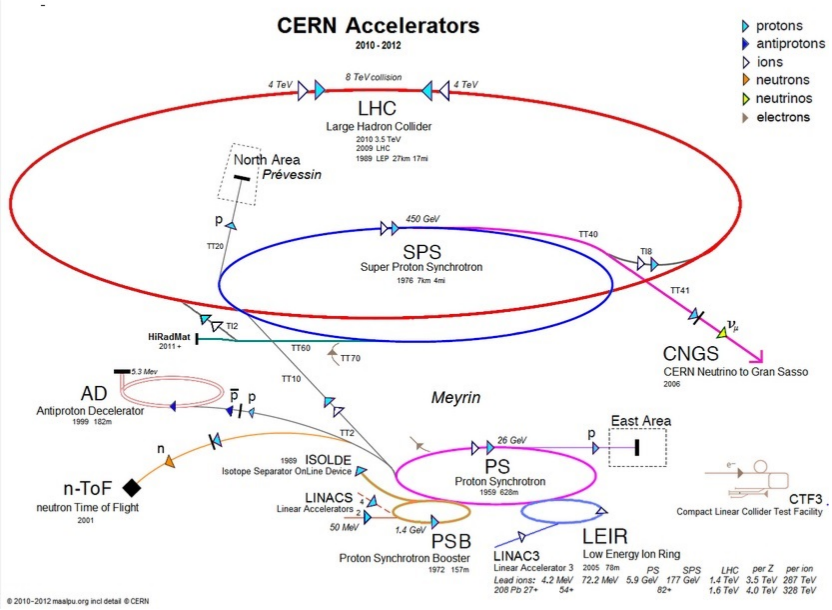

Figure 1.1: CERN accelerator system

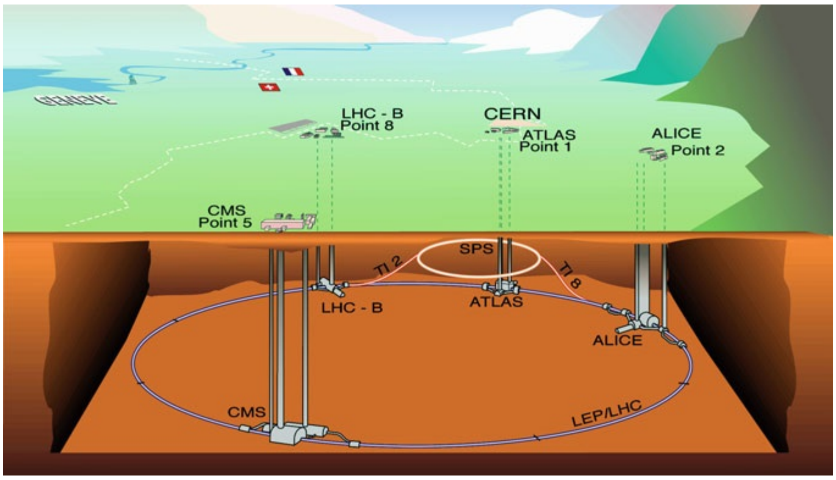

Figure 1.2: LHC and the four experimental caves: global view

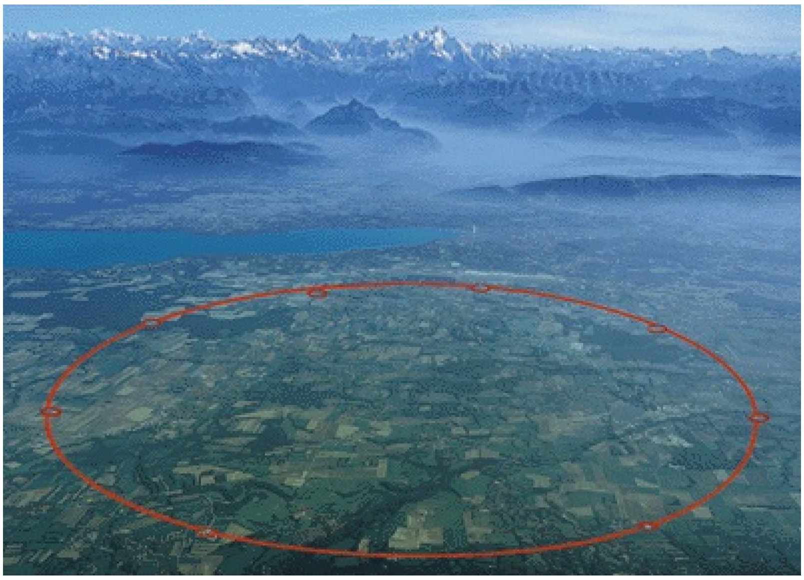

Figure 1.3: LHC with the Mont Blanc and the Lac Léman

1.3 LHCb

The LHCb (Large Hadron Collider beauty) is one of the seven experiments collecting data in the LHC at CERN [1].

The LHCb detector is a single arm forward spectrometer designed for the study of particles containing b or$c$ quarks and of the CP violation parameters [4].

The CP (Charge Parity) symmetry states that laws of Physics should stay the same when a particle is changed with its anti-particle (C symmetry) and its spatial coordinates are inverted (P symmetry). Since the known universe is made of matter instead of antimatter and it is supposed that matter and antimatter were equally generated at the very beginning, this symmetry must be imperfect. CP violation let matter prevail on antimatter in the early moments after Big Bang. In case of persistent total symmetry, there should have been total cancellation of particles and antiparticles (electron-positron, proton-antiproton etc) and Universe should have become just a sea of radiation without matter. CP violation is necessary to explain the evidence of what we daily see.

CP violation is theoretically previewed by the Standard Model since 1964 when James Cronin and Val Fitch provided rigorous demonstration of it (Nobel Prize 1980) and in 2011 a first indication of CP violation in decays of neutral D mesons was reported by the LHCb experiment.

Without entering in the complex Physics recommended to fully understand both the final purposes of LHCb and the way they can be obtained, we will now shortly describe the global structure of the detector.

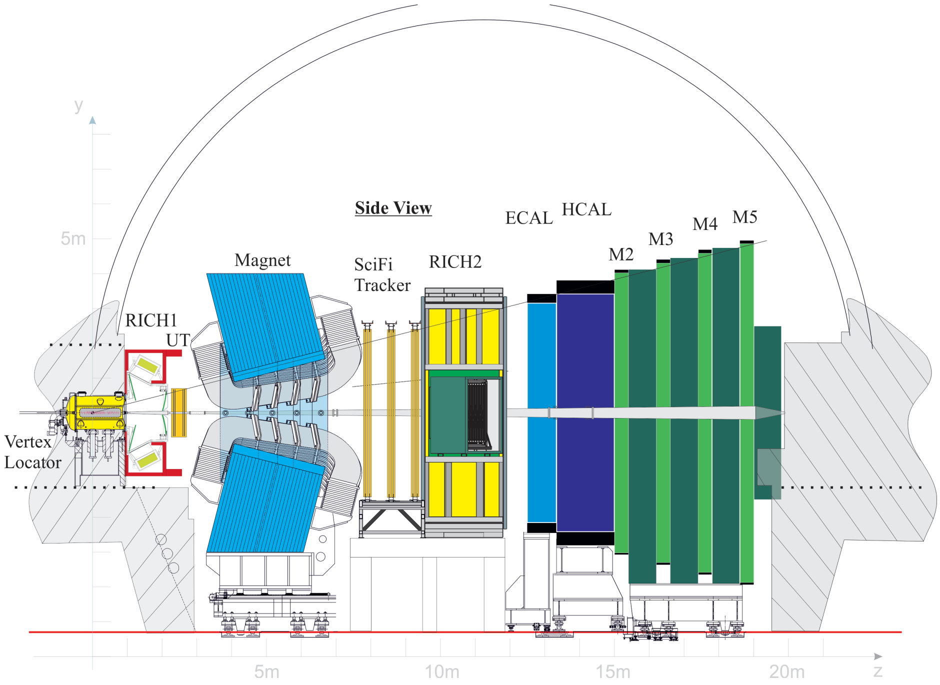

Figure 1.4: The LHCb detector

- **VELO.** The VErtex LOcator (VELO) [5] provides precise measurements of the track position in the region close to the pp collisions. Primary vertices are reconstructed using the prompt tracks coming directly from the pp interactions and, as most of the longlived b and c-hadrons decay inside the VELO instrumented volume, displaced tracks are used to identify and reconstruct their secondary vertices with good accuracy.
- **Dipole Magnet.** Charged tracks are bent in the horizontal plane with an intense magnetic field generated by a normal-conductive dipole magnet weighting 1,600 tons [6]. The LHCb magnet, shown in Fig. 1.5, provides an integrated magnetic field of 3.6Tm. It is situated between the two RICH detectors and its magnetic field profile is designed in order to minimise the residual field inside the RICH1 boxes and the VELO, while creating a field as high as possible in the region before the tracking stations.
- **Tracking Stations.** The coordinates on the transverse plane of the charged tracks are measured by five planar tracking stations located at

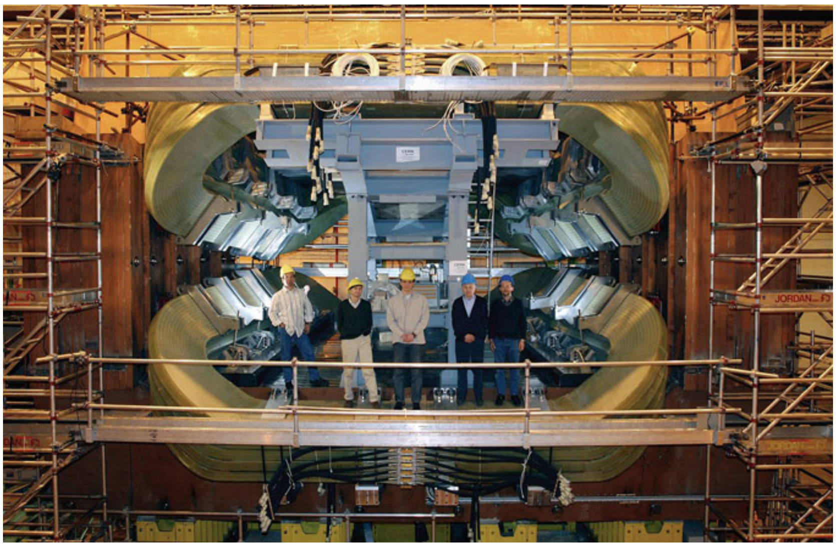

Figure 1.5: LHCb magnet

different z-positions. The first two layers (TT) are situated before the magnet, while the latter three (T1, T2, T3) after. This part will be widely described in the next chapters, as it is the fundamental subject of the report.

- **RICH.** Discrimination between charged hadrons is provided in the LHCb detector by two Ring Imaging Cherenkov detectors (RICH1 and RICH2) [7].
- **Calorimeters.** The LHCb calorimeter system composed by ECAL and HCAL (Electromagnetic CALorimeter and Hadron CALorimeter) provides measurements of the energies and transverse positions of electrons, photons and hadrons [8].
- **Muon Stations.** The muon stations are located at the end of the detector and provide efficient muon identification and triggering [9].

Chapter 2

The LHCb SciFi Tracker: Overview

The Tracking Stations provide a high precision estimate of the momentum of charged particles. This leads to a precise mass resolution for decayed particles. The reconstructed trajectories of charged particles are given as inputs to photon-ring searches in the RICH detectors which are used for particle identification. The momentum resolution is mainly limited by multiple scattering for tracks with momentum up to about 80GeV/c, while the detector resolution is the limiting factor for tracks with higher momentum. This chapter describes the upgrade of the tracking detectors downstream of the magnet [10].

There are three downstream tracking (T-)stations: T1, T2, T3. They were designed to provide reconstructed trajectories of the charged particles passing through them with a high efficiency together with high resolution in the bending plane of the magnetic field. The tracking stations of the current detector consist of two separate sub-detectors: the Outer Tracker (OT) and the Inner Tracker(IT). The OT is constructed using large straw detectors and covers around 99% of the 30m2 detector surface. The IT is a silicon micro-strip detector covering an area of 0.35m2 in the high track density region around the beam-pipe. Each station consists of four detection planes which provide measurements of the co-ordinates (x, u, v, x), with strips or straws orientated at $(0°, +5°, -5°, 0°)$ with respect to the vertical axis [10].

The design of the current tracking detectors was optimised to provide the best performance in proton-proton collisions at a centre-of-mass energy of 14TeV with 25 ns bunch spacing, and instantaneous luminosities in the range $\mathcal{L} \approx$ 2 - 5 x $10^{32} cm^{-2} s^{1}$. The LHCb upgrade is planned to run with an increased luminosity of 1 - 2 x $10^{33} cm^{-2} s^{-1}$ and so this part needs to be upgraded, the current detector being not able to deal with the increased luminosity [10].

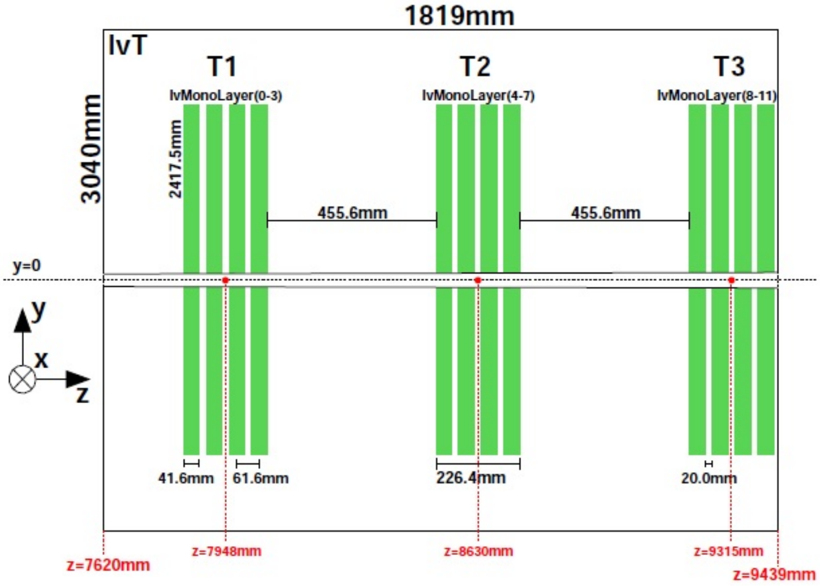

Figure 2.1: Arrangement of the SciFi tracker

The tracking stations will be replaced by a scintillating fibre tracker (SciFi Tracker/SFT) which will cover the full acceptance after the magnet. The Tracker will consist in 12 parallel "fibre walls" (3 groups of 4, in order to maintain the 12 points necessary to reconstruct a particle's trajectory), each of them formed by 12 fibre modules. The modules will have 2.5m long scintillating fibres with a diameter of 250 μm. The fibres will be read out by Silicon Photomultipliers (SiPMs) contained in Read-out Boxes at the top and bottom of the detector.

2.1 Requirements

The track reconstruction requires that the SciFi detector has high hit efficiency, good spatial resolution in the bending plane of the magnet, and low material budget in the acceptance [11].
The LHCb upgrade requires that the read-out electronics operate with 40MHz sampling frequency. The detector must be able to operate for the full lifetime of the upgraded LHCb detector to ensure that the performance of the track reconstruction is good enough for the duration of the experiment.

2.1.1 Detector performance

The main requirements on the upgraded tracking detector are given below:

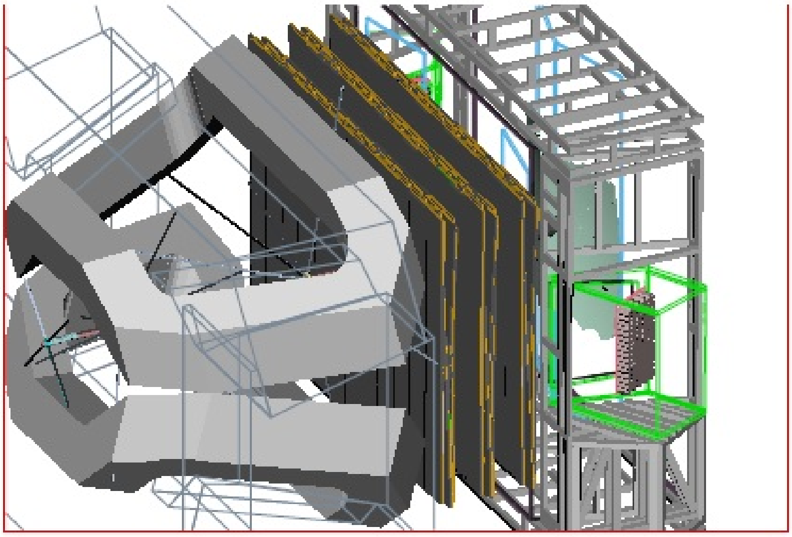

Figure 2.2: The three stations of the scintillating fibre tracker shown between the dipole magnet on the left and RICH2 on the right.

- The hit detection efficiency should be as large as possible ($\approx$ 99%), while keeping the reconstructed noise cluster rate at any location of the detector below ($<$ 10%) the signal rate at that same location.

- The single-hit spatial resolution in the bending plane of the magnet must be less than or equal to 100 μm. A better resolution is not needed as the extrapolation of tracks from the VELO would be dominated by the effect of multiple scattering in the detectors upstream of the magnet.

- The material in the acceptance region should be minimised such that the effect of multiple scattering in the tracker are smaller than those due to the material upstream of the magnet. This requirement is achieved when the radiation length is such that X=X0 $\approx$ 1% per detection layer.

- The read-out electronics should be able to run at a frequency of 40MHz, and the recovery time of the read-out channels should be short to minimise inefficiency due to dead-time.

- The detector should be able to operate with the required performance for an integrated luminosity up to 50 fb^{-1}.

	Inner Tracker		Outer Tracker	
	$z_{min}(cm)$	$z_{max}(cm)$	$z_{min}(cm)$	$z_{max}(cm)$
T1	767.3	782.8	783.8	803.8
T2	836	851.5	852.5	872.5
T3	905.0	920.5	921.5	941.5

Table 2.1: Nominal z-position of the current tracking stations

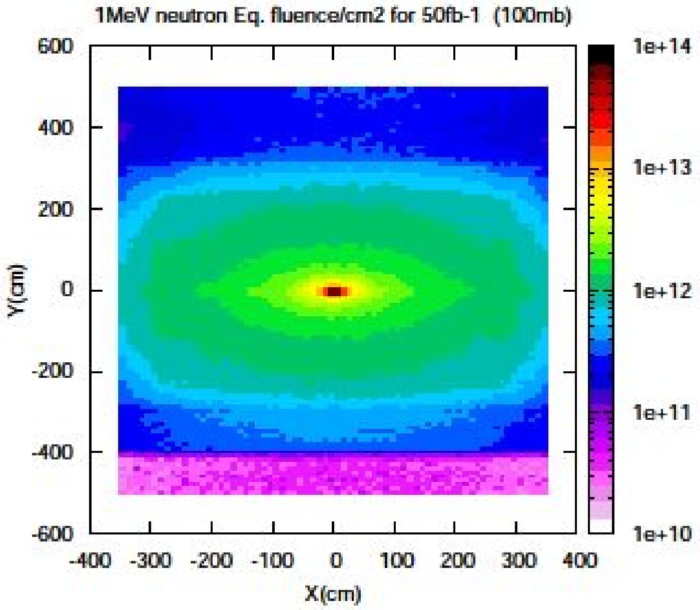

Figure 2.3: Neutron Fluence

2.1.2 Geometry constraints

Since the current detector has three tracking stations placed at equidistant positions along the beam-line between the LHCb magnet and RICH2 (the nominal z positions are listed in Table 2.1) the space available for the SciFi Tracker is constrained in the z-axis (that is also the beam axis) by that currently used by the IT and OT. If this on one hand a constraint, on the other it gives the possibility to reuse the current supporting structure [11].
The fibres must be straight and aligned within 50-100 μm in the x-direction, and the detection layers should be at within 300 μm in the z-direction, to ensure that the requirements on the resolution can be satisfied. This corresponds to a challenging work, considering the great dimensions of the entire detector.

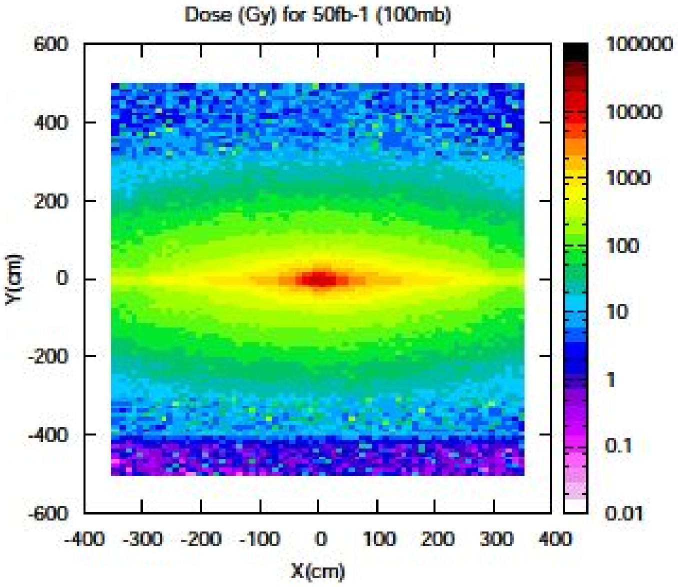

Figure 2.4: Dose: FLUKA simulation

2.1.3 Radiation environment

The radiation level expected at the tracker stations will be a major issue both for fibres and SiPMs. Fibres will experiment different doses, being radiation stronger in the region near the beam pipe and lower when one comes closer to the SiPMs. An important part of this master thesis work will be the investigation of how those devices answer to radiation damage in respect to the dose. Radiation doses have been accurately estimated through FLUKA simulation [12, 13].

The simulation was made using the latest version of the detector geometry for the expected upgrade conditions at $\sqrt{s}$ = 14TeV assuming an integrated luminosity of 50 fb^{-1} and a proton-proton cross-section of 100mb [14].
The estimated 1-MeV neutron-equivalent fluence in T1 (z = 783 cm) is shown in Fig.2.3, and the dose is shown in Fig.2.4 . The expected fluence and dose were also estimated for T3 (z = 920 cm). The maximum fluence at the position of the SiPMs (y = ±250 cm) after an integrated luminosity of 50 fb^{-1}1 is estimated to be 9.5 x 10^{11} n$_{eq}/cm^2$ and 13 x 10^{11} n$_{eq}/cm^2$ for T1 and T3 respectively. This corresponds to an integrated ionising dose in the SiPMs of 40Gy in T1 and 80Gy in T3. The peak dose absorbed in the fibres is expected to be around 35 kGy and 25 kGy at T1 and T3, respectively. The simulations also showed that a technically feasible shielding, constructed from Polyethylene with 5% Boron, can reduce the neutron fluence in the region of

the SiPMs by at least a factor of two [11].

2.2 Geometrical description

Considered the detector's dimensions (6m x 5m in X-Y plane), and the difficulties to carry voluminous objects in the LHCb cave, modularity has been adopted to realise the SciFi tracker.
In this section we will explain how the fibres will be arranged. We know that the SciFi tracker, due to geometry constraints, will consist of 3 tracking stations. Every tracking station is made of 4 detection layers, each of them subdivided of 24 submodules. Inside every module we will find 4 fibre mats. The final geometry is complicated and still in a non-definitive development phase, but we will anyway try to enter in a more detailed description of the layers' structure and fibres' arrangement [15].

2.2.1 Detection Layer and Module's Design

The tracker is made of 12 detection layers (3 groups of 4). They don't present all the same orientation in the XY plane. Stereoangles are previewed in order to achieve some resolution (lower than the more important and required X-resolution) in the Y direction. Stereoangles corresponding to the 4 detection layers of a station are respectively $0°, -5°, +5°, 0°$ (see Fig.2.5).
Each layer is 5m high and subdivided 12 modules of full height and ≈ 50cm width (see Fig.2.6). Every module is divided into a submodule of 2.5m high. It was decided to halve the height because of the breaking risks one meets handling big objects made of fragile thin plastic scintillating fibres. Every submodule ends with a mirror in correspondence to the central region (at

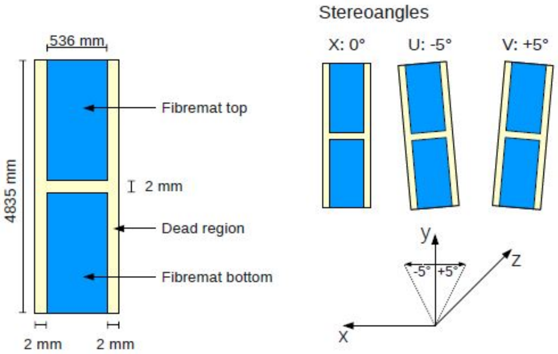

Figure 2.5: Stereoangles

the same Y of the beam pipe, y=0) and, at the other end, with and end-piece that provides correct coupling between fibres and SiPMs. The mirror is precious: we don't want to loose scintillated photons propagating in the direction opposite to detection.

Every fibre module isn't made by one single fibre layer, but by 5 of 6.

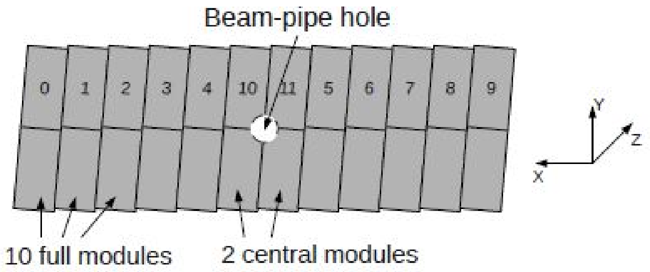

Figure 2.6: A complete Detection Layer, made out of 24 submodules. The central module preview a hole to let the beam pipe pass through. In order not to interfere with the beam and, even worse, to damage the pipe, the detector shall never come closer than 2 cm to the pipe.

The final number is still to be decided: probably 6 for the central modules near the beam pipe, where we have more frequent events, 5 for the others. Multiple fibre layers are designed to achieve a more confident distribution in the particle trajectory. From every detection layer (i.e. 5 or six fibre layers) one wants to extract just one single hit point with the highest precision (Fig. 2.8).

The multi-fibre layer is called *fibre mat* (Fig. 2.7). The scintillating fibre mats form the active component of the SciFi Tracker. Fibres in mats are embedded in an epoxy glue and arranged with extreme precision.

How to build and how to check the quality of a fibre mat is a complicated and still open issue; many requirements shall be satisfied such as maximum occupancy (reduce to the minimum the blind inter-fibre region), no missing or extra fibres in the mat, no inhomogeneity nowhere in the mat. To fulfil such constraints it is not only necessary to build a precise machine able to assemble the mat properly, but one has to be sure that fibres are geometrically perfect [16]. A bump in the fibre profile that locally increase the fibre diameter up to 0.3-0.35mm (not infrequent) would completely destroy the entire mat geometry. Diameter will be controlled for every fibre, metre by metre, with a laser based machine to localise bumps and cut them away during the mat production.

Mats are ≈ 130mm wide: we understand now that there will be 4 mats inside each module.

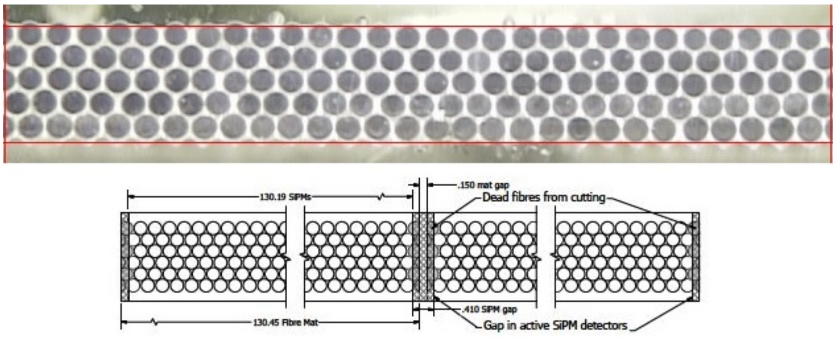

Figure 2.7: Example of Fibre Mat. At the connection of one mat to the its neighbour, some cut and blind fibres are unavoidable

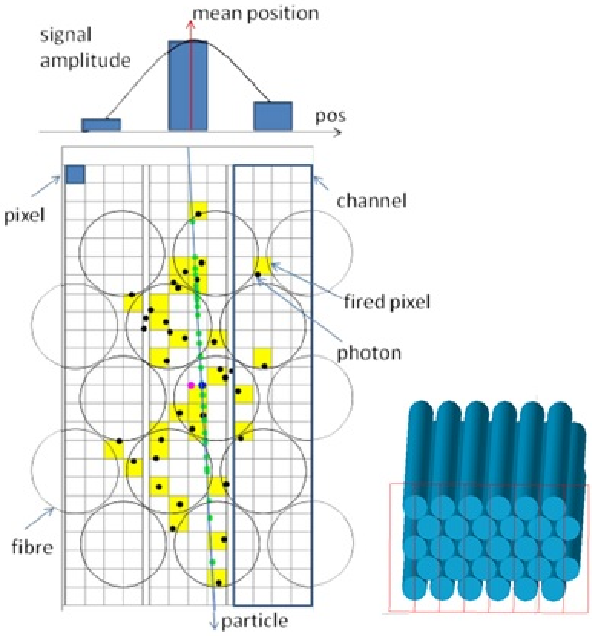

Figure 2.8: A particle passing through a detection layer: the produced photons are propagating inside the fibre and arrive to the SiPM. 3 SiPM channels are here represented. Every channel is made of many pixels, with the exact number depending on the technology and on the producing factory (not yet definitely chosen). The read out from the SiPMs is made on a channel base.

Chapter 3

Silicon Photo-Multipliers

The scintillation process, as we will see in the chapter specifically dedicated to SciFi, is not extremely efficient. In addition, just a small part of the produced light can be trapped by the fibre. This light is attenuated during propagation inside the fibre. An optimistic prevision forecasts that 10-15 photons per event finally arrive at the fibre end, without still considering coupling and internal losses with the detector that follows. One drives the conclusion that, for the LHCb SciFi tracker, a device able to detect a single photon is more than desired if we want to assure a reliable read-out for the fibre's signal.

A PIN photodiode, even with its good quantum efficiency, is not the good solution because of its unitary gain (1 photon = 1 electron); an Avalanche Photo-Diode (APD) operating in conventional mode can provide higher gain, in the order of 100. This is still too low and in APDs noise is increasing with gain. A photomultiplier vacuum tube could be a nice solution since it provides both extremely high gain (10^6) and low noise (some hundreds Hertz or lower of Dark Count Rate) but on the other hand it has low quantum efficiency, it is space demanding (not possible to use 1 PMT to read out every single fibre) and even the cost is unaffordable (hundreds Euros for one PMT). The only solution left is to use a new technology device called Silicon Photo-Multiplier.

SIPM: Working Principle

Silicon photomultipliers (SiPMs) are solid state photon detection devices that combine all of the features necessary for the photon detection of a high resolution scintillating fibre tracker [22]. SiPMs are made of arrays of parallel connected micro avalanche photodiodes with a quenching resistor [18, 20]. These APDs are operating in Geiger mode, so to say with reversed bias voltage over the breakdown value and in a full discharge regime with high internal gain. In this case a series quenching resistor (in the order of 500kΩ) becomes necessary to produce the voltage drop, a quenching for the avalanche current and to recover the cell after discharge. A smaller resistor ($\approx$kΩ) in series to the APD gives the fast shape of the discharge signal(see Fig.3.1).

Every APD microcell operating in Geiger mode must be considered as a digital detector since once the avalanche is triggered we loose the information on the number of photons that triggered it. The complete discharge of one fired pixel is in fact always equal at a fixed bias voltage and independent of the incoming light intensity. Though, a SiPM can be considered a quasi-analog device thanks to a final signal that is the sum of single APDs signals; light intensity information is generated by the internal superposition of signals coming from all fired microcells.

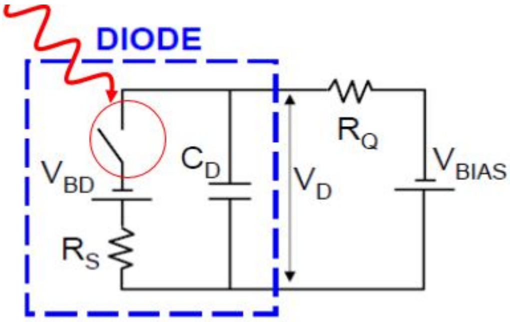

Figure 3.1: SiPM: the equivalent circuit is made of an interrupter which is closed when a photon arrives, a capacitor that represents the accumulated charge which will generate the current during discharge, a series resistor and a quenching resistor. Bias voltage is high and negative

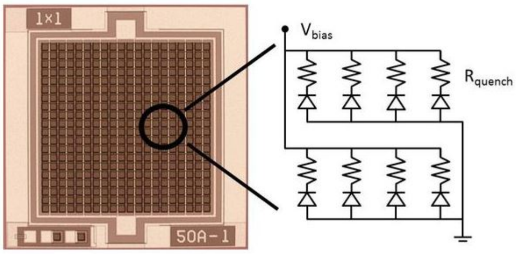

Figure 3.2: The SiPM is made of parallel APDs. If two of them are triggered by an incoming photon, we observe two times the current and, through the quenching resistor, two times the voltage signal. The SiPM is a quasi-analog device

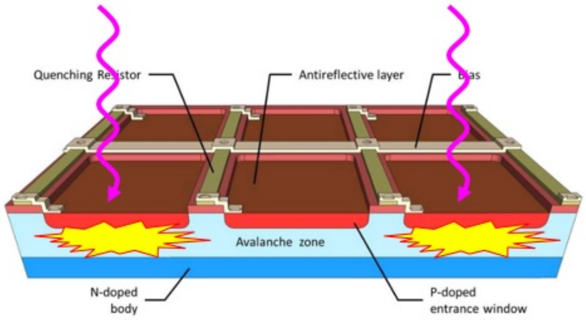

Figure 3.3: SiPM: Structure

Construction Process and Signal Shape

Silicon Photomultipliers are based on a P-on-N structure: A narrow, highly P-doped region on top of a low N-doped common silicon body is forming the entrance window for the incoming light (Fig.3.3) [18].

For this structure nearly all avalanche breakdowns are triggered by electrons. Due to the higher ionization coefficients for electrons the silicon P-on-N structure has a higher Geiger efficiency compared to a N-on-P structure. In addition, the dead layer of the PN-junction and the geometrical fill factor of the microcell have been continuously improved over the last years [18].
The quenching resistor of a KETEK Silicon Photomultiplier is formed by a doped polysilicon strip line embedded in an insulating matrix. The resistivity can be precisely adjusted in a range starting from 100 kΩ up to several MΩ. A high quenching resistor makes the device more robust and stable but at the same time the SiPM becomes slower during the recovery phase: the charge is accumulating in the capacitor represented by the depleted region with a time constant proportional to RC. A good trade off valuer stays between 0.2 and 0.8 MΩ [18], which means, with a capacitance C_D in the order of 10-20nF, a time constant:

$$\tau_L = R_Q * C_D \approx 10ns \tag{3.1}$$

characterising the second slow part of the signal shape (Fig. 3.4) produced by a triggered cell.
The first and faster part is on the contrary dominated by a different and time constant. If we consider that the resistor R_S is in the order of 1-10 kΩin first approximation the time constant is given by the product:

$$\tau_S = R_S * C_D \approx< 1ns \tag{3.2}$$

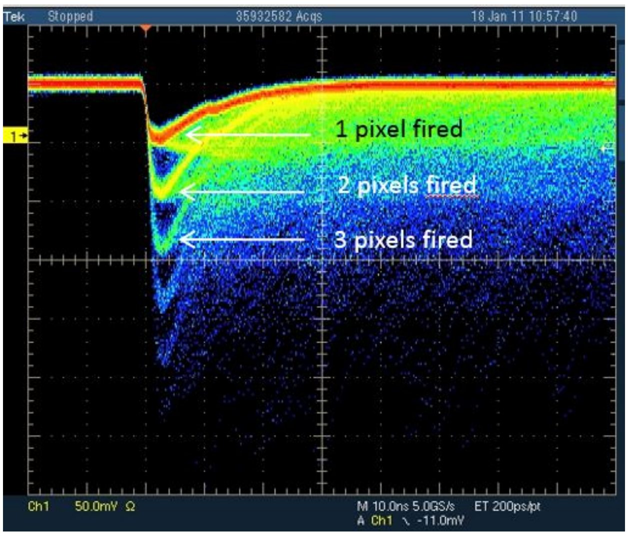

Figure 3.4: SiPM: characteristic signal shape. One can appreciate the quasi-analog signal produced by the device

which explains the extremely and almost immediate response of the device after a photon absorption.

The sensitive entrance window of the light PN-junction is coated with an anti-reflective layer with maximum transmission for blue light to avoid any reflection light losses at the interface.

Manifacturers

Two SiPM manufacturers, Hamamatsu [19] and KETEK [17], have developed dedicated devices for the SciFi Tracker. These custom devices provide high reliability due to their simple mechanical construction and a high density multi-channel package. SiPMs' cost is low enough to make the construction of a large area tracking device affordable. The main challenging requirements demanded to the photo-detector are represented by the neutron radiation environment and the low light output of the long scintillating fibres.

The development of customised devices is required to adapt the dimensions of the detector's channels to the SciFi Tracker geometry and to insert SiPMs in a packaging suitable for low temperature operation. The imposed geometry should preview:

- 64-channel SiPMs
- Channels of 0.25mm width, to respect a harmonious coupling with fibres (see Fig. 2.8).

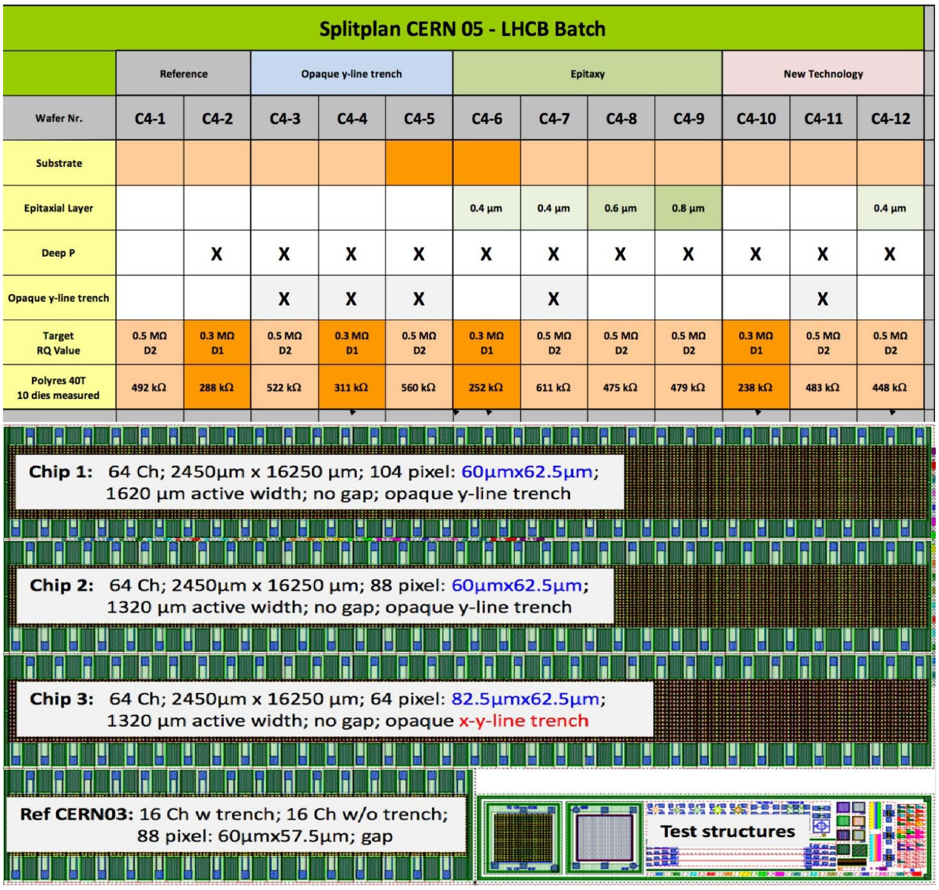

Splitplan CERN 05 - LHCB Batch

	Reference		Opaque y-line trench			Epitaxy				New Technology		
Wafer Nr.	C4-1	C4-2	C4-3	C4-4	C4-5	C4-6	C4-7	C4-8	C4-9	C4-10	C4-11	C4-12
Substrate												
Epitaxial Layer						0.4 µm	0.4 µm	0.6 µm	0.8 µm			0.4 µm
Deep P		X	X	X	X	X	X	X	X	X	X	X
Opaque y-line trench			X	X	X		X				X	
Target RQ Value	0.5 MΩ D2	0.3 MΩ D1	0.5 MΩ D2	0.3 MΩ D1	0.5 MΩ D2	0.3 MΩ D1	0.5 MΩ D2	0.5 MΩ D2	0.5 MΩ D2	0.3 MΩ D1	0.5 MΩ D2	0.5 MΩ D2
Polyres 40T 10 dies measured	492 kΩ	288 kΩ	522 kΩ	311 kΩ	560 kΩ	252 kΩ	611 kΩ	475 kΩ	479 kΩ	238 kΩ	483 kΩ	448 kΩ

Chip 1: 64 Ch; 2450µm x 16250 µm; 104 pixel: 60µmx62.5µm; 1620 µm active width; no gap; opaque y-line trench

Chip 2: 64 Ch; 2450µm x 16250 µm; 88 pixel: 60µmx62.5µm; 1320 µm active width; no gap; opaque y-line trench

Chip 3: 64 Ch; 2450µm x 16250 µm; 64 pixel: 82.5µmx62.5µm; 1320 µm active width; no gap; opaque x-y-line trench

Ref CERN03: 16 Ch w trench; 16 Ch w/o trench; 88 pixel: 60µmx57.5µm; gap

Figure 3.5: KETEK: CERN SiPMs for spring 2014

- Channels of 1.5mm height to respect a harmonious coupling with the 6-layer mat.

New devices from KETEK with the latest technological improvements implemented have become available in Spring 2014. KETEK designed for CERN a batch with chips coming from 14 wafers with different characteristics. Every wafer had 3 different SiPM designs. Finally, what has been received in Geneva and analysed in this Master work are just 7 wafers, everyone with 2 different chip designs. The received wafers are C4-1, C4-3, C4-7, C4-8, C4-9, C4-11 and C4-12. The received designs correspond to the "Chip 2" type and the "Chip 3" type (see Fig. 3.5).

Details of these new technologies, the complete analysis and characterisation of the received devices will be treated in the next section.

3.1 Characterisation at room Temperature

The SiPM characterisation at room Temperature will consider 3 main parameters in principle, that are

1. **Noise**
2. **Gain**
3. **Photo-Detection Efficiency**

3.1.1 Noise: Dark Count Rate and Cross-Talk

The price to be paid to have a powerful device able to detect single photons as SiPMs are, is to deal with their high sensitivity to noise. Noise has three major contributions for a SiPM:

1. **Dark Count Rate:** thermal/ tunnelling carrier generation in the bulk or in the surface depleted region around the junction can trigger an avalanche indistinguishable to the one produced by a real photon hit.

2. **Cross-Talk:** 10^5 carriers in an avalanche plasma emit on average 3 photons with an energy higher than 1.12 eV (A. Lacaita et al. IEEE TED 1993). We can have up to 10^7 carriers in a SiPM avalanche. These photons can trigger an avalanche in an adjacent microcell: we call this phehomenon optical crosstalk. It is the cause of the high intensity noise and reduces the possibility of determining the correct position of a passed particle (see Fig. 2.8).
   Cross-talk is a crucial issue for new devices, since it is highly increased by a higher bias Voltage, i.e. from 2V to 5V Over-Voltage (OV) that means Volts over breakdown Voltage, there were gain is highly increased too. Extremely high gain is demanded in order to detect the little amount of light fibres are delivering, but cross-talk doesn't allow to increase OV indefinitely [22].

3. **After Pulses:** during an avalanche, carriers can remain trapped for a short time in the depleted region, triggering a new avalanche once they are released again (≈100ns). This is a ghost pulse, normally of lower intensity since the capacitor didn't had the time to recharge completely. Fortunately After-pulsing has been significantly reduced for the latest technology and contributes only with a negligible fraction to the total noise. For that reason we won't analyse it specifically but, using a fast read-out, counting it directly in the DCR.

Dark Count Rate

The first measurement we performed on the new KETEK SiPM 2014 batch was Dark Count Rate. DCR measurements will allow us to draw conclusions also about Cross-Talk, Gain and Gain Linearity.
First of all the 64-channel detectors were mounted on a PCB piece, taking care about the delicate procedure of bond wiring. Since this procedure takes time and to bond 32 channels instead of 64 resulted an easier soldering issue, we decided to connect just half of the channels. Moreover, the measurement of 50% of the channels was considered more than sufficient to fully characterise the device.

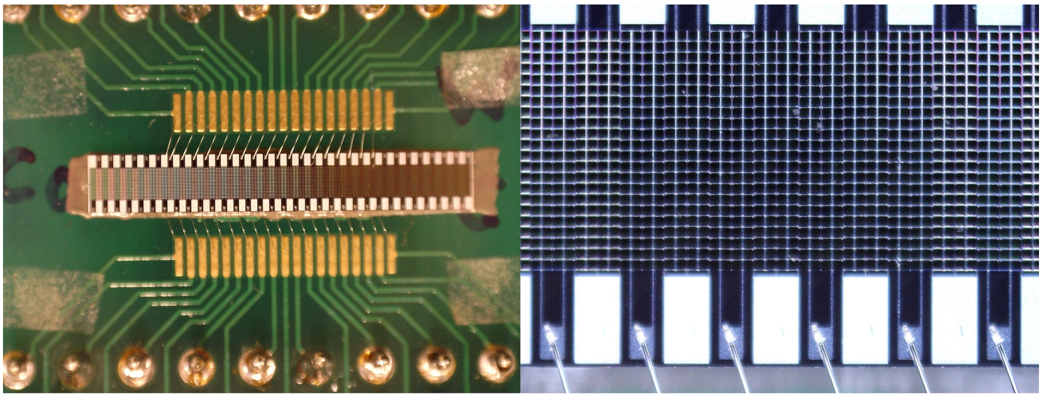

Figure 3.6: The SiPM mounted on a PCB. One can see the 32 connected channels + 2 connections for power supply. In the zoomed image one can clearly distinguish the channels and even the single pixels.

Experimental Set-up

The detector was afterwards put into a small dark box that worked both as a dark room for the SiPM and as a Faraday cage to defend us from electromagnetic noise. The dark box was covered many times with a black blanket to avoid any single photon to hit the SiPM.
The bias reversed Voltage was supplied by a pico-ammeter which was also used to read the dark current (a mean value). The voltage signal was instead read by a picoscope, a digital oscilloscope directly connected to the PC. Two capacitors were used to filter noise: the first (C_1) to avoid low frequency noise components to pollute the signal, the second (C_2), to discharge fast noise components to ground. The signal was then amplified with a fast amplifier. The equivalent electric circuit can be seen in Fig 3.7.

Experimental Parameters

To measure the DCR, we used to store with picoscope an interval of 0.1s of

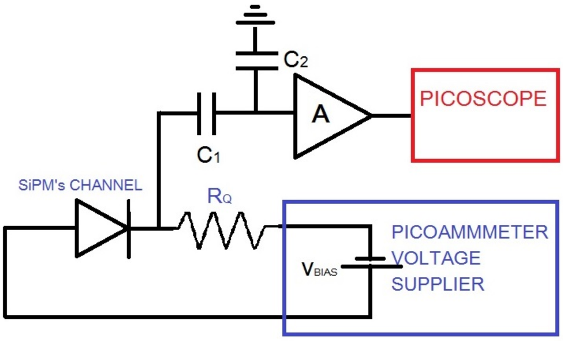

Figure 3.7: Dark Count Rate Measurement circuit

the signal's temporal trace, with a sampling time of 0.8ns. The temporal traces were captured for 4 different bias Voltage values: +2V, +3V, +4V, +5V OV. Breakdown (BD) Voltage was known through KETEK data sheet and, as we will see, since BD is Temperature dependent, Temperature was strictly controlled through a Pt 100, a Platinum thermistor.

Counting Method

A typical temporal trace is as illustrated in Fig.3.8. These kind of traces were analysed through a Matlab program appositely written and optimised for the analysis of these specific data.

Since every pulse corresponds to an avalanche provoked by dark noise, first of all the program has to identify peaks and count them. To identify a peak a simple threshold method was used: if the signal is, in absolute value, greater than a determined threshold (function of OV)for a certain number of consecutive samples, than this pulse must be counted as a dark event. Thresholds

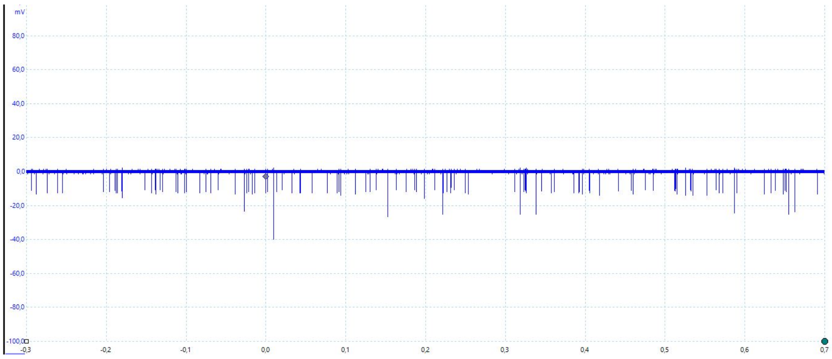

Figure 3.8: Dark Count Rate Measurement: Temporal Trace

were determined with an eye-check: they were set to the 50% of the average peak value (it is OV dependent) of an event.

In order to provide an estimation of the DCR, one can chose two different methods:

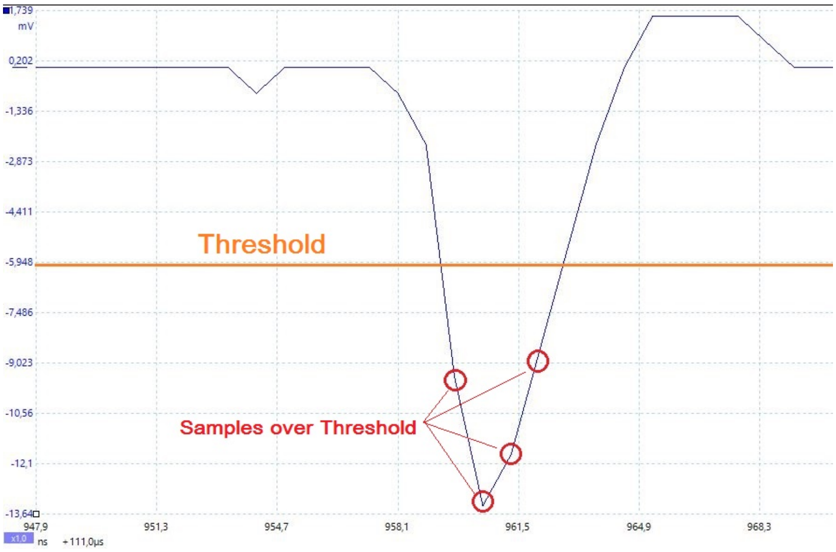

Figure 3.9: Zoom on a single event peak, Threshold method. To be considered a peak, signal must have at least 3 or 4 consecutive samples above Threshold, in order not to count large noise fluctuations

- One can count every single pulse and divide the total number by the capture time to have a first rough idea of the rate.

  $$DCR = \frac{n_{totalcounts}}{t_{measurment}} \tag{3.3}$$

  these method is simple but it doesn't provide us an idea of the temporal statistical distribution of the time interval between a dark pulse and the next.

- Another more refined method consists in counting peaks and establish their exact temporal position. Later one can find the width of the intervals that stay between them, store their value and make an average. The inverse of that average will be the dark count rate.
  That is to say, if n represents the total amount of counts and, if t_i is the temporal position of the i-th pulse:

  $$DCR = \left[\frac{1}{n}\sum_{k=1}^{n}(t_i - t_{i-1})\right]^{-1} \tag{3.4}$$

Even if the two methods give results with non remarkable differences (<1%), we preferred to use the second since it gave us also a temporal probability density of the intervals' distribution. We expected this probability density to be a decreasing exponential and so, if the histograms of the intervals could be well fitted with such a function, it meant that the measurement is statistically significant.

Results

We're not going to report here the entire set of results, since the amount of data and the readability of this document would be uselessly compromised. Just to have a quantitative idea of how many graphs were produced during this measurement, one should think that we analysed 14 chips (7 different wafers, 2 chips per wafer); every chip had 32 measured channels and every channel was measured at 4 different OV, for a total of 14 x 32 x 4 = 1792 DCR graphs. We're going so to comment just channel 1 of chip W7-3 for the 4 OVs (Fig. 3.10). This chip was chosen because it will turn out to be one of the best of the entire batch.

One can see that the exponential hypothesis for the interval probability density function is respected even if, for +2V OV, statistics starts to be low (few events) and the histogram's bins don't always correspond to a pure exponential. At low OV in fact the probability to trigger an avalanche for a thermally generated carrier is lower since the electric field in the depleted region is weaker. Even more, for lower voltages, the depleted region in the diode is spatially less extended and a carrier generated outside this region cannot trigger the avalanche mechanism. It is so not surprising to see how DCR is decreasing with a decreasing OV.

Comments on the results

It is still matter of discussion which will be the operating OV for the SiPM. As we have seen, a higher OV causes a higher DCR and, as we will see, a higher cross-talk. But it also provides a higher gain. For the moment a large part of the electronics pool in the charge is thinking to operate the SiPMs between +3V OV and +4V OV. We agree with this position and in this work, when we present global chip's results, we show data collected between +3V OV and +4V OV.

In Fig. 3.11 we present the entire chip's data concerning DCR at +3V OV. We cannot see 32 channels but just 27. Some bond-wires were damaged during handling and some other channels turned out to be non operating (short-circuited): those reasons explain the 5 missing channels.

At this R&D stage, a DCR under 100kHz is highly desirable. We know that the whole LHCb experiment is planned to read-out data with a frequency of

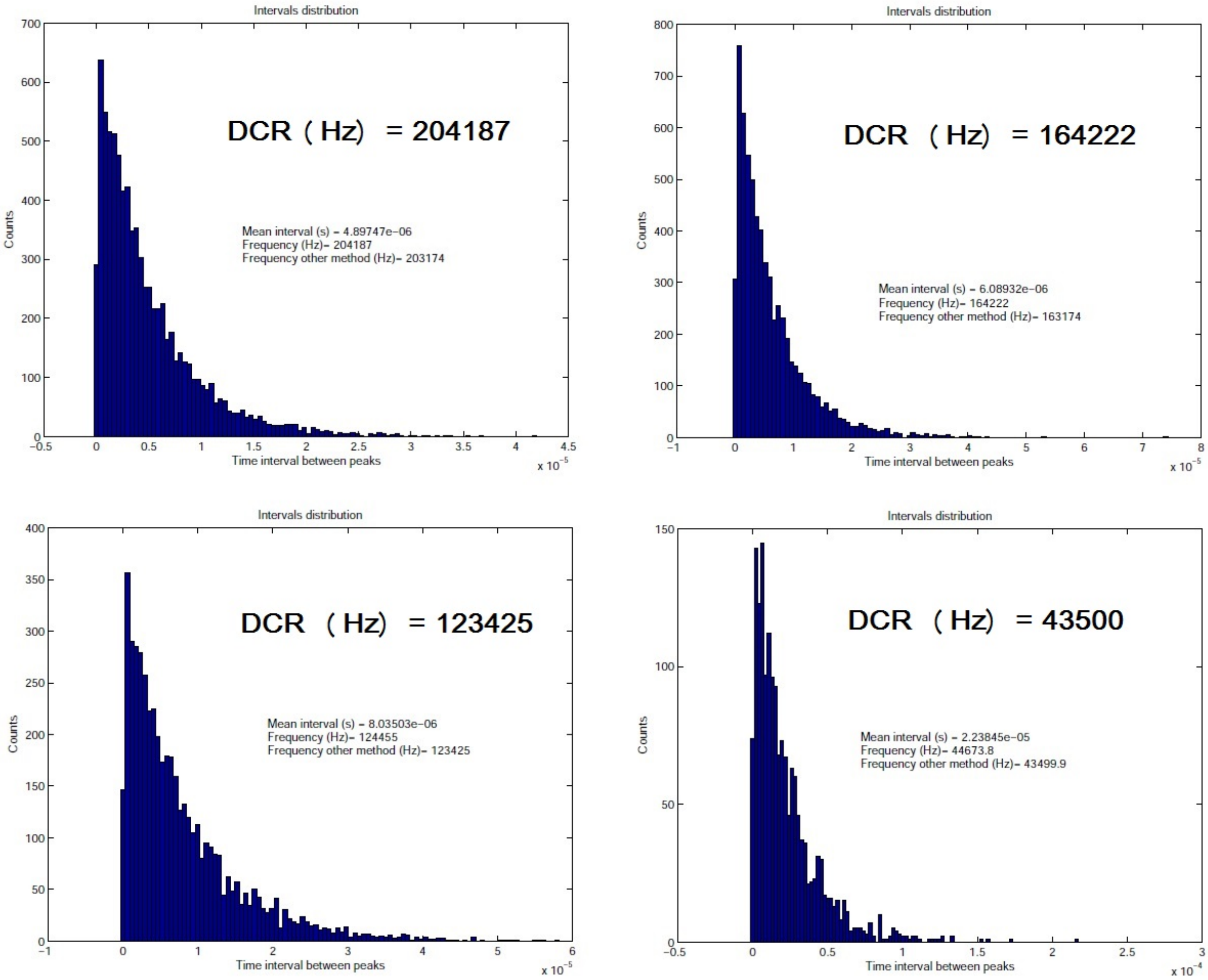

Figure 3.10: Chip W7-3, channel 1. The graphs refer respectively, from left up to right down, to 38V bias Voltage (+5V OV), 37V (+4V OV), 36V (+3V OV), 35V (+2V OV). The "other method" results for DCR refers to the simple calculation counts/time

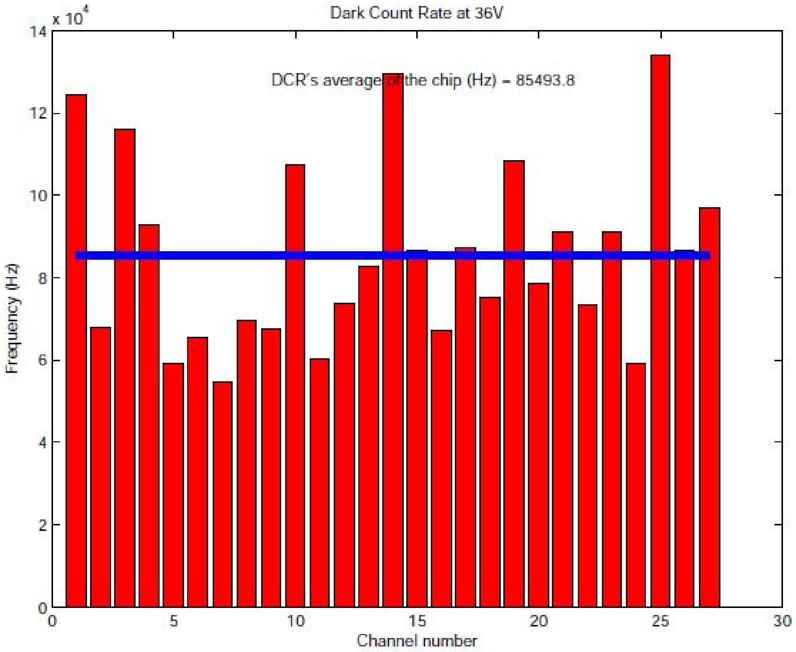

Figure 3.11: Global DCR results for chip W7-3 at 36V (+3V OV)

40MHz. This means that on average we're going to have a ghost hit due to DCR every 400 read-outs, which is acceptable. Other features such us noise cluster and SiPM cooling (to reduce thermal generation) will be implemented to increase the signal to noise ratio. On the other hand, radiation will play a fundamental role and will increase DCR: at a first extremely rough approximation, if we think that cooling and radiation will one neutralise the other, this first value at room temperature is of great importance.
For chip W7-3 we got an average of ≈ 85 kHz at +3V OV, telling us that KETEK is working properly in this direction.

Cross-Talk

We used again the same data collected in the DCR measurements to obtain information about Cross-Talk (X-Talk). This was done to optimise time both on the hardware set-up and in the software data analysis. One could remark that, if for DCR we had statistics good enough to draw significant conclusions for X-Talk we hadn't, since the double peaks were expected to be at least ten times less frequent than single peaks. This is partially true, especially for low OVs, but still numbers were good enough to let us reach important results. We used again the Threshold method to identify the so called "double events". This time Threshold was defined at 1.5 average peak value of a single event pulse. If we call N the peaks over the second Threshold, and n the single peaks, X-Talk can be defined and calculated as follows:

$$XTalk = \frac{N}{n+N} \tag{3.5}$$

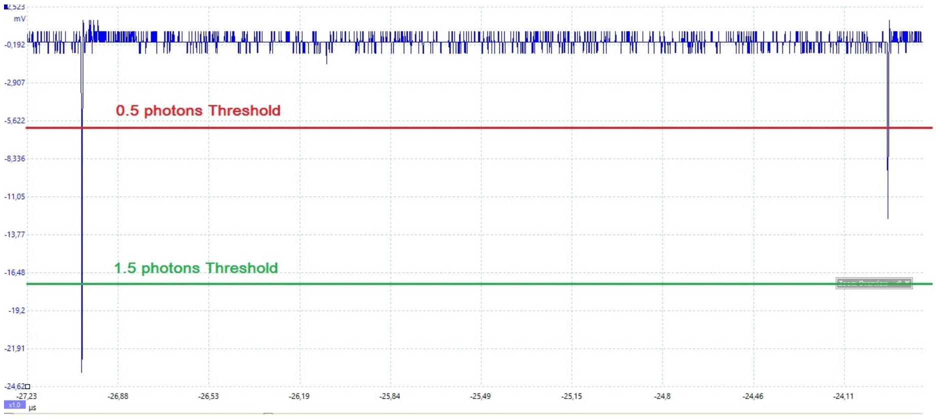

Figure 3.12: SiPM Optical X-Talk. The 1.5 photons Threshold method

New Opaque Trenches

Some words must be spent describing the new technology developed by KETEK we had to test. KETEK inserted opaque trenches between one microcell and its neighbours to avoid that photons produce by the avalanche plasma pass through and trigger another pixel. Trenches reduced dramatically X-Talk. For geometry 3 chips, trenches were present in both X-Y directions, while only Y trenches were present for chips of geometry 1 (see Fig. 3.5).

The drawback of the trench technology consists in losing spatial efficiency in the geometrical fill factor: trenches are blind and can't be detective regions for the SiPM. We will find confirmation of this effects during measurements of Photo-Detection Efficiency (PDE).

Results and comments

We will present results just from our test chip (W7-3, channel 1).

It's useful to remind now that for SiPMs produced in 2013 typical X-talk values were in the order of 5-10%. We can joyfully see how these new devices have improved their performances thanks to the integrated opaque trenches technology (Fig.3.14). One can also remark how rare have become triple events and the quite total absence of 4 and 5 simultaneously triggered microcells due to X-Talk. To confirm that trenches are the origin of this dramatic and important improvement, we can compare chip W7-2 and chip W7-3.

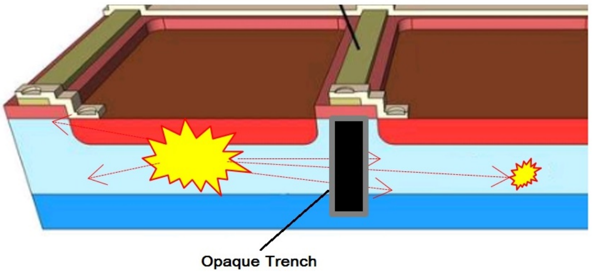

Figure 3.13: Opaque Trenches make less probable for a photon to pass from a microcell to its neighbour

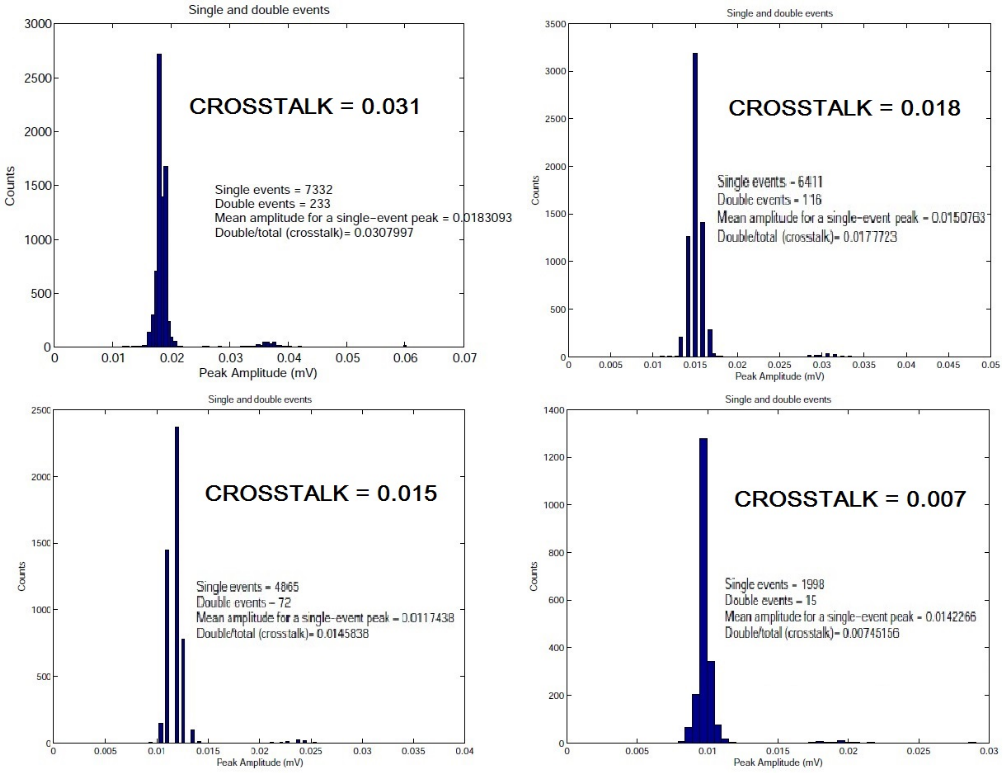

Figure 3.14: Amplitude distribution of pulses for chip W7-3, channel 1 in the dark. The graphs refer again at measurement performed at +5V OV, +4V OV, +3V OV, +2V OV.

Coming from the same wafer, they differ only in the chip's geometry and pixel size, but X-Talk is for W7-3 4 times smaller, in the order of 1.4% on average for W7-3 at +3V OV. What can be remarked as an optimum result is the ≈3% X-Talk one obtains at +5V OV: an incredible technological step forward impossible to preview in 2013.

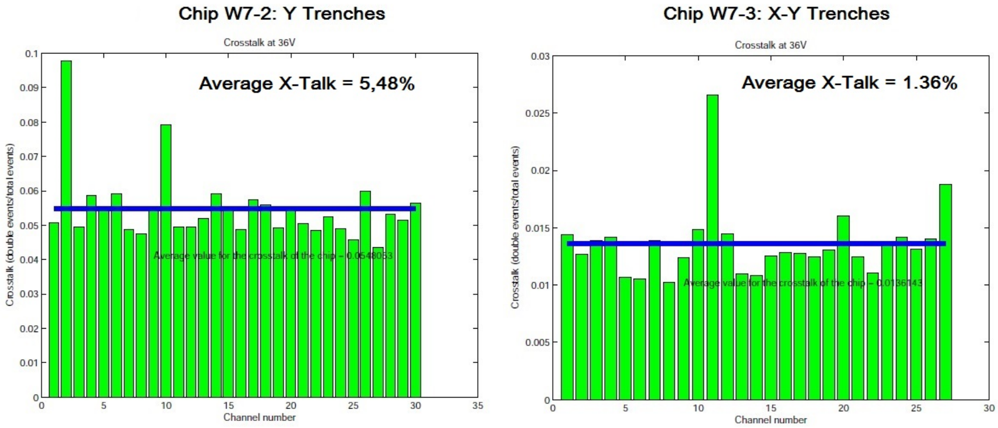

Figure 3.15: Comparison between 2 chips, one with double trenches and the other with single trenches, coming from the same wafer, at the same OV

3.1.2 Gain

Gain is a crucial parameter for a SiPM, but it is difficult to measure. It is defined as the number of electrons generated by a single photon hit.
Gain depends on the charge accumulated in the depleted region and discharged once an absorbed photon generates a carrier, which is then accelerated by the Electric Field and forms the avalanche.

$$G = \frac{Q}{e} \tag{3.6}$$

where e is the electron charge. So we can write:

$$G = \frac{(V_{bias} - V_{BD})\, C_D}{e} \tag{3.7}$$

We can model the depletion capacitance at first approximation with a simple capacitor with parallel and plane faces. Capacitance is so given by:

$$C = \epsilon_0 \epsilon_r \frac{S}{d} \tag{3.8}$$

where ϵ_0 is the electric permittivity in the vacuum and ϵ_r is the relative permittivity in Si, S is the surface and d is the width of the depleted region. From this rough model we can deduce that the more the BD Voltage is high, the smallest we expect the gain. In fact to have breakdown we need the module of the Electric Field $\vec{E}$ to reach a critical value $\vec{E}_c$, characteristic of the material. Since:

$$V_{BD} = \int_0^d \vec{E}_c(\vec{r}) \bullet d\vec{r} \tag{3.9}$$

for a capacitor with plane and parallel faces we obtain:

$$V_{BD} = \left|\vec{E}_c(\vec{r})\right| \cdot d \tag{3.10}$$

A higher width of the depleted region in the p-n junction means higher V_{BD}, but it means also smaller C and so less accumulated charge and smaller gain.

Measurement and Results

To measure gain properly one should conceive a set-up to measure C_D which would be costly in terms of time and presents difficulties.

Another simpler (and for our purposes sufficiently precise) solution is to exploit once again the DCR measurements. If one knows: dark current average value (measured through the pico-ammeter), DCR, measuring time and amplitude distribution of peaks one can reconstruct the Gain information considering that charge corresponds to the average current multiplied by the observation time interval. We assume that charge is equally divided into the counted number of events (taking into account multiple events too).

Gain can be obtained through the formula:

$$G = \frac{I_{dark} \cdot t_{meas}}{e \cdot n \cdot \frac{\langle A_{Singles} \rangle}{A_{Tot}}} \tag{3.11}$$

where n is the number of single events, $\langle A_{Singles} \rangle$ is the average amplitude of the single events and $\langle A_{Tot} \rangle$ is the total average amplitude. In this way we take account of every multiple X-Talk.

This method gave quite good results, as one can see in Fig.3.16, where Gain is plotted for every measured channel of chip W7-3 at +3V OV.

One can see how gain is homogeneous for the entire chip, respecting another important figure of merit that wants the chip not to introduce errors in determining a particle's trajectory (see Fig. 2.8). Good gain values stay around 10^6 for SiPMs. Excellent values arrive at 10^7.

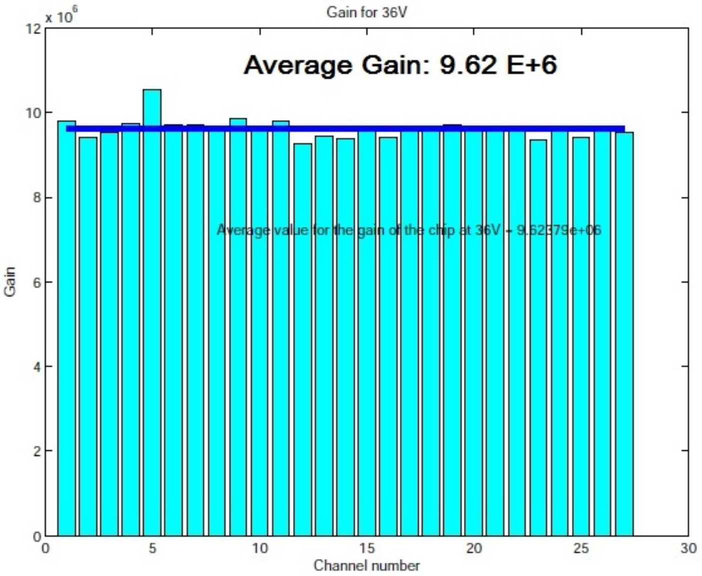

Figure 3.16: Global view over Gain for the measured channels of chip W7-3

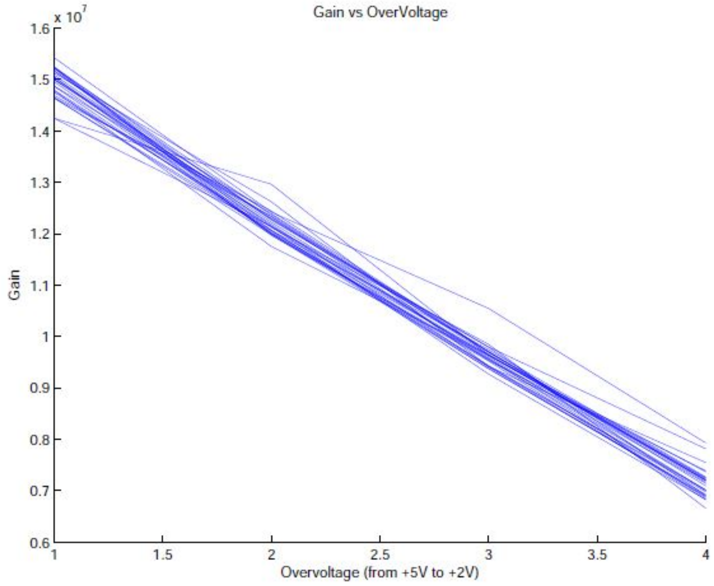

Figure 3.17: Gain(OV) for chip W7-3. We see here all the masured channels superposed together. We appreciate the linear behaviour, similar for every channel in the chip

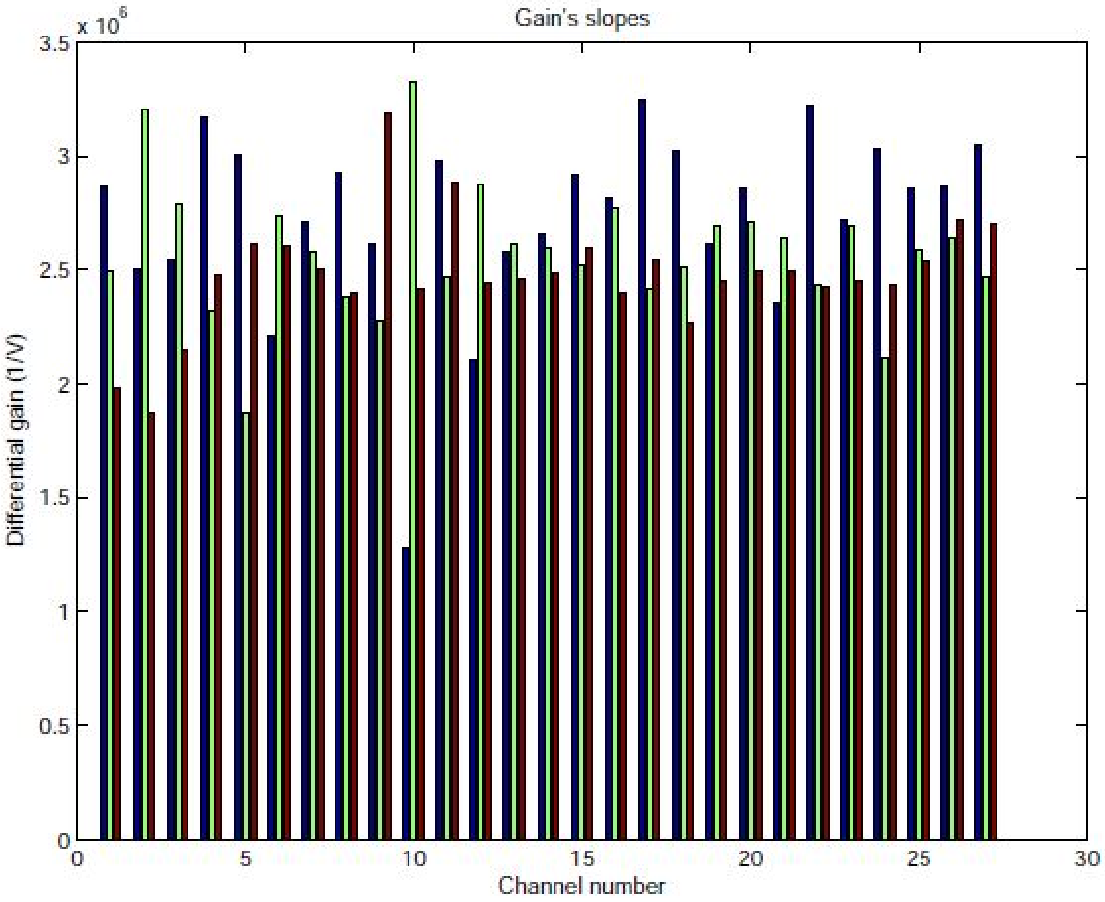

Figure 3.18: Differential Gain for every channel and every OV gap in chip W7-3. Since we measured at 4 OVs, we have 3 different DG per channel. The blue bin represents the slope between +5V and +4V, the green between +4V and +3V and finally the red is the slope between +3V and +2V

Gain f(OV): Differential Gain

Not only Gain itself is an important parameter, but even its functional dependency on OV has to be investigated. Since gain is supposed to be linear with OV (always at a first approximation), we tried to perform some measurements of the so called "Differential Gain", that is defined as:

$$DG = \frac{\partial G}{\partial OV} \tag{3.12}$$

With our approximations, DG is supposed to represent the slope of a straight line. We can have 4 experimental points for this straight line (4 different OVs) and 3 different slope values. The results are visible in Fig. 3.17 and Fig. 3.18. We remark once more how the method that obtains gain through

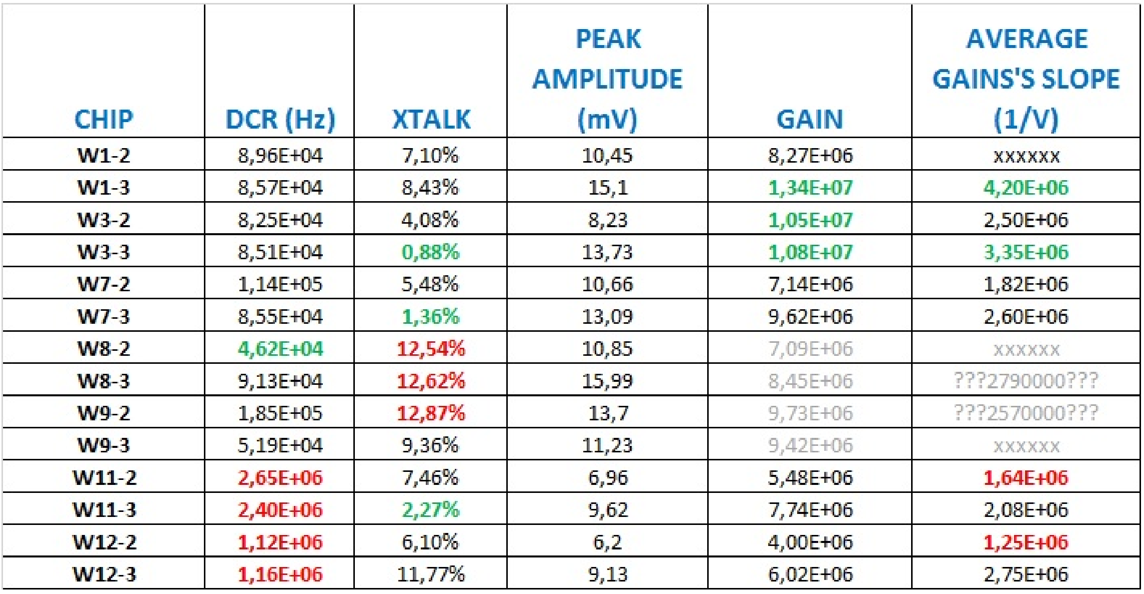

CHIP	DCR (Hz)	XTALK	PEAK AMPLITUDE (mV)	GAIN	AVERAGE GAINS'S SLOPE (1/V)
W1-2	8,96E+04	7,10%	10,45	8,27E+06	xxxxxx
W1-3	8,57E+04	8,43%	15,1	1,34E+07	4,20E+06
W3-2	8,25E+04	4,08%	8,23	1,05E+07	2,50E+06
W3-3	8,51E+04	0,88%	13,73	1,08E+07	3,35E+06
W7-2	1,14E+05	5,48%	10,66	7,14E+06	1,82E+06
W7-3	8,55E+04	1,36%	13,09	9,62E+06	2,60E+06
W8-2	4,62E+04	12,54%	10,85	7,09E+06	xxxxxx
W8-3	9,13E+04	12,62%	15,99	8,45E+06	???2790000???
W9-2	1,85E+05	12,87%	13,7	9,73E+06	???2570000???
W9-3	5,19E+04	9,36%	11,23	9,42E+06	xxxxxx
W11-2	2,65E+06	7,46%	6,96	5,48E+06	1,64E+06
W11-3	2,40E+06	2,27%	9,62	7,74E+06	2,08E+06
W12-2	1,12E+06	6,10%	6,2	4,00E+06	1,25E+06
W12-3	1,16E+06	11,77%	9,13	6,02E+06	2,75E+06

Figure 3.19: Recapitulatory results for KETEK SiPMs of the Spring 2014 batch. All the values here presented are the chip's average of the measured channels at +3V OV Chips coming from wafers 8 and 9 had problems of dark current stabilisation in time. Current was constantly decreasing, reaching an asymptote after several hours: a time we usually didn't have. We used to expect 15 minutes before every measurement waiting for the current to stabilise but still the Gain values are uncertain for those chips and are here presented in grey.

Dark Current is reliable, together with the simple physical model of the p-n junction operating in Geiger mode: for every channel we can see the linear behaviour within a reasonable experimental error (which may be originated from small but measured Temperature differences between measurements, second order effects, external noise etc...). The measured quantities for every chip of the batch are reported in the following table 3.19.

3.2 Photo-Detection Efficiency

Photo-Detection Efficiency (PDE) and its wavelength dependency can be seen as probably the most critical parameter for a SiPM and the most difficult to measure. It was necessary to have Gain and amplitude distribution's information before proceeding in PDE measurements. PDE can be defined as the ratio between the number of photons that arrive on the detector (Ph_{tot}) and the number of detected photons (Ph_{det}); one can express it as the product of the Quantum Efficiency multiplied by the geometrical efficiency of the detector and the probability that an absorbed photon is creating a carrier triggering the avalanche. In the geometrical factor we also include the reflected light at the SiPM's surface, even this component is almost negligible due to the anti-reflection coating every SiPM has been provided with.
QE and the transmittance of the anti-reflection coating are wavelength dependent: PDE is wavelength dependent too.
Resuming:

$$PDE_{SiPM}(\lambda) = \frac{Ph_{det}}{Ph_{tot}} = QE(\lambda) \cdot \epsilon_{geom}(\lambda) \cdot \epsilon_{avalanche} \tag{3.13}$$

All of these quantities are extremely difficult to be experimentally obtained, thus the method we used to investigate PDE consists of relative measurements.

3.2.1 Theoretical approach

The Photo-Detection Efficiency of a SiPM can be be expressed as:

$$PDE_{SiPM}(\lambda) = \frac{I_{SiPM}}{\phi_\gamma(\lambda)e} \tag{3.14}$$

where I_{SiPM} is the photocurrent extracted from the detector, ϕ_γ the incident photon flux and e the electron charge.
The only quantity we could measure with good precision was the photocurrent through a pico-ammeter. To bypass the unknown information about the photon flux, we used a calibrated photodiode of which we knew the Quantum Efficiency (QE) as a reference detector:

$$PDE^*_{SiPM}(\lambda) = \frac{I_{SiPM}}{I_{PD}} \cdot QE_{PD} \tag{3.15}$$

We used here the symbol PDE^* because we're not yet dealing with the real PDE, since we will need corrections for Gain, X-Talk and geometry factors.

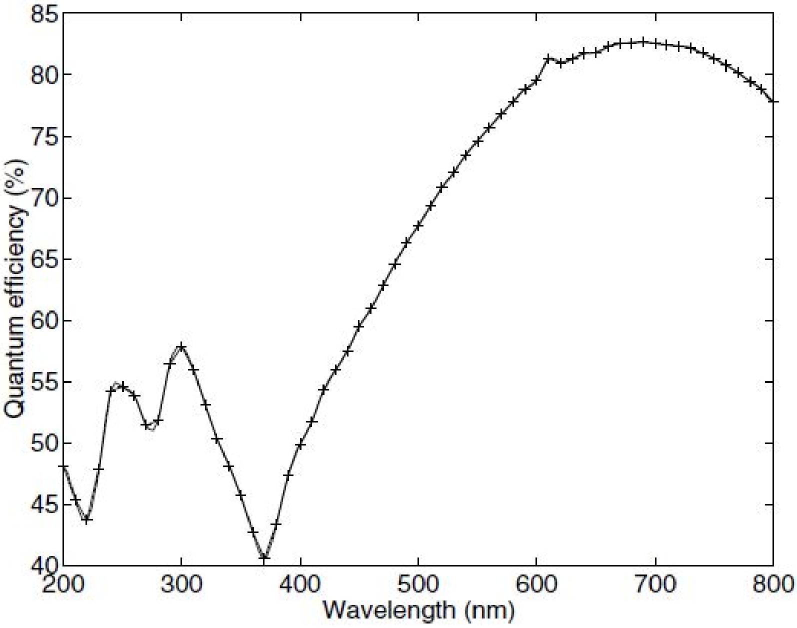

Figure 3.20: Photo-Diode's Quantum Efficiency

Once all the corrections made, we find a relative PDE measurement (fundamental to compare different devices). Moreover, with an absolute reference that KETEK provided us, we could get absolute PDE values. This reference SiPM's device is called KETEK-50D ADV and was guaranteed to have an absolute PDE peak of 30% at +3V OV.

3.2.2 Experimental Set-Up

A monochromator based set-up was used to characterise and compare the various devices as a function of the applied over-voltage. We needed a wide spectrum and stable light source to investigate PDE's wavelength dependency. The lamp of choice was a 75W high pressure Xenon arc lamp, housed in an elliptic reflector (see Fig. 3.21) [23].
The characteristics we needed were:

- Smooth and continuous spectrum from 300nm to 700nm
- Ellipsoidal reflector with a focal length adjusted to fit with the monocromator and providing full spectrum.
- High short term stability ($\approx$ 0.1%) and low long term drift (ideally 0%).

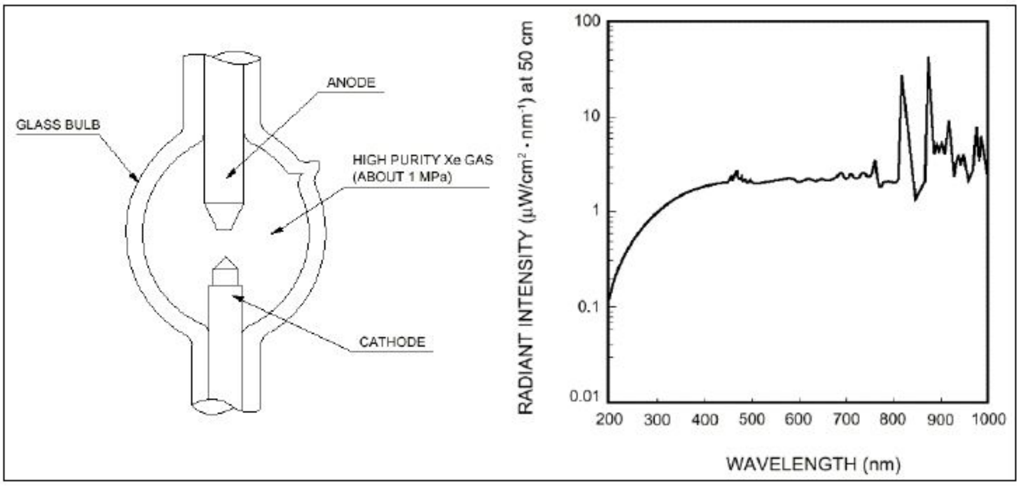

Figure 3.21: the Xenon White Lamp with its spectral distribution

The white light (filtered and decreased in intensity in order not to damage the very sensible SiPM) was passing through a double monochromator (located inside a dark box) that allowed us to sweep the visible spectrum from 300nm to 700nm; this interval represents the sensible region of our SiPMs.

The light coming out of the monochromator was guided through an optic plastic fibre just in front of the SiPM. We used to keep 10cm between the fibre's end and the device to leave the light diffract and form a large spot of uniform intensity on the detector. The SiPM under test was mounted on a micrometric table that permitted us to centre its position in respect to the light spot.

Just one SiPM channel per measurement was connected and supplied with bias Voltage.

Before every measurement we used to perform a calibration run in which, through the calibrated PIN diode, we read the light coming out from the monochromator to fully characterise it and eventually correct for possible time drifts. Moreover, a constant fraction of the lamp light was constantly observed to monitor its stability during measurements.

The whole set-up is reported in Fig. 3.22.

Corrections to the PDE formula

Once we got the photocurrent produced by the SiPM as a function of the wavelength, we had to apply several corrections, including X-Talk (that doubles the photocurrent produced by a single event) and Gain (that multiplies

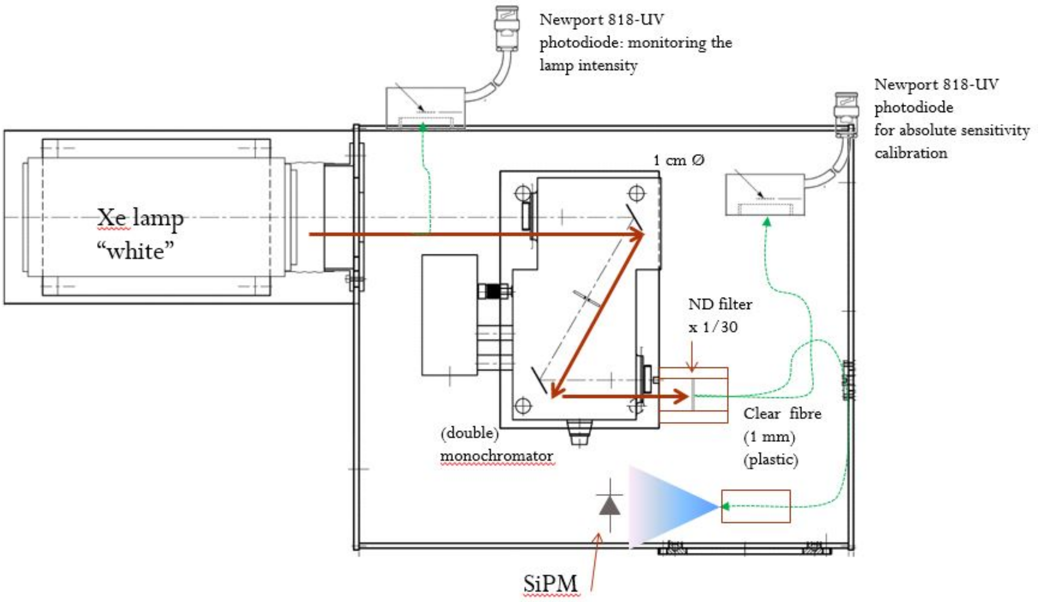

Figure 3.22: Experimental set-up for PDE measurements

the absorbed photon in multiple electrons generating the photocurrent). Finally we could arrive to PDE through the following formula:

$$PDE = \frac{I_{SiPM} \cdot QE_{PD} \cdot d^2}{(1 + XTalk) \cdot Gain \cdot I_{PD} \cdot S} \cdot NF \tag{3.16}$$

where:

- ***d*** is the distance between the detector and the fibre end. Since we didn’t know the photon flux, but we knew that it’s decreasing with the square of the distance, we corrected with this factor.
- ***S*** is the pixel surface of the detector. Since the photocurrent depends on the enlightened area while PDE does not, we corrected by this factor.
- ***NF*** is a Normalisation Factor, adjusted to bring the peak PDE of 50D ADV up to 1 at +3V OV (see Fig 3.23).

Measurements

The measurement procedure was almost completely automatised thanks to an already existing Labview program. It was actually controlling a small electric motor, used to select the output wavelength from the diffraction

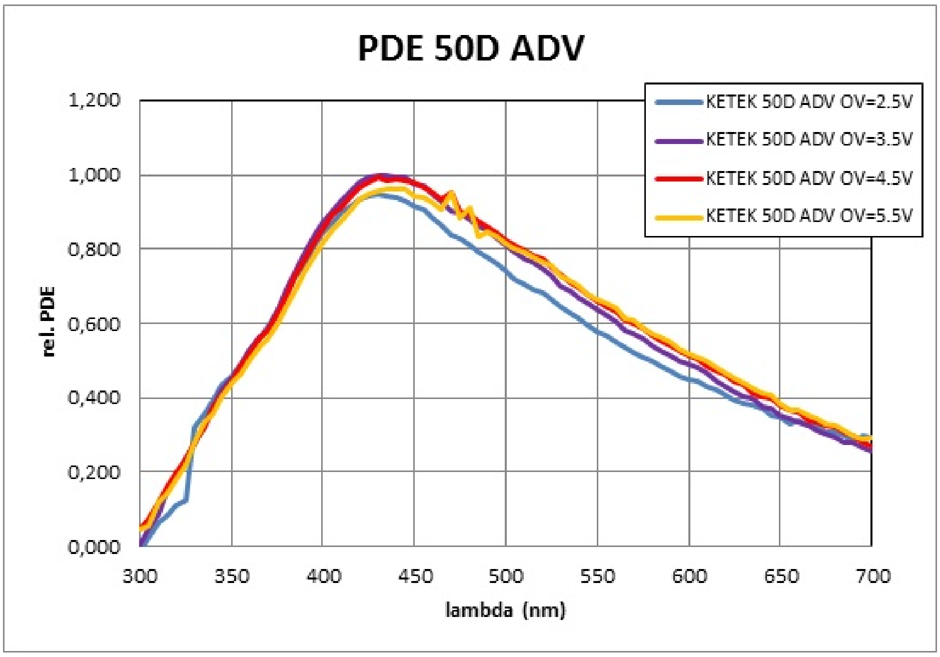

Figure 3.23: PDE measurements for the reference chip KETEK 50D ADV. The PDE values were normalised in order to have 1 as maximum PDE for the 50D ADV. The measurements were performed at different over-voltages. We don't see here the normal increasing PDE with OV: probably this device suffers PDE saturation with OV

gratings inside the monochromator.
First of all we used to read current at 200nm, there where the SiPM is blind, to obtain a dark current value. We used then to sweep the range from 300nm to 700nm with 5nm steps. For every step a current value was read with the picoamper meter, connected to the computer through a GPIB. The dark contribution was subtracted from the measured current.
Finally, having the program stored the PD calibrated current and its QE, for every λ it automatically calculates the value:

$$PDE^{*}_{SiPM}(\lambda) = \frac{I_{SiPM}(\lambda)}{I_{PD}(\lambda)} QE_{PD} \tag{3.17}$$

Through an Excel book we analysed those data adding further corrections.
Every PDE measurement was performed at 4 different OVs, nominalli +2V, +3V, +4V and +5V OV. We normally expected PDE to increase together with an increasing OV for physical reasons regarding once again the behaviour of a p-n junction.
We remember here that:

$$Q = C \cdot V \tag{3.18}$$

If we change V and we suppose that C (junction capacity) doesn't change, it means that a higher spatial charge Q has to be stored in the junction. A higher charge means a larger depleted region (this is actually also changing the junction capacitance, but we consider this second order effect negligible).
We have bent the band energy levels and therefore electric field exists only in the depleted region: only a photon absorbed in that specific volume can trigger the avalanche process and be detected. A larger depleted region is translated in a higher PDE.

3.2.3 Results and comments

The optimum PDE peak value one could dream of in 2013 was ≈40% [23].
KETEK worked in this direction to provide CERN with such a device.
We take now our usual test SiPM W7-3 to discuss the results.
The PDE relative to the 50D ADV, as well as the absolute results are shown in Fig. 3.24 and 3.25.
We underline that the 40% goal was actually reached at the forecasted operational OV (between +3V and +4V OV). This remarkable success helps the whole SciFi project. Every percent gained in PDE is indeed extremely precious for the SciFi Tracker, where we estimate that ≈ 10 photons/event can reach the detector.
Moreover we must remember here that opaque trenches, extremely useful

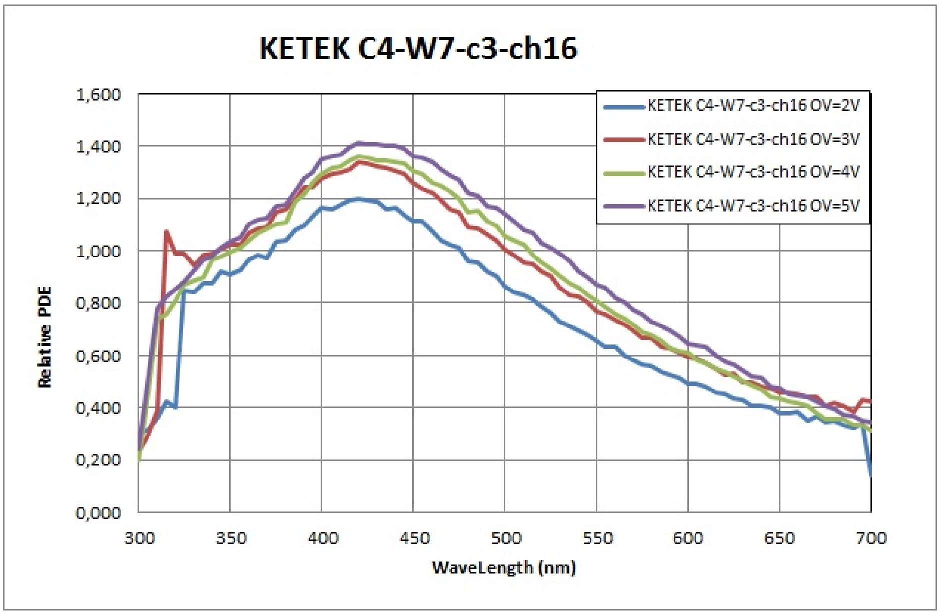

Figure 3.24: PDE for chip W7-3. Results relative to KETEK 50D ADV.

against X-Talk, were supposed to cost a trade off in terms of PDE, reducing the detector's geometrical fill-factor. We didn't recognise such an effect, as we can see in Fig. 3.26, where the results at +3V OV for chip W7-2 are reported.

The PDE peak value is not the only important quantity one has to observe to evaluate a SiPM. One has to look also at the spectral evolution of PDE. The most desirable situation should be a PDE plateau in the visible region and KETEK devices don't present such a behaviour, being the peak PDE relatively narrow, with rapidly decreasing values when moving towards longer wavelengths.
Those considerations lead us to the next section, where we discover that PDE itself is not a real figure of merit to evaluate the SiPM's quality.

3.2.4 Overlap between PDE and SciFi's emission spectrum

The best SiPM for the SciFi tracker is not the one with the highest PDE peak, but the one that detects the highest number of photons the fibre can carry to the detector.
The real figure of merit for a SiPM (FM_{SiPM}) is the overlap integral in λ of PDE multiplied by the fibre's emission spectrum (ES_{SciFi}).
We're going to talk widely about fibre's emission spectrum in the chapter con-

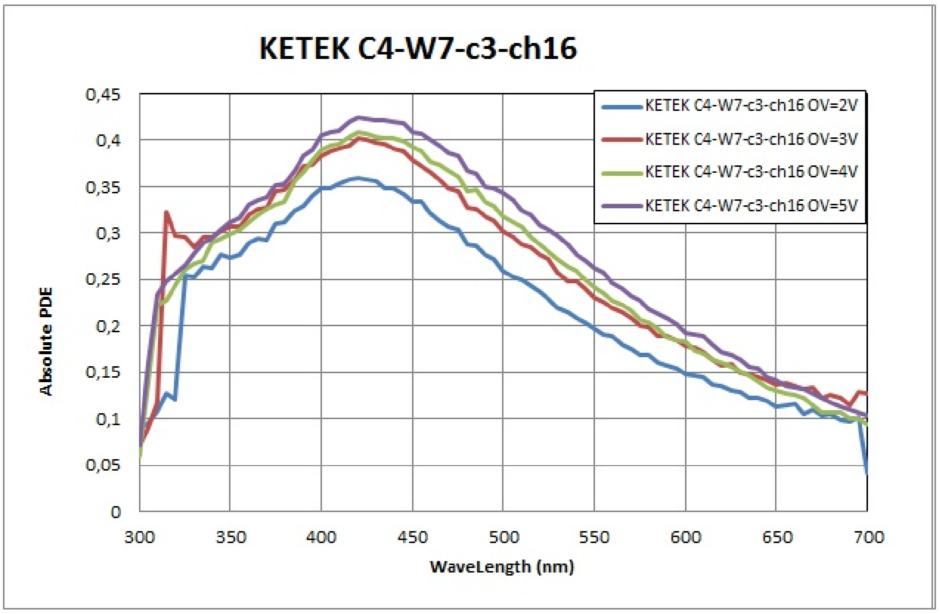

Figure 3.25: PDE for chip W7-3. Absolute results (peak PDE for 50D ADV =30%)

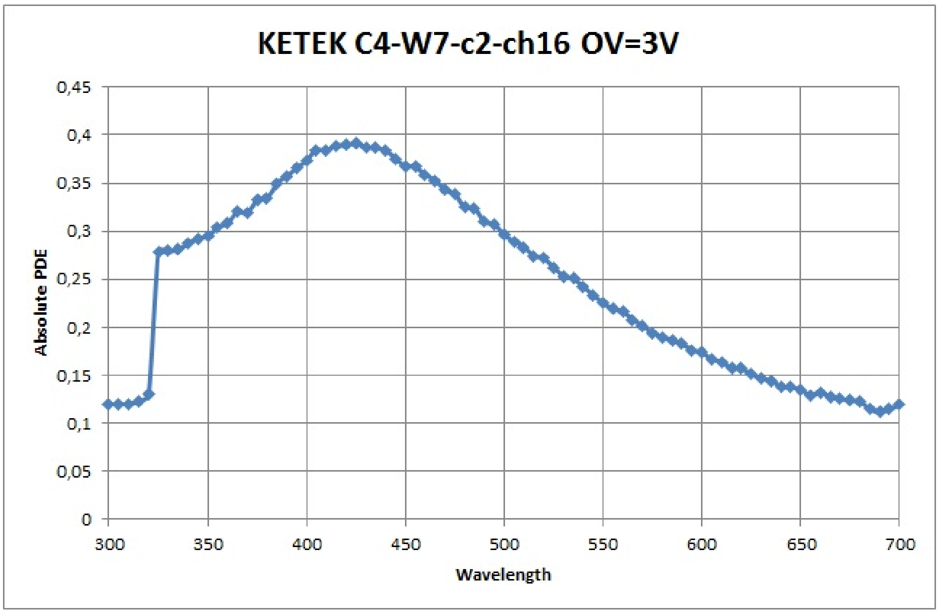

Figure 3.26: PDE for chip W7-2. Absolute results (peak PDE for 50D ADV =30%)

secrated to SciFi. For the time being we just anticipate that the spectrum strongly depends on the distance between the excitation and the measurement points, because different wavelengths feel in the fibre different attenuation. Radiation and scintillation mechanism are playing a role too, creating inhomogeneous propagation conditions fo different wavelengths. The simulated SciFi emission spectra are represented in fig. 3.27.

So we define our figure of merit as:

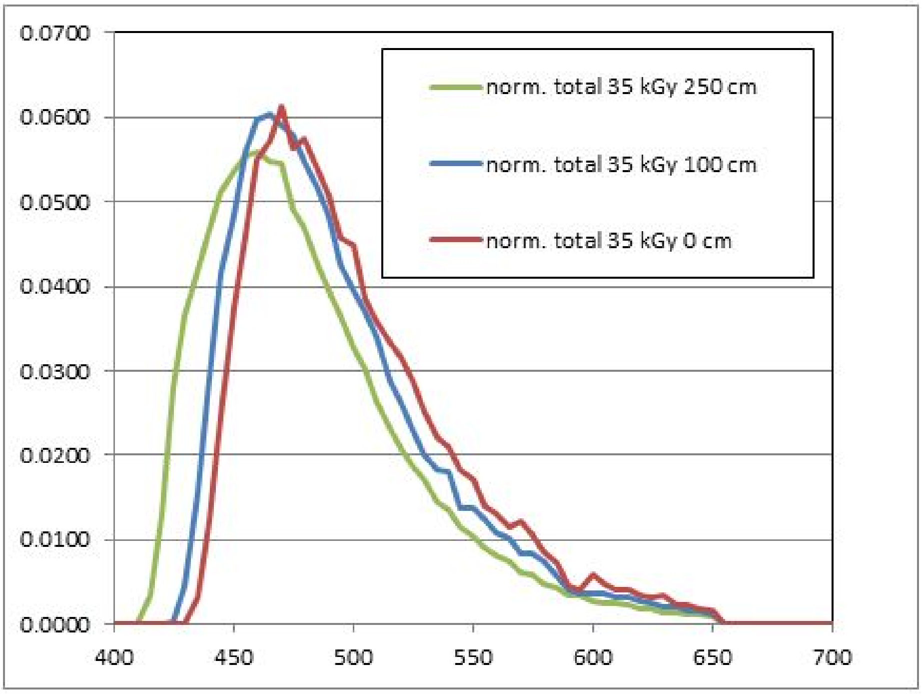

Figure 3.27: Simulated SciFi emission spectrum

$$FM_{SiPM} = \int_{400nm}^{650nm} PDE(\lambda) \cdot ES_{SciFi}(\lambda) d\lambda \tag{3.19}$$

where the integration limits correspond to the non-zero emitted radiation for a SciFi.

We could not calculate an integral being our measurement discrete. We passed to a discrete sum, with $\Delta\lambda = 5nm$:

$$FM^*_{SiPM} = \sum_{\lambda=400nm}^{\lambda=650nm} PDE(\lambda) \cdot ES_{SciFi}(\lambda) \cdot \Delta\lambda \tag{3.20}$$

Considering this quantity as the figure of merit, we recognise that despite the substantial improvement realised by KETEK in the last year, the optimum is has still to be reached. The peak PDE should be found at ≈ 470nm in order to perfectly match SciFi ES, and not at ≈ 420nm as it is right now. If we simply shift PDE to make the two peaks correspond, we see how much we're loosing because of this "misalignment". If we call the maximising wavelength of PDE λ_{PDE} and the maximising wavelength of ES λ_{ES}, we obtain:

$$\frac{FM^*_{SiPM}}{FM^*_{SiPMshifted}} = \frac{\sum\limits_{\lambda=400nm}^{\lambda=650nm} PDE(\lambda) \cdot ES_{SciFi}(\lambda)}{\sum\limits_{\lambda=400nm}^{\lambda=650nm} PDE(\lambda - \lambda_{PDE} + \lambda_{ES}) \cdot ES_{SciFi}(\lambda)} \approx 85\% \tag{3.21}$$

The global results for all of the chips concerning PDE measurements are reported in the following table 3.28.

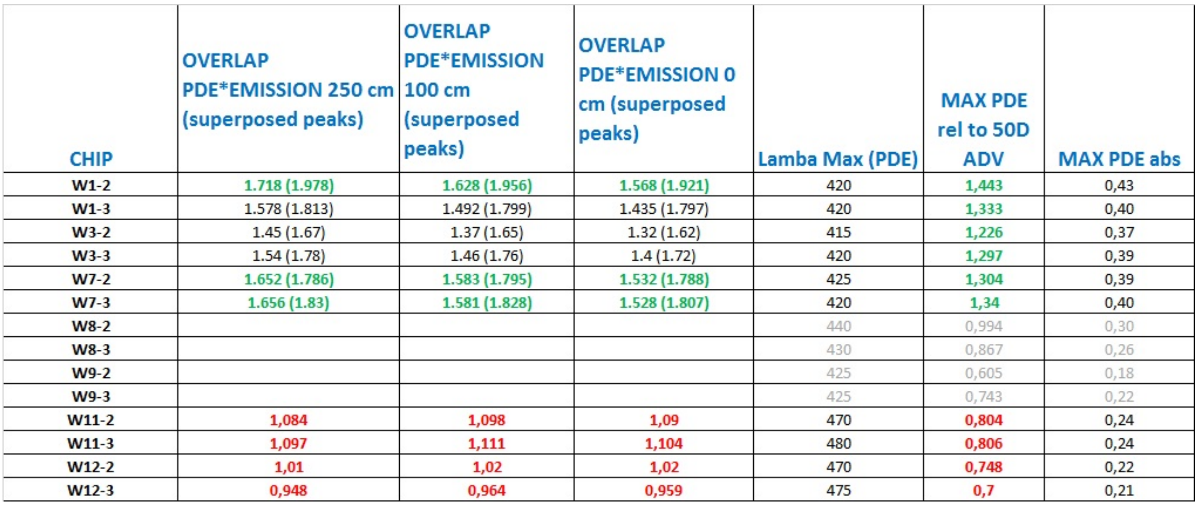

CHIP	OVERLAP PDE*EMISSION 250 cm (superposed peaks)	OVERLAP PDE*EMISSION 100 cm (superposed peaks)	OVERLAP PDE*EMISSION 0 cm (superposed peaks)	Lamba Max (PDE)	MAX PDE rel to 50D ADV	MAX PDE abs
W1-2	1.718 (1.978)	1.628 (1.956)	1.568 (1.921)	420	1,443	0,43
W1-3	1.578 (1.813)	1.492 (1.799)	1.435 (1.797)	420	1,333	0,40
W3-2	1.45 (1.67)	1.37 (1.65)	1.32 (1.62)	415	1,226	0,37
W3-3	1.54 (1.78)	1.46 (1.76)	1.4 (1.72)	420	1,297	0,39
W7-2	1.652 (1.786)	1.583 (1.795)	1.532 (1.788)	425	1,304	0,39
W7-3	1.656 (1.83)	1.581 (1.828)	1.528 (1.807)	420	1,34	0,40
W8-2				440	0,994	0,30
W8-3				430	0,867	0,26
W9-2				425	0,605	0,18
W9-3				425	0,743	0,22
W11-2	1,084	1,098	1,09	470	0,804	0,24
W11-3	1,097	1,111	1,104	480	0,806	0,24
W12-2	1,01	1,02	1,02	470	0,748	0,22
W12-3	0,948	0,964	0,959	475	0,7	0,21

Figure 3.28: PDE measurements: recapitulating results.
Since we didn't trust gain measurements for chip coming from wafer 8 and 9 (see Fig. 3.19), we don't present here their PDE as a sure number, but in grey.
In the column indicating the Overalap, one can find in brackets the result if the peaks of PDE and SciFi's ES were superposed.

Photos

To visually explain our work, we present here photos of the experimental set-up used for PDE measurements, inside and outside the dark box.

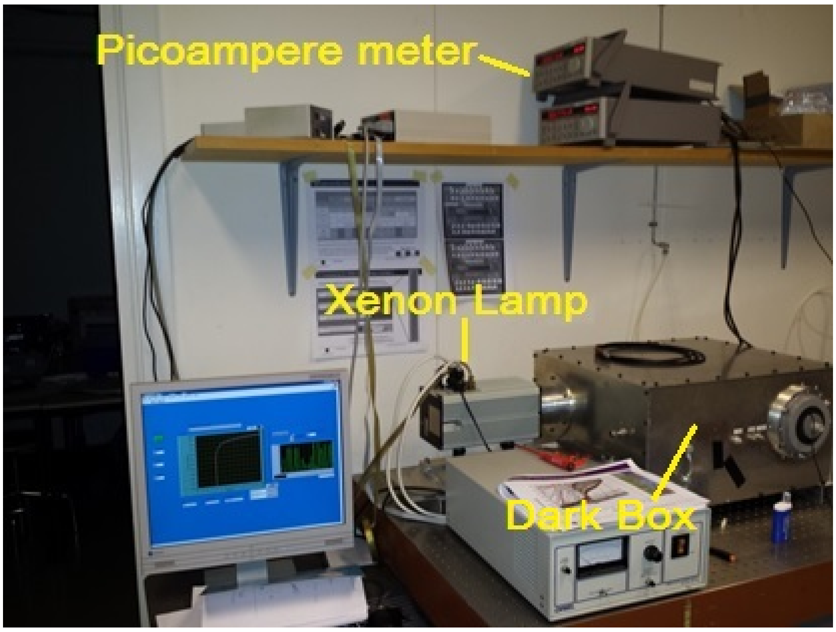

Figure 3.29: PDE set-up

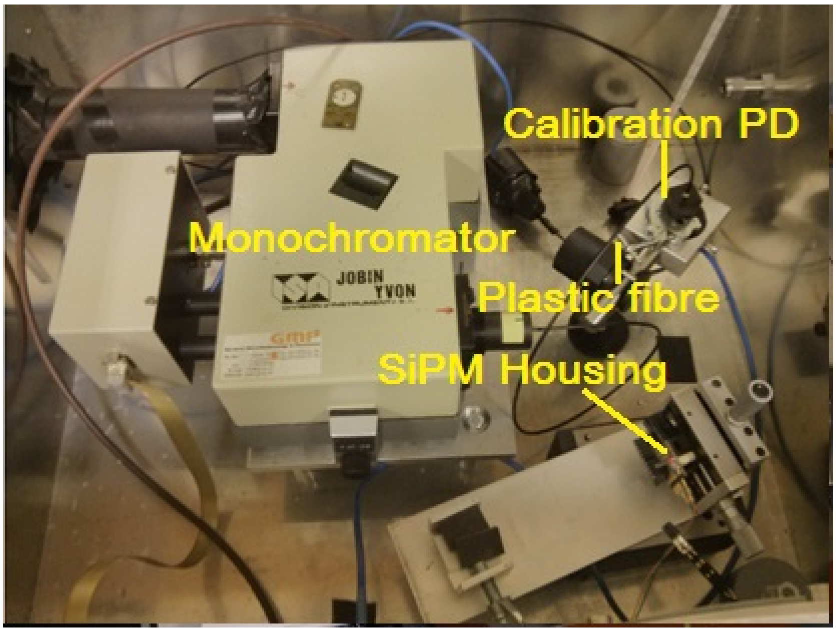

Figure 3.30: PDE: inside set-up

3.3 Temperature Characterisation

SiPM will work in the SciFi detector at $-40°$ C. The fundamental reason for that can be found in the strong connections between Dark Count Rate and Temperature. The main origin of the ghost events one can see in the temporal trace of a SiPM in the dark are due to theramal generation in the depleted region of the p-n junction.
Carriers in a semiconductor are ruled by a Fermi-Dirac Statistics, but when we deal with great energies (in the order of the 1.12 eV of the Si band Gap) we can with optimal approximation use a normal Boltzmann Statistics.
If we call dP_{VC} the probability that an electron owns an energy included between E_{GAP} and $E_{GAP} + dE$, it comes out that the probability for this elecctron to have sufficient thermal energy to pass from the valence to the conduction band is proportional to a Boltzmann exponential factor:

$$dP_{VC} \propto e^{-E_{GAP}/K_BT} \cdot dE \tag{3.22}$$

The total probability is so proportional to:

$$P_{VC} \propto \int_{E_{GAP}}^{\infty} e^{-E/K_BT} \cdot dE = CT^{3/2} exp\left(-\frac{E_{GAP}}{2K_BT}\right) \tag{3.23}$$

Cooling is so the simplest solution to reduce exponentially Dark Count Rate. Nevertheless, we saw that a DCR of less than 100kHz is easily achievable nowadays and it would be sufficient to have a satisfactory signal/noise rate, since LHCb reads out at 40MHz [29]. In these considerations we didn't take radiation damage into account: even if SiPMs will be installed at least 2.5m far from the beam pipe (there where doses are high: $\approx$ 20-30 kGy) and even if they will experiment doses under 1kGy principally made of neutrons, they will suffer and increase exponentially their DCRs (see Fig.3.31).

The detector is supposed to be working for 5 years during which the it will be constantly a radiation target: at the end of this period cooling will be the only solution to continue the data extraction from the SciFi tracker, otherwise noise produced in SiPMs by radiation will cover every signal.
It is so of great importance to discover how those devices change their behaviour in Temperature. We suppose that two important quantities are mainly changing:

- **Dark Current and DCR**.
- **Break-Down Voltage**. Atomic vibrations of the crystal lattice increase their amplitude with a growing Temperature. Probability that

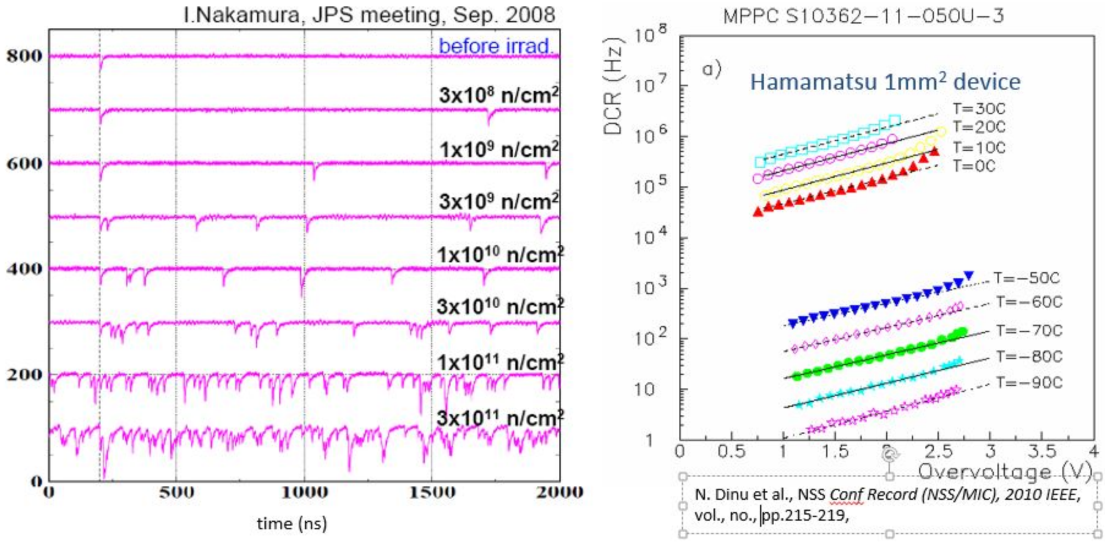

N. Dinu et al., NSS Conf Record (NSS/MIC), 2010 IEEE, vol., no., pp.215-219,

Figure 3.31: DCR degradation due to neutron irradiation and DCR improvement due to cooling

the generated carriers may collide with an atom in the crystal rises up. During collisions, carriers loose their kinetic energy. This can happen before carrier's energy is high enough for ionisation, reducing the probability of avalanche generation. To make ionization easier to occur, the reverse voltage should be increased and the internal electric field enlarged: BDV increases with Temperature.
BDV is the reference point from where we determine OVs. Since Gain, X-talk, PDE etc. depend on OV, indirectly every important value of a SiPM is actually depending on T.

3.3.1 Experimental Set-Up

The most reliable method to individuate BDV is to measure the current produced by a SiPM as a function of the applied bias Voltage. By definition, at BDV an internal Gain starts to be produced.
A complex set-up was built to allow V-I curves' measurements at different Temperatures. The set-up should provide the possibility of cooling teh chip down to -40°C. We built a cold box, taking care that it could be thermally isolated. Two cooling steps were necessary to cool the chip down at -40°C:

1. A first cooling machine, using refrigerating liquid, was able to bring our system at ≈-10°C.

2. A Peltier element was mounted to generate an additional ΔT of 30°C, necessary to bring the detector at -40°C.

The SiPM was positioned over the Peltier, that was itself fixed on a cold box's wall. The Peltier and the chip were covered by an additional plastic box. Thi additional layer inside the cold box provided dark, more thermal isolation and a non-humid environment thanks to a little hole in this plastic box, where we were injecting pressured nitrogen, filling the plastic box with it and avoiding water to condense and subsequently freeze over the detector. In a first moment, measurement were performed in the dark, presuming that Dark Current would have been high enough to allow precise measurements. Experience revealed that Dark Current was insufficient, especially at low Temperatures; at -40°C typical Dark Current stay around 1nA. A LED was finally put inside the plastic box, in order to make the SiPM produce measurable currents even at -40°C.
Resuming, inside the plastic box we had:

- The Peltier element and its supplying cables.
- The SiPM and its supplying cables (bias Voltage and current cables)
- Two Temperature detectors (Pt 1000): one for the base cooled by the liquid and one over the Peltier.
- An hygrometer and its supplying cables.
- A LED with its supplying cables.

Just one channel per SiPM was measured, starting from -40°C, going up to +30°C with 10°C steps. Current was read by a picoampere-meter every 5mV. An appositely written Labview program was controlling current measurements, plotting the V-I curves and their derivatives in real time.
Temperature's stable control was guaranteed by a complex software connected to a FPGA, appositely studied and programmed to deliver the correct current value to the Peltier. The software used a PID controller.

3.3.2 I-V curves, Breakdown Voltage(T)

Many definitions can be found and chosen for Break-Down Voltage. We are using the one that defines BD Voltage as the voltage for what the first derivative of the I-V curve divided by the current reaches its maximum:

$$V_{BD} = max \frac{1}{I_{SiPM}(V)} \frac{\partial I_{SiPM}}{\partial V} \tag{3.24}$$

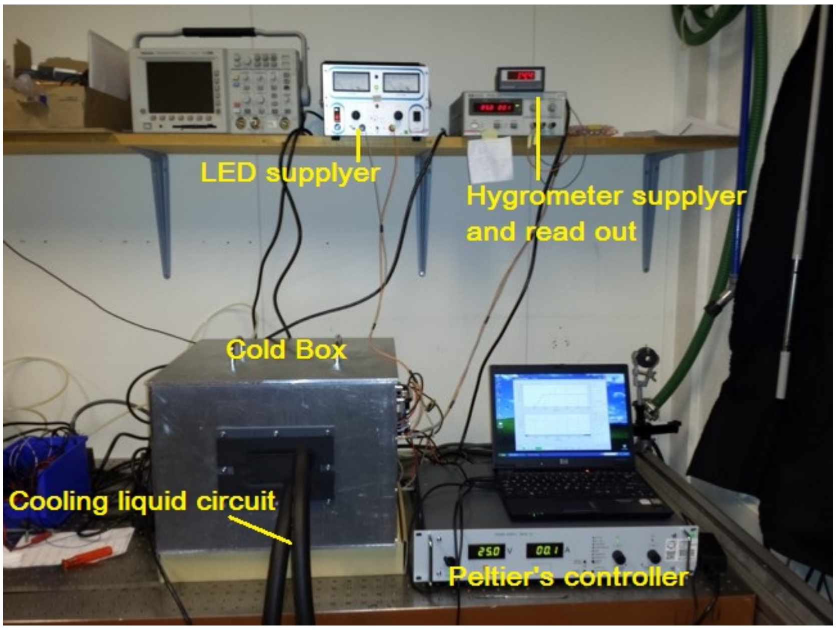

Figure 3.32: Cooling Set-Up: external view

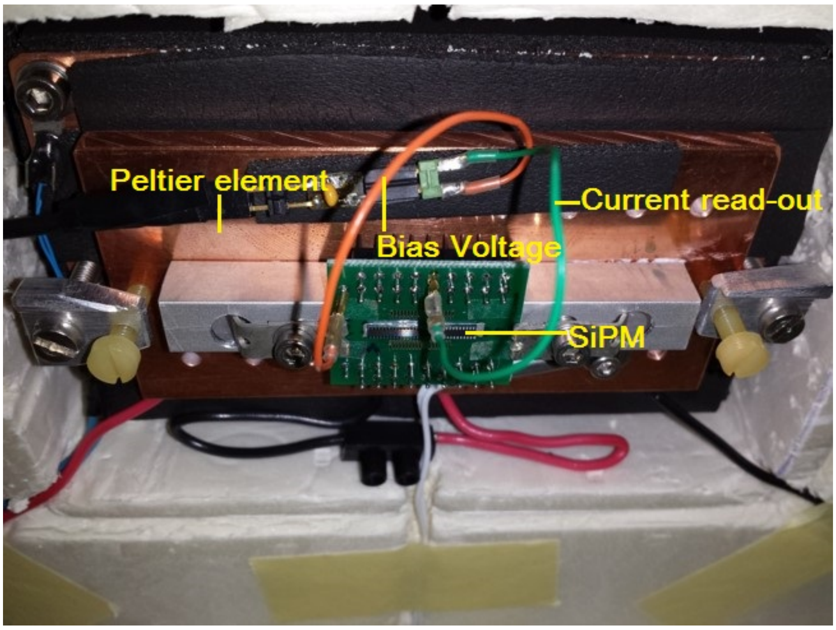

Figure 3.33: Cooling Set-Up: internal view

The I-V curves and the relative derivative performed on our standard chip W7-3 are visible in Fig. 3.34 and 3.35.

The plot is nicely showing that BDV is moving towards lower values with the decreasing Temperature. Moreover, it seems that BDV is following a linear dependency in T, as confirmed by the plot BDV vs T (3.36).

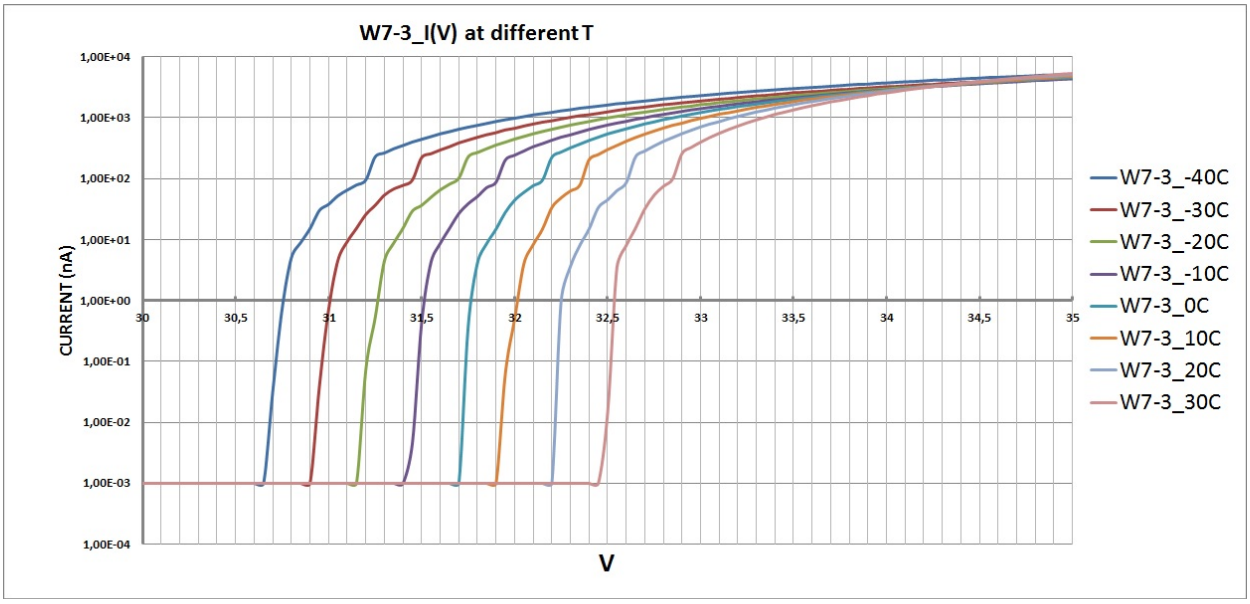

Figure 3.34: I-V curves

A linear displacement of BDV in T was previewed, being the same behaviour observed in previous SiPM batches. The goal for this new 2014-technology was to minimise this BDV's translation, ideally having a constant BDV. This because, every important parameter of a SiPM being OV-dependent, one should desire not to see Gain, X-talk or PDE fluctuations from one SiPM to the other when they're at slightly different Temperatures. In fact, even if nominally all of the SiPM of the SciFi tracker will be at the same T, this cannot be possible, considering that:

- Fibres and in general the entire tracker will stay at room T (high and non-uniform thermal gradient in the detector).
- The cooling system, for how precise it could be, it's not perfect and small ΔT are unavoidable.
- Unexpected and unpredictable thermal contacts.

Finally, all SiPMs will be precisely supplied by the same bias Voltage (no possible adjustments for T differences).

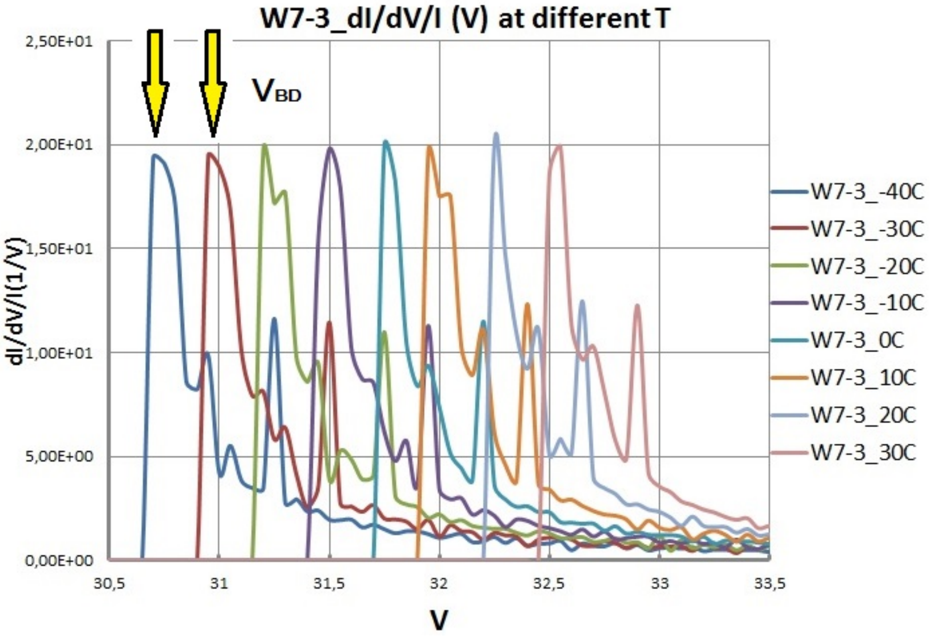

Figure 3.35: Derivative scaled with current of I-V curves

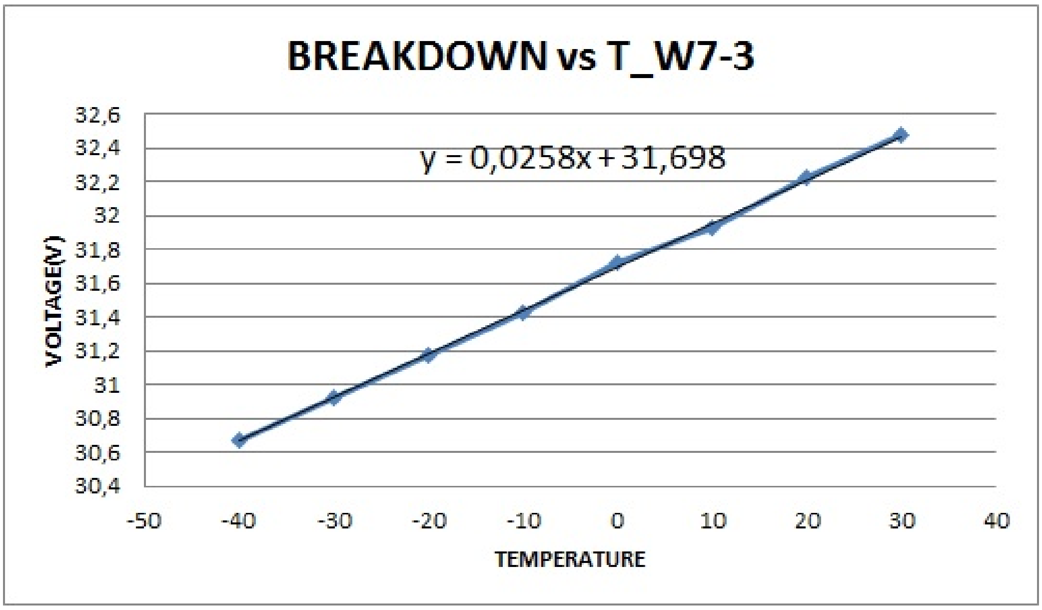

Figure 3.36: BDV as a function of Temperature. One can appreciate the linear dependency between the two quantities and the T-coefficient of 25.8 mV/K

Before 2014, normal values for T-coefficients (the slope of the straight line in the BDV-T curve 3.36) were around 40mV/K; in this new batch we saw a consistent drop of the T-coefficients, down to 20-25mV/K. KETEK managed to impove its devices following CERN's requests.

3.3.3 Dark Current (V,T)

From the moment that we had to cool SiPMs to measure I-V curves dark current was also measured in order to discover the dark noise evolution.
In principle, one should proceed differently to better detect Dark noise, since dark current is sometimes almost insignificant and difficult to be correctly measured; moreover it is affected by fluctuations, noise etc.. To obtain a trustful result concerning noise, one should have repeated what was done for DCR, i.e. pulse counting.
Pulse counting was the first idea we had for measurements at low T too, but electromagnetic noise forced us to renounce; the great quantity of cables for Temperature and humidity sensors, for the Peltier supplying and bias Voltage were noise generators and worked as antennas capturing the external e.m. noise in the room. Moreover, we had to drill holes in the metallic cold box to bring the cables in: this made the box a useless Faraday cage. During the first measurements, SNR was dramatically below one, leading to impossible pulse measurements. Dark current is however sufficient to provide a quantitative idea of the noise reduction with T.

Dark current measurement and $T_{1/2}$ determination

To obtain the value we needed we used an indirect measurement.
For every T, with the LED switched off, we took at a random(but above BDV) bias voltage that we call V_{dark}, a I_{dark} value. Once the BDV was determined as explained in the previous section, we knew exactly at which OV V_{dark} corresponds.
Since, as usual, the interesting region is for us between +3V OV and +4V OV, to know I_{dark} in this range and precisely at +3.5V OV, we made the hypothesis that I_{dark} is actually scaling as the current produced by the enlightened SiPM:

$$\frac{I_{light}(V_{dark})}{I_{light}(V = 3.5V)} = \frac{I_{dark}(V_{dark})}{I_{dark}(V = 3.5V)} \tag{3.25}$$

and so

$$I_{dark}(V = 3.5V) = I_{dark}(V_{dark}) \cdot \frac{I_{light}(V = 3.5V)}{I_{light}(V_{dark})} = I_{dark}(V_{dark}) \cdot CF \tag{3.26}$$

where CF stays for Correction Factor.
That way we could plot the dark current at +3.5V OV for every temperature, as shown in Fig. 3.37 and then fit the result with an exponential function.
We used in this situation an exponential fit in base 2:

$$I_{dark} = A \cdot 2^{T/T_{1/2}} \tag{3.27}$$

We wanted in fact to determine the so called $T_{1/2}$, that is the ΔT we need to decrease if we want noise to be halved.
A reasonable value for $T_{1/2}$ is around 10°C, that is what we find for chip W7-3.
In this field there were no improvements nor deterioration, being 10°C a standard value also in the past years. Of course a smaller value would be desirable. We end this section presenting in Fig. 3.38 the results for the whole batch. We didn't measure chips coming from wafers 8 and 9 because at this stage it was already clear that they had problems and in general, from all the other measurements, they were not good candidates to be the best technology KETEK has to invest in.

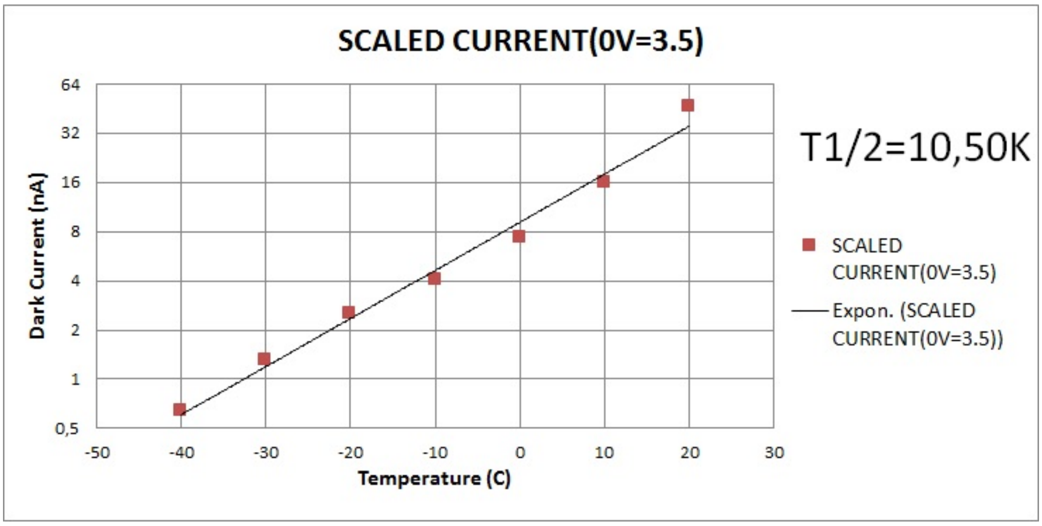

Figure 3.37: Dark current at +3.5V OV as a function of T. The Y-axis is in logarithmic scale with basis=2

3.4 Next R&D steps for SiPMs

The part of this master work spent on SiPMs ends here.
The SciFi project is a huge collaboration, with 19 institutes involved (universities, research labs and companies): after a first "disordered" starting

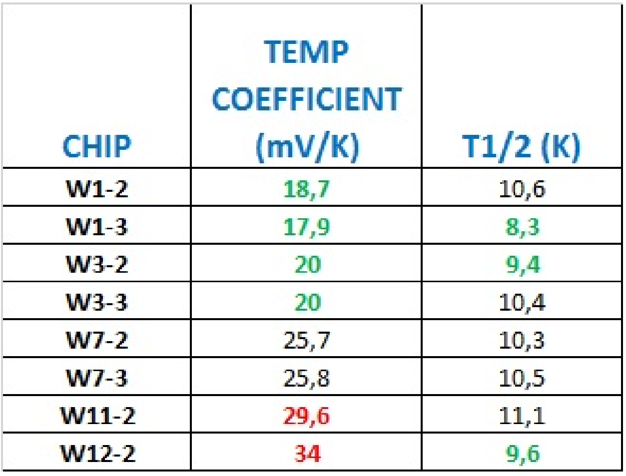

CHIP	TEMP COEFFICIENT (mV/K)	T1/2 (K)
W1-2	18,7	10,6
W1-3	17,9	8,3
W3-2	20	9,4
W3-3	20	10,4
W7-2	25,7	10,3
W7-3	25,8	10,5
W11-2	29,6	11,1
W12-2	34	9,6

Figure 3.38: Temperature measurements: results

period, with every institute working quite independently without a general ordering criterion, a more structured organization has been planned at the end of May 2014.

Here it was established that EPFL (École Polytechnique Fédérale de Lausanne) would be in charge of SiPM research and development. Every result will continue to be the base of a positive feedback for the producing companies. Partnership with KETEK and Hamamatsu (the other principal competitor in the SiPM market) will last.

We can try to imagine where the research direction will go.

SiPM packaging will be a delicate but mandatory step. It will consist of putting in the final housing chips that turned out to be best from our measurements, that is to say:

- W1-2
- W3-3
- W7-3

After this passage, chips must be irradiated. SiPMs in LHCb will be exposed to $1.2 \cdot 10^{12}$ neutrons of 1MeV eq./cm2 (50 fb-1): a set up to produce a similar irradiation is required.

Furthermore, a detailed FLUKA simulation showed that shielding (Polyethylene with 5% Boron) can halve this fluence: it has to be experimentally demonstrated.

Then, EPFL will have to repeat after irradiation all the measurement we presented in this chapter in order to investigate SiPM's behaviour in presence of radiation.

Finally some test must be performed to understand whether some annealing process is possible after radiation and, if it is, if it has a relevant importance.

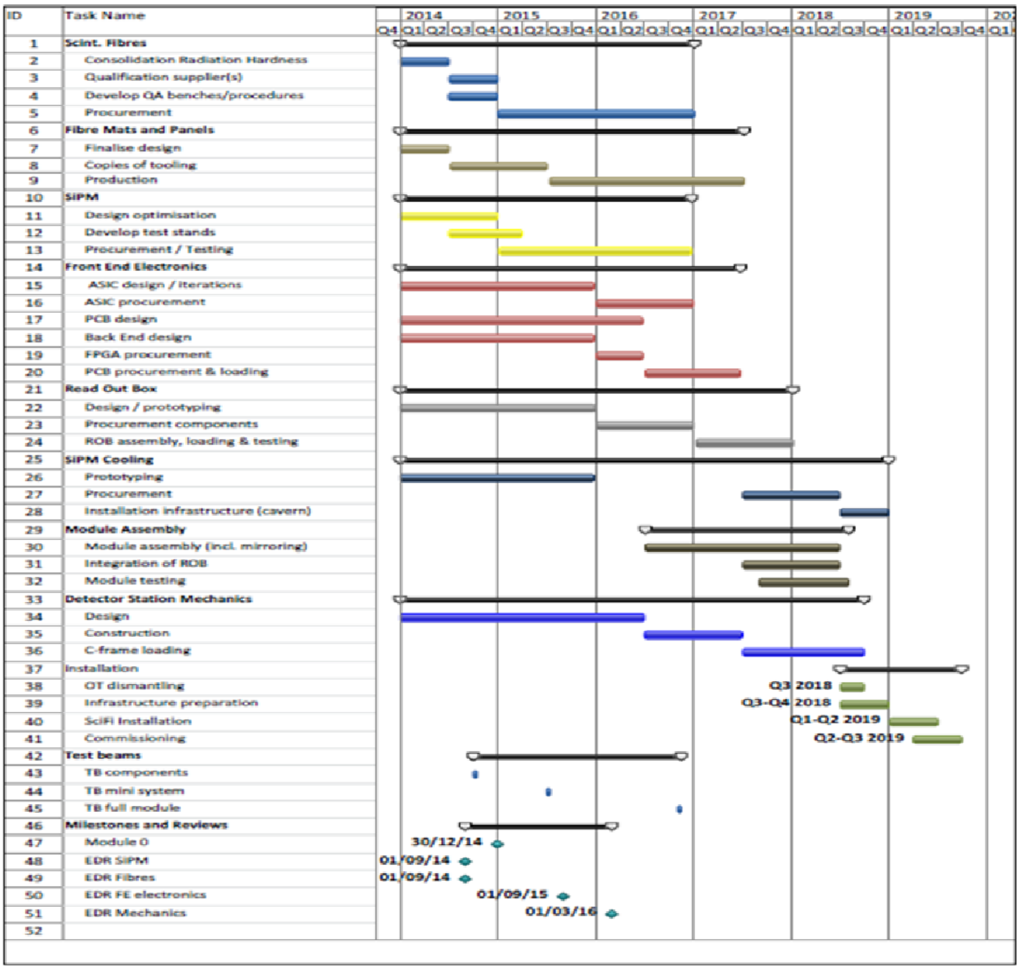

Figure 3.39: SciFi Tracker's Schedule until 2019

Concerning the CERN group working on the SciFi Tracker, it was designated to be in charge of research on Scintillating Fibres.
The next chapter will describe the second part of this master work, concerning principally experimental work on SciFI.

Chapter 4

Scintillating Fibres

Plastic scintillating fibres with a circular cross-section and a total diameter of 0.250mm, which includes two cladding layers nominally 3% total thickness each, are intended to be used in the LHCb SciFi Tracker.
For the time being, the only producer of high quality fibres is the Japanese company *Kuraray* [24].
Kuraray Scintillating Fibres are composed by [25]:

- Doped Polystyrene (PS) core, $n = 1.59$.
- Internal cladding made of plexiglass (PMMA), $n = 1.49$.
  The two claddings together are $\approx 10\mu m$ thick.
- External cladding made of fluorinated polymer, $n = 1.42$.

The numerical aperture of the fibre is 0.72. In the core we find dopants of different type, principally used to increase the amount of scintillated light and shift its wavelength. Different dopant concentrations (from 500ppm up to 5000ppm) can be chosen to vary the fibre's characteristics. What these dopants precisely are made of, as well as their complete formula, is not revealed by Kuraray. Their optimal concentration (especially the WaveLength Shifter's concentration, see below) has still to be determined.In particular, we're going to present results shown by 4 fibre models:

- Kuraray SCSF78 - 500ppm WLS
- Kuraray SCSF78 - 1000ppm WLS (*Kuraray Standard*)
- Kuraray SCSF78 - 2000ppm WLS
- Kuraray SCSF78 - 5000ppm WLS

The figure of merit that one can use to determine whether a fibre is better than another is a combination of different factors:

- **Light Yield**. How many photons are produced when the fibre is crossed by a charged particle.
- **Attenuation**. How much light is lost during propagation from the scintillation site to the SiPM.
- **Radiation damage**. How fibre's performance is degrading because of radiation.
- **Geometrical stability**. How much the fibre's dimensions are close the nominal ones and how rare are geometrical defects (i.e. bumps, greater diameter etc.).

Experiments described in the following chapter were built and performed in an R&D phase of the SciFi project, with the aim to research the best solution for fibre procurement and to guarantee in a later moment a fast, reproducible and reliable quality control for all the fibres that will be used in the LHCb SciFi Tracker.

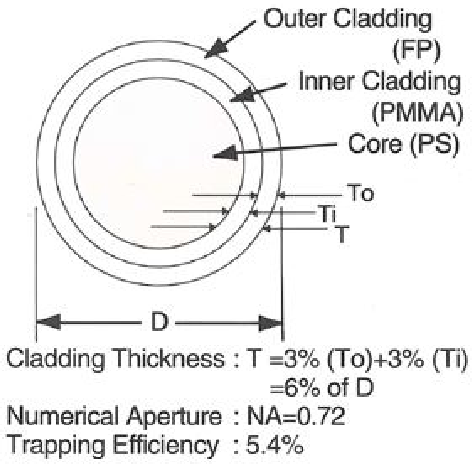

Figure 4.1: Kuraray double-cladded scintillating fiber

4.1 Basics of Scintillating Fibres

4.1.1 Trapping Fraction

Scintillating plastic fibres are considered as the active elements for the SciFi-Tracker project. A signal of optical photons is produced through a multi-step process when ionisation energy is deposited in the core of the fibre; approximately 4.6eV of deposited energy are required to produce an excitation of the polymer [26, 21]. Light is isotropically produced over the entire solid angle. The light a fibre can capture is limited by total internal reflection conditions: the greatest part of scintillation is immediately lost. We consider for example a single-cladded fibre, with PS core and PMMA cladding, we would have:

$$\theta_{crit} = asin\left(\frac{n_{PMMA}}{n_{PS}}\right) = asin\left(\frac{1.49}{1.59}\right) = 69.6° \tag{4.1}$$

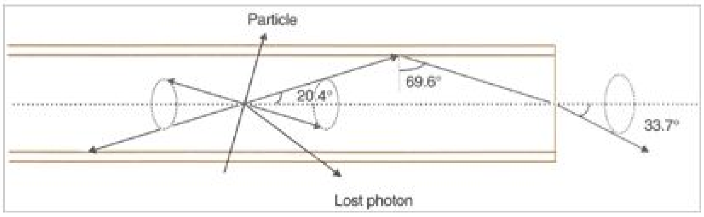

Figure 4.2: Single-cladded SciFi: trapping angle

Since our fibre is a round fibre, the trapping fraction is:

$$\epsilon_{trap} \geq \frac{1}{4\pi}\int_{0}^{\frac{\pi}{2}-\theta_{crit}} 2\pi sin\theta d\theta = 3.1\%(perpart) \tag{4.2}$$

We put the $\geq$ symbol to indicate that we are considering just the meridional modes: helical path or non-meridional light rays will further increase this number, but are highly attenuated (Fig. 4.3).

Almost 94% of the scintillating light is lost in a single-cladded fibre. This fraction is reduced if we consider a double-cladded fibre:

Figure 4.3: Geometrical rays and helical paths in a fibre

$$\theta_{crit} = asin\left(\frac{n_{PMMA}}{n_{PS}}\right) = asin\left(\frac{1.42}{1.59}\right) = 63.3° \tag{4.3}$$

That means:

$$\epsilon_{trap} \geq \frac{1}{4\pi}\int_{0}^{\frac{\pi}{2}-\theta_{crit}} 2\pi sin\theta d\theta = 5.4\%(perpart) \tag{4.4}$$

that corresponds to more than 50% of relative increase of the trapped light.

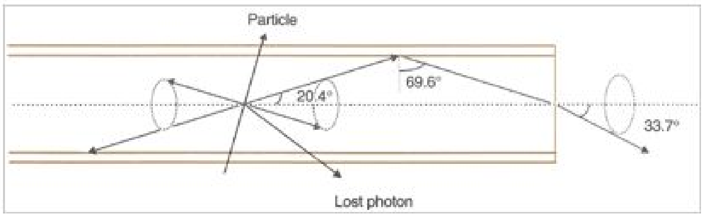

Figure 4.4: Double-cladded SciFi: trapping angle

4.1.2 Scintillation Process

The organic scintillation mechanism is based on the π-electrons of the benzene ring (C_6H_6). A photon signal is produced though a multi-step process.

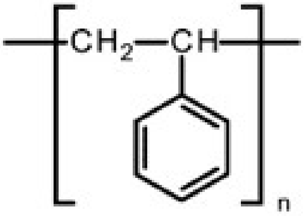

Figure 4.5: Polystyrene, used for Scintillating Fibre's core

Ionisation energy is deposited by the ionizing radiation in the polystyrene core of the fibre; approximately 4.6 eV of deposited energy is required to produce an excitation of the polymer. However, the relaxation time and light yield of the base organic phosphorescent material is quite poor: the polymer could stay in an excited state for a long time (10^{-4}s), in which the detector could be partially blinded to new-coming particles.

An organic fluorescent dye with matched excitation energy level structures is added to the polystyrene solvent base ($\approx$1% by weight) to improve the efficiency of the scintillation mechanism. Energy is transferred quite rapidly (sub-ns) from the base to the dye thanks to a non-radiative dipole-dipole transmission, known as Forster Transfer, where the excited energy state of the dye will subsequently relax by emission of a photon.

The fluorescent dye is chosen to have a high quantum efficiency (>95%), a particular emission wavelength spectra, and fast decay time (a few ns, nominally 2.8ns [25]). Single dopant fibres that emit in the blue-region (such as PMP dye) typically have a greater attenuation, due to the self-absorption of the light by the dye. Two solutions can be proposed to avoid self-absorption. For example dyes with larger separation between their absorption and emission spectra (Stokes' Shift), such as 3HF which emits in the green (400-

600nm, peaked at 450nm), show lower attenuation. A second approach is to use two scintillating dyes. The primary dye has a high quantum efficiency to absorb the energy from the base material and the second dye is a wavelength shifter. It absorbs the emission of the primary dye, via radiative or non-radiative transfer, and fluoresces at a longer wavelength where re-absorption in the fibre is less likely to occur [28].

Light yield is typically around 8000 photons/MeV of deposited ionisation energy [30] (no values for Kuraray fibres). Typically, with a SiPM placed near the source, one can observe 15-20 photoelectrons per mm of scintillating fibre traversed by a charged particle.

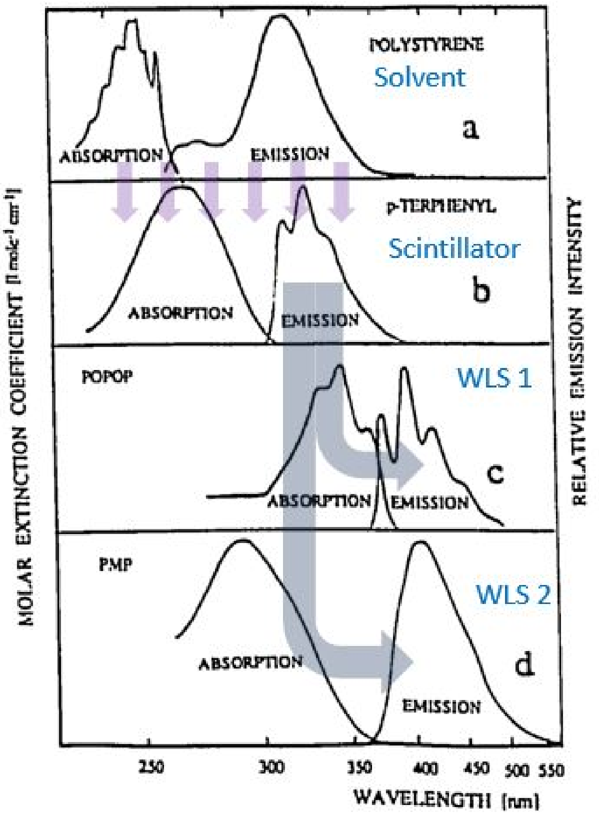

Figure 4.6: Steps of the scintillation process: the ionizing particle gives part of its energy to the solvent (PS core), which in turn transfers it without radiation to the scintillating dye (a–>b). This emits a photon that is then absorbed by the first or the second Wavelength Shifter (usually fibres have just one WLS) and re-emitted in the green region (b–>c) (c–>d). The second WLS, with a more important Stokes shift, offers better performances in terms of attenuation (no self-absorption).
Image taken from H. Leutz, NIM A364 (1995) 422.

4.2 Attenuation Lengths

There is no perfect theoretical model that explains and describes how and why light is attenuated in scintillating fibres. Empirical models and fits, sometimes suggested by the producer, show that the light intensity in the fibre decreases with the distance from the excitation source as a sum of two exponentials [27]:

$$I(z) = I_0 \left(e^{-z/\Lambda_L} + A e^{-z/\Lambda_S} \right) \tag{4.5}$$

where Λ_L and Λ_S represent the attenuation lengths, the long component and the short component respectively. The short component translates the fast attenuation of the helical path and cladding light, while the long component describes a classical attenuation behaviour. Since more than two metres will separate the beam pipe (where the greatest part of the light will be produced) and the read-out, the long component is of greater interest; we will call it by definition the "attenuation length".

Attenuation length's measurements is a fundamental step both for the procurement phase, when fibres to buy must be chosen, and for the successive quality control that every fibre spool will undergo. It is important to know attenuation length before and after irradiation: it has been experimentally seen that the scintillation process and the light yield are not degraded by radiation, while the attenuation length is dramatically decreased by radiation. Even if the measurement itself doesn't present extreme difficulties, we require a very efficient, rapid and mostly automatised experimental set-up for attenuation lengths, especially for non-irradiated fibres.

4.2.1 Non-Irradiated Fibres

We're going to describe now the experimental set-up appositely built for non-irradiated fibre's attenuation length's measurements. In this first section we will not consider the wavelength dependency of attenuation.

Experimental Set-up

To measure light attenuation, light must be introduced in the fibre. We cannot easily excite directly the PS core and activate the scintillation mechanism: a radioactive source would be needed as well as a more complicated set-up, with single photon detectors (see Light Yield 's section). Moreover, we could not get from a direct excitation of the PS the pure attenuation information, but a combination of light yield and attenuation.

What is required is a source which introduces in the fibre light identical to the scintillation light, which can be moved through the fibre to measure the

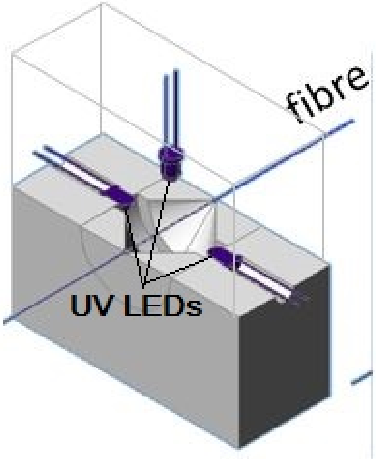

Figure 4.7: 4 UV-LEDs in a Teflon cavity create a homogeneous light and excite the WLS.

light intensity at different distances from the fibre end, which delivers light enough to be measured with a normal PIN photodiode. It was decided to excite the fibre with UV-LEDs having an emission spectrum overlapping the absorption region of the fibre's WLS. The radiation re-emitted by the WLS is in fact the final light of the scintillation process and, therefore the one of what we want to measure the attenuation.

Four UV-LEDs were placed in a Teflon cavity where fibres could slide in. The diffused light inside the cavity guarantees a homogeneous excitation of the fibre's WLS. Fibres were mounted on a rail 3.5 metres long, with an end facing the photodiode and the other mechanically fixed. This end was blackened with AquaDAG to suppress any Fresnel reflection; some centimetres of fibre before the detector were blackened as well, to suppress any cladding light: core light's attenuation was the only quantity we wanted to measure.

Photodiode's current was read through a KEITHLEY picoammeter, connected to the PC with a GPIB. Current values were read every 5-10 cms, moving the excitation source through the rail.

To make this measurement as rapid as possible (fundamental effort for the quality controls previewed in 2015-2016, when hundreds kms of fibres will be measured), a Labview program was appositely written and some hardware prepared. In fact, the few metres separating the PC and the rail make the measurement's duration two or three times longer if the user is supposed to move the source on the rail, go back to the PC and mouse-click to read and save the current value. An electrical switch (a simple button), was so con-

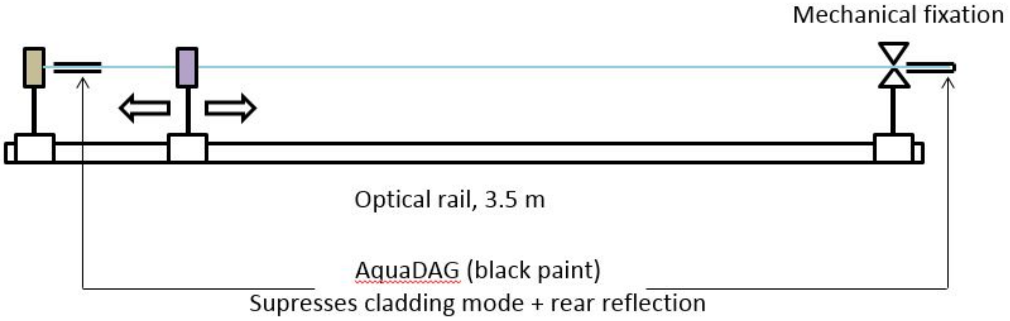

Figure 4.8: Attenuation length set-up

nected to a USB DAQ. When the excitation source is correctly positioned, the user has just to push the button: the program reads the current value, it plots it, an acoustical beep tells the user he can move the source to the next point and, at the end of the rail, the points are fitted to give a first rough value of the attenuation length. A long click deletes the last measured point producing a different acoustical beep, in case the user took a wrong measurement. Finally, the data sheet is automatically saved to be further analysed with more dedicated programs.

Results

A good scintillating fibre should present attenuation lengths' values around 3 metres for the long component and 30-40 cm for the short one. **Kuraray** is actually the only company that can provide such quality standards. Another French-American company, called *Saint Gobain*, sent some free test spools of fibre which turned out to have incredibly high attenuation, with attenuation lengths between 70-200 cm. Fibres with such values are unthinkable to be used in the SciFi Tracker (Fig. 4.9).

To analyse data and especially for data fitting, CERN uses ROOT programs. A ROOT routine was written to fit the recorded data with the double exponential, in order to obtain the best fit parameters. To have a reliable value for attenuation length, **Kuraray** suggests to fit the data taken between 1 to 3 metres from the excitation source with a single exponential, being the short component already mostly attenuated and negligible.

That is what is shown in Fig. 4.10, where the four fibre types, with different WLS's concentrations are compared.

As a general tendancy, it was experimentally seen that the higher the WLS concentration, the lower the attenuation length. Probably the little overlap between the absorption and emission spectra of the WLS is responsible of this greater attenuation when its concentration increases. The only exception

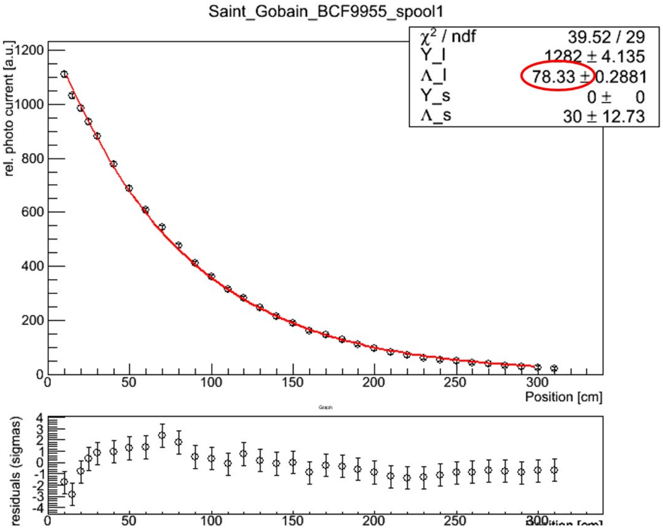

Figure 4.9: Saint Gobain fibre with very low attenuation length

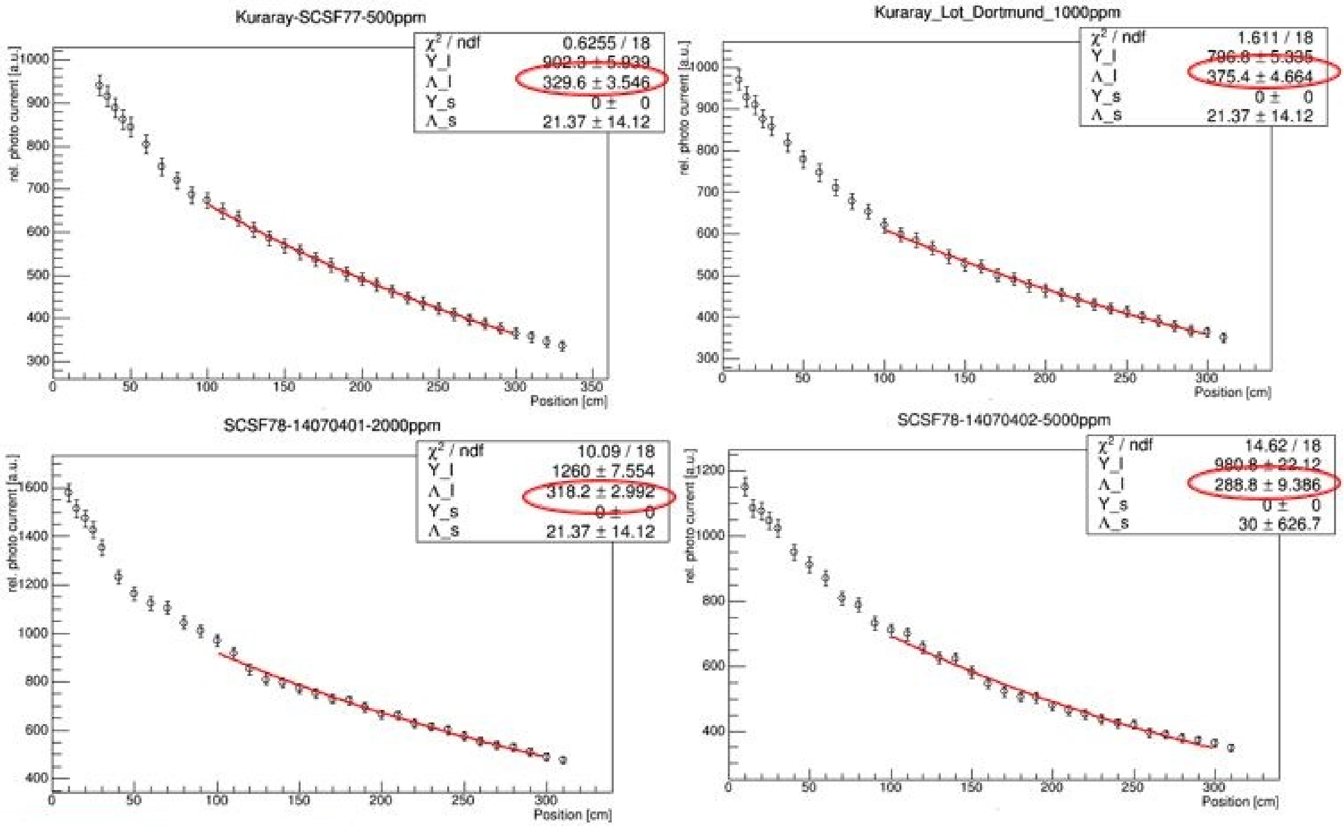

Figure 4.10: Attenuation Lenghts: compared results for different Kuraray Fibres

was reported for the 1000ppm fibre, that is strangely showing the highest attenuation length; this fibre was actually coming from a particular spool (the "Dortmund Spool"), whose fibre was of exceptional quality in terms of attenuation. Other spools with the same concentrations gave lower results.
In any case, the measured values were all more or less in the range 3m ±10% and therefore acceptable for the SciFi tracker: the WLS concentration is not really a critical parameter when attenuation is concerned. Other quantities, light yield in particular, will decide which fibre will be finally used in LHCb.

4.2.2 Irradiated Fibres

The scintillating fibres are exposed in the innermost region of the detector, at about 8 cm from the beam-pipe axis, to an accumulated ionizing radiation dose of approximately 35 kGy after an integrated luminosity of 50 fb^{-1} [21]. The expected dose drops rapidly, both in the horizontal and vertical direction, and becomes relatively marginal (<1 kGy) at distances of about 50 cm [31], as shown in see Fig. 2.4.
Radiation damage to plastic fibres was investigated [32] and the optical changes to the base material resulting in transmission loss were identified as main cause for the degradation of their light output. Radiation damage leads to a reduction of the optical attenuation length. The basic scintillation and wavelength shifting mechanisms are not expected to suffer for the Kuraray SCSF-78MJ fibres.
CERN's previous analysis of the publications on irradiation experiments which have been performed for scintillating fibres or similar polystyrene emitting fibres revealed results that partly disagree. It wasn't possible to extract a clear and definitive conclusion since opinions in literature are vague or contradictory [21, 34].
It is so highly desired to perform radiation experiments and measure attenuation length for fibres irradiated at different doses.

Experimental Set-up

In November 2012. A radiation test was performed in the CERN PS T7 [35, 36] area with 24GeV=c protons on a plexiglass test plate which contained an arrangement of 8 1000ppm SCSF-78MJ fibres of 2.94m length on a 1m polycarbonate plate. The fibres are laid in straight channels on the plate and then turned back at the ends of the plate with a bending radii of 12 cm, resulting in four 75 cm long segments. An epoxy glue which doesn't harm plastic fibres, the same previewed for final fibre mats, was here used.

Every leg was exposed to a different radiation. Leg 1 and leg 2 were exposed only to a neutron background radiation. We can estimate that they received a poor and negligible ionisation dose. Only leg 3 and leg 4 were exposed directly to protons. Leg 3 received approximately 3 kGy and leg 4 approximately 22 kGy.
The necessary excitation for attenuation length measurements was provided by a UV LED (exciting the WLS), manually positioned at different distances from the PIN diode used for read-out positioned at the fibres' end.
A first attenuation length measurement was performed just after irradiation in November 2012 and a new one was repeated in May 2014, looking for some possible annealing effects.

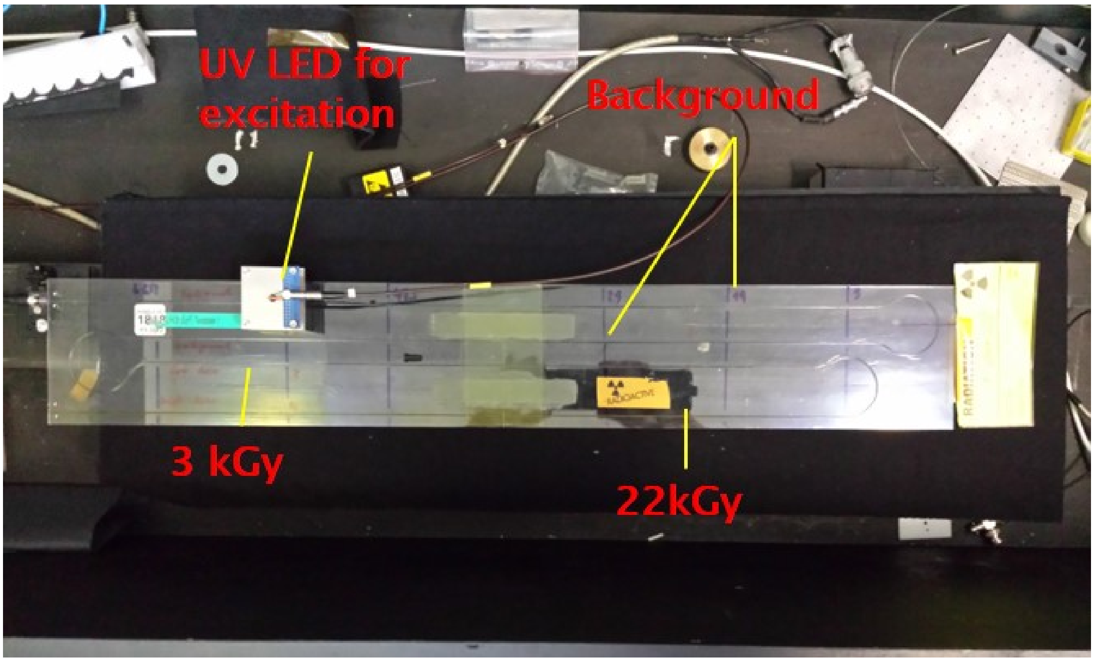

Figure 4.11: Irradiation plate for attenuation length measurements

Results

One can see (Fig. 4.12) a sensible effect on attenuation due to radiation. The background region is in fact not dramatically involved as the irradiated regions in the reduction of the attenuation length. It is actually decreasing from respectively 126cm (3 kGy) to 52cm (22 kGy). No annealing effect has been remarked: the points measured in the same experimental conditions in 2012 and 2014 are consistent.

No annealing has been documented, even if a small effect was previewed. A possible reason is that glue is preventing oxygen to penetrate into the fibre. Oxygen could in fact reduce the radicals formed by radiation in the fibre and allow a partial reparation of the radiation damages.

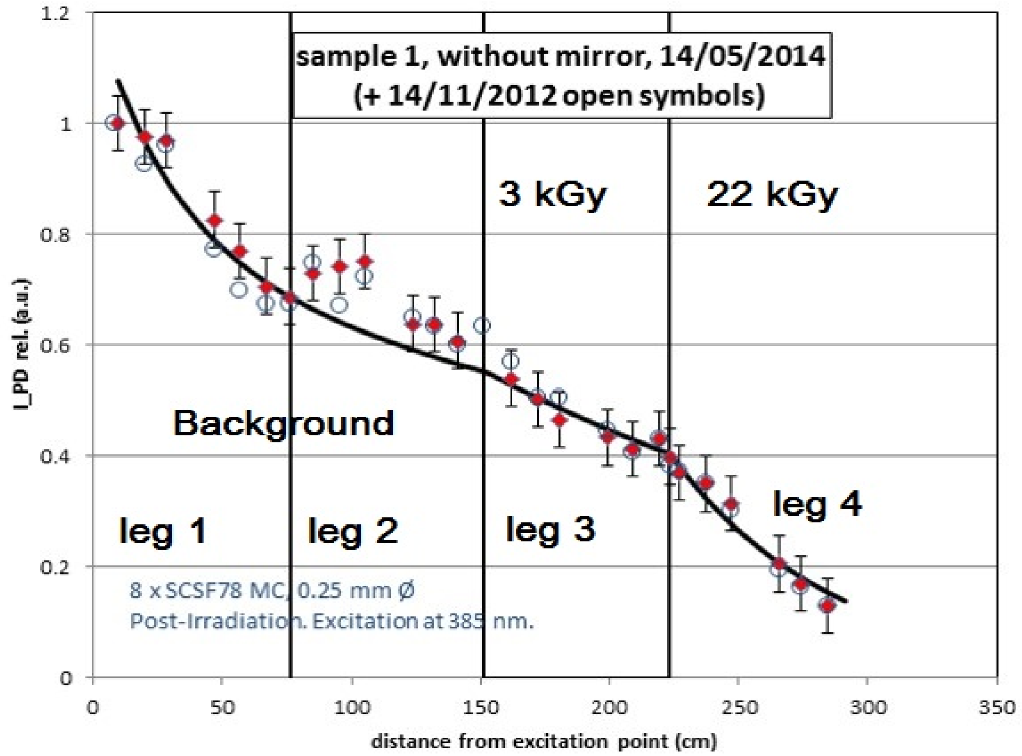

Figure 4.12: Attenuation for different radiation doses. The apparently increasing light passing from leg 1 to leg 2 (background) is due to the curvature of the fibre inside the plexiglass

At this stage a measurement of the radiation damage on scintillating fibres at low doses (<1 kGy) is still missing. Different models try to extrapolate the ratio of the attenuation lengths $\Lambda'(Dose)/\Lambda_0$ at low doses from the available experimental points, but they often disagree and show sometimes non-physical results (i.e. a logarithmic model that is previewing infinite attenuation length at zero dose [33]). Fibres in the SciFi tracker will experiment low dose for the greatest part of their length and therefore is crucial to discover their reaction to such a radiation: it is planned to experimentally obtain this information at CERN in the second part of 2014.

4.3 Emission and Absorption Spectra

The spectral content of the light coming out at the fibre end is determined by its emission and absorption spectra. This light should be perfectly known to eventually tune SiPM's PDE on it.
Attenuation length is strongly wavelength dependent due to reabsorption of the shorter blue wavelengths by the scintillation dyes, Rayleigh scattering, and some discrete absorption of higher wavelengths by the polystyrene. Spectra have been measured for irradiated and non-irradiated fibres. Clear fibres (without scintillator and WLS) were measured too.

4.3.1 Non-Irradiated Fibres

Emission Spectra

Non-irradiated fibre's emission spectrum was obtained by simply exciting the fibre with the 4 UV LEDs in the teflon cavity, coupling one fibre end with a 1 metre long quartz fibre (with flat and almost negligible spectral attenuation) carrying light inside an optical spectrometer. The distance excitation point - fibre end was kept at 1 metre, to let the cladding light and the helical paths be already attenuated. A second measurement was then taken at two metres distance. From the comparison between the two measurement one can know the attenuation. Typical spectra can be seen in Fig. 4.13 and Fig. 4.14.
The significant light content is limited in the range 420-600 nm, with a peak intensity at ≈ 460 nm. At 200cm from the excitation source the spectrum's

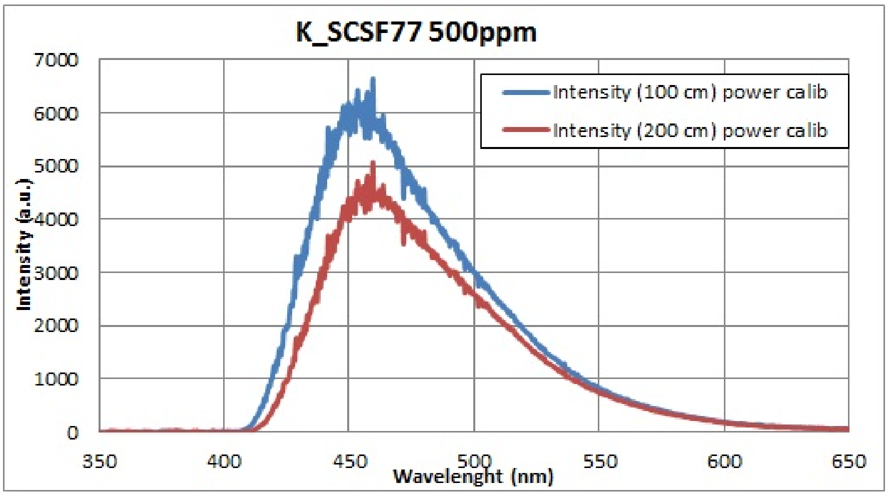

Figure 4.13: Emission spectra for a Kuraray 500ppm fibre.

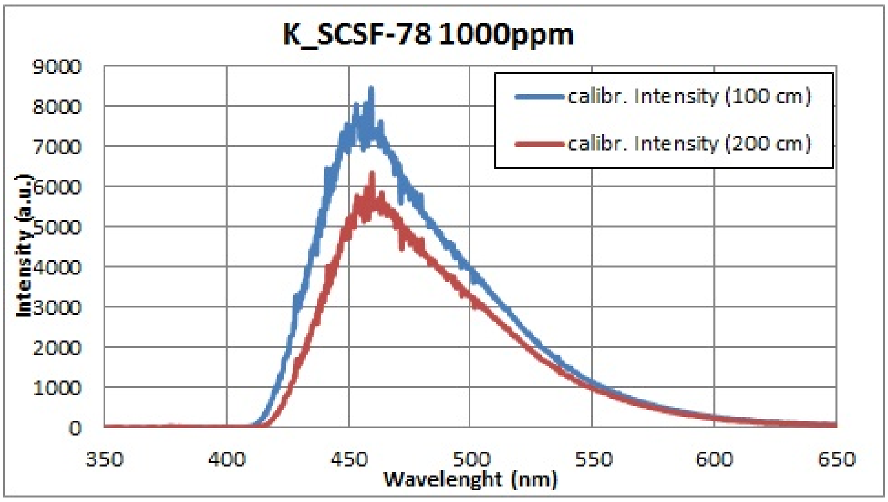

Figure 4.14: Emission spectra for a Kuraray 1000ppm fibre.

peak is green shifted: blue light seems to be more attenuated as previewed; no significant spectral differences seem to appear due to the different WLS concentration: just a very slight green shift is observed with the increasing WLS's concentration (Fig. 4.15).

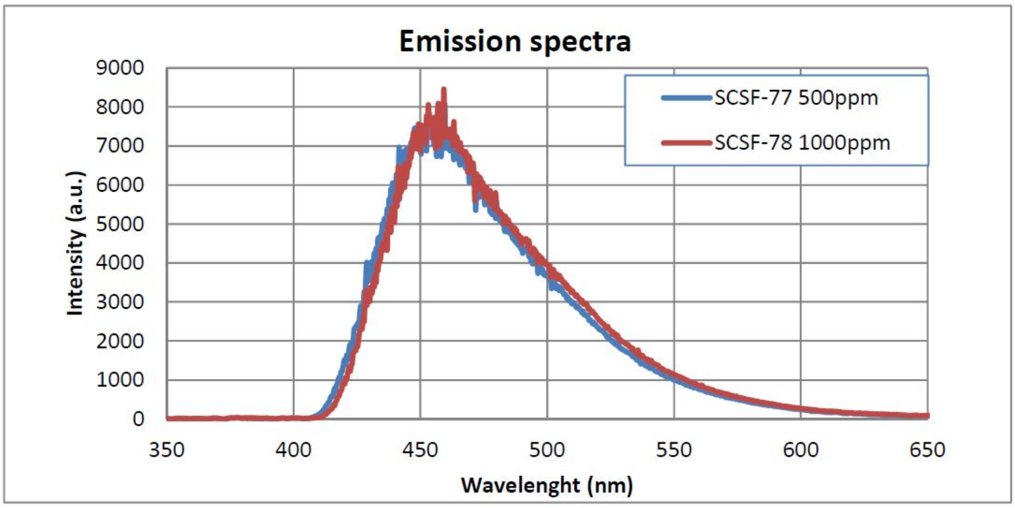

Figure 4.15: Superposed and scaled emisision spectra for a Kuraray SCSF 500ppm and 1000ppm.

Absorption Spectra

In principle two spectra, measured at different distances ($z_1 = 100cm$ and $z_2 = 200cm$) from the excitation point, allow us to determine the attenuation length for each λ. If we consider the double exponential model for attenuation and the short component already negligible at 100cm from the source (reasonable, since we have $\Lambda_S \approx 30cm$) one can say:

$$\Lambda_L(\lambda) = \frac{(z_2 - z_1)}{ln\left(\frac{I_1(\lambda;z_1)}{I_2(\lambda);z_2)}\right)} \tag{4.6}$$

When we plot the attenuation length for each λ or the attenuation factor (that is simply $100/\Lambda_L$, expressed in m^{-1}) one finds that short wavelengths are more attenuated in the fibre, that is exactly what was qualitatively expected. Rayleigh scattering shows in fact a cross section $\propto \lambda^{-4}$ and re-absorption due to overlapping WLS absorption and emission spectra is of course more likely to occur at low emitted wavelengths. Those attenuation measurement confirm a slight lower attenuation for fibres with lower WLS concentration, especially in the region 500-550 nm. This was unexpected, since no absorption from the WLS should happen in that spectral region. But, since the material is not revealed by Kuraray, we don't know perfectly its absorption spectrum and we cannot exclude that it presents no absorption at 500-550 nm.

Even if the data collected at CERN in Spring 2014 and just shown confirm a higher attenuation for the blue region, they don't match quantitatively with what was previously measured and simulated by other institutes (i.e. Heidelberg University). They were expecting much higher attenuations at low wavelengths than we found (see Fig. It is not clear whether CERN or

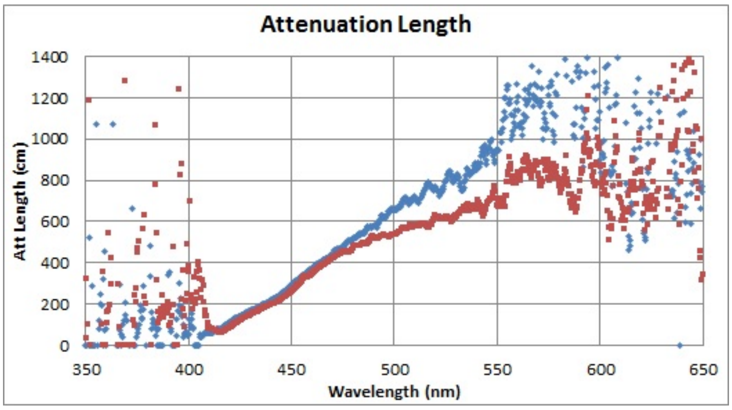

Figure 4.16: Attenuation for SCSF-78 1000ppm (red) and SCSF-77 500ppm (blue).

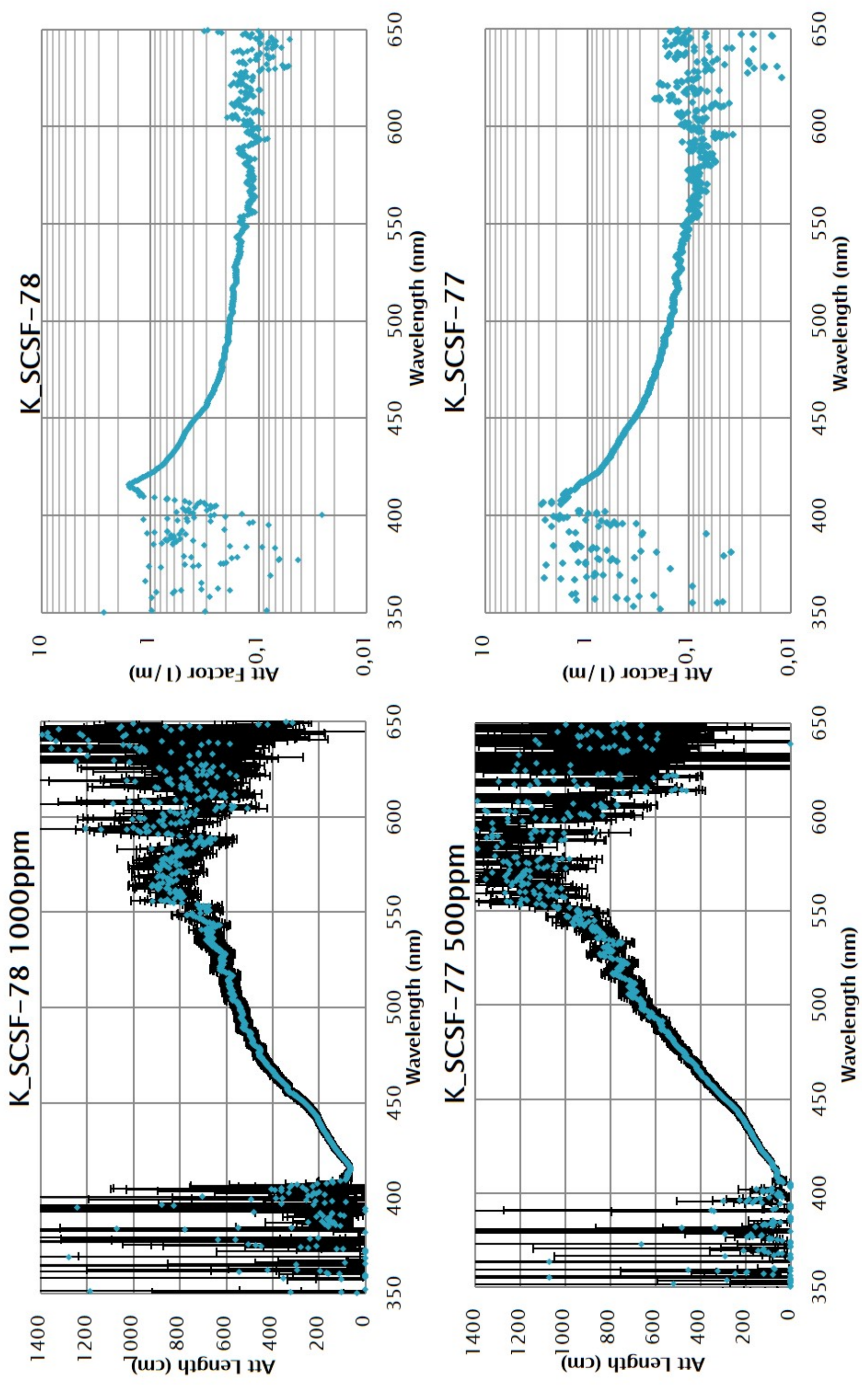

Figure 4.17: Attenuation lengths (lambda) and attenuation factors (lambda)

Heidelberg or both present incorrect results. It was so decided to investigate a clear fibre of pure polystyrene (without any scintillator nor WLS) to better separate spectral contributions to the final absorption and to understand if the discrepancy in the blue is due to PS or to the WLS.4.18).

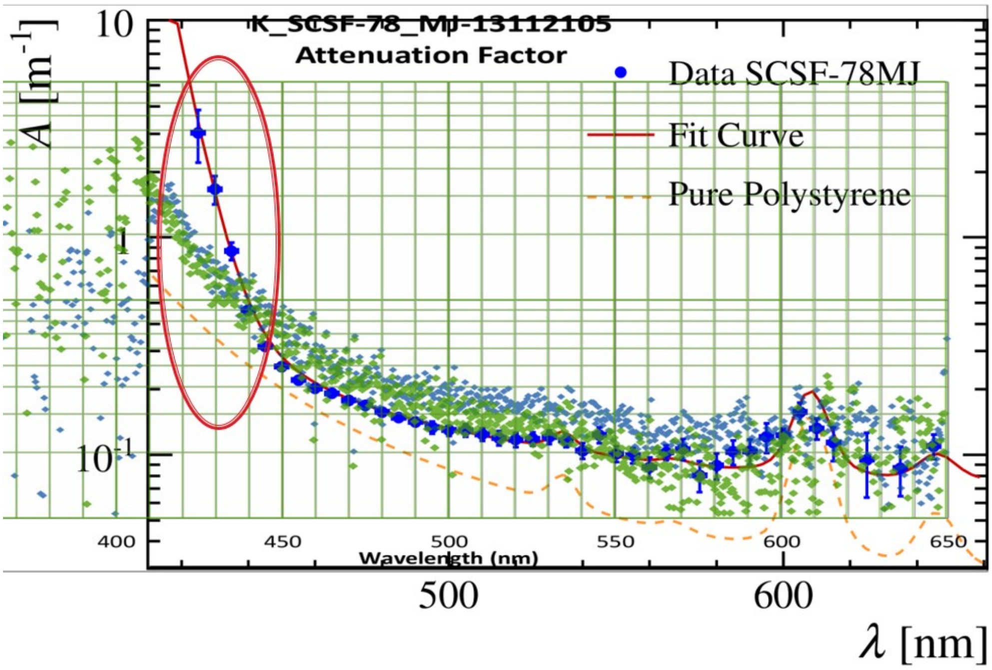

Figure 4.18: Disagreement at small wavelengths between CERN measurement (green and blue small points) and Heidelberg measurement (big blue points).

4.3.2 Clear Fibre

Attenuation length measurements for clear fibres were performed using the same method described for scintillating fibres: two spectra at different distances from the excitation light were taken and, through the logarithm of the ratio of the two and the distance, we obtained the attenuation length.
The hardware had anyway to be modified since a clear fibre cannot be excited with UV LEDs, being the scintillation mechanism absent. A thermal QTH lamp (produced by ORIEL) with white spectrum was used to inject light at one fibre's end, while the other was coupled to the quartz fibre and therefore the spectrometer. The experimental conditions were supposed not to change between the two spectral measurements as the smallest difference would make senseless the ratio of the two spectra to obtain the attenuation length. The

lamp was so maintained at the same power and the coupling quartz fibre-clear fibre was left untouched. The clear fibre was provided with two lamp coupler glued at predetermined positions. To have a standard cut for the fibre's end facing the lamp, the fibre was cut with a micro-guillotine. After the first measurement, the fibre was cut (always with the micro-guillotine) in correspondence of the second fibre-lamp coupler and the second spectrum was measured. A scheme of the full set-up is visible in Fig. 4.19. These

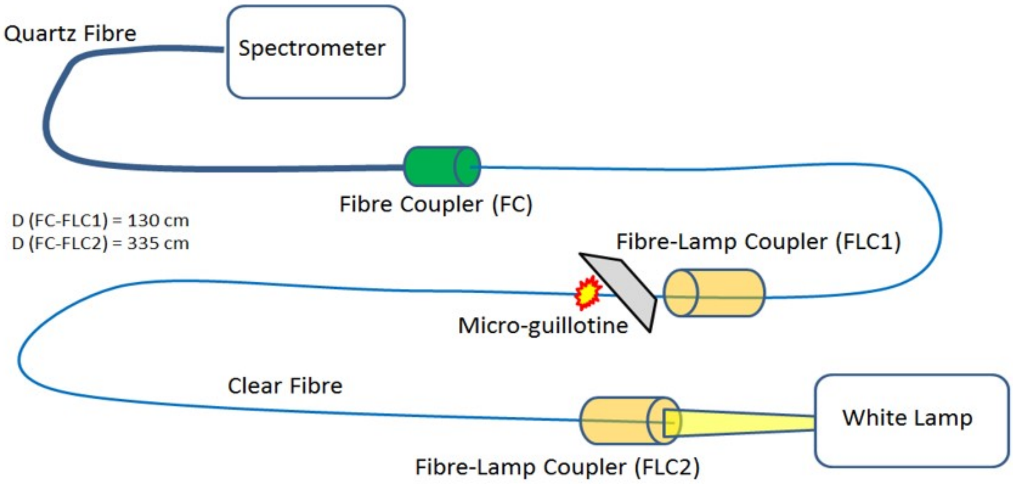

Figure 4.19: Experimental set-up for clear fibre's absorption measurements.

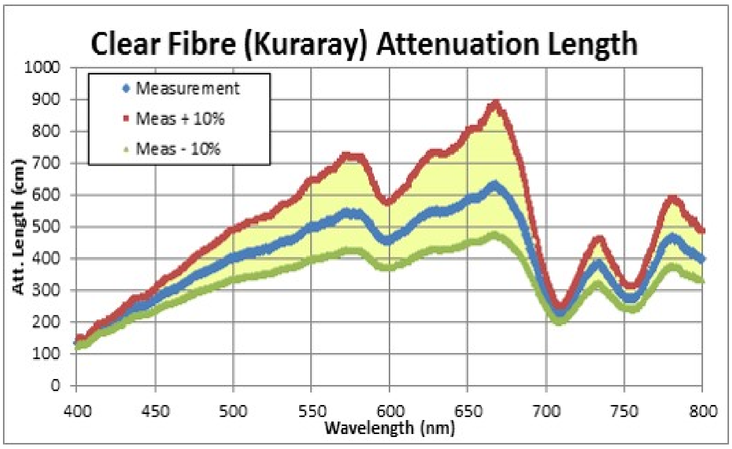

Figure 4.20: Clear fibre's attenuation length:

measurements gave surprising results, showing lower attenuation lengths all over the spectrum for the clear fibre when compared to the SCSF-77 and

SCSF-78 (Fig. 4.20). In principle the clear fibre is supposed to show larger values than a scintillating fibre, but here it is ≈20% lower. Even assuming a 10% error (due to the non-optimal reproducibility of the experimental conditions, translated in a ±10% for the intensity ratio) the attenuation length stays below the expectations.

When compared to the data Kuraray is showing on its catalogue regarding clear fibres, the one measured at CERN is clearly more attenuating (Fig. 4.21).

Kuraray was asked for clarifications and possible explanations for this discrepancy. The answer was that the clear fibre CERN was given may not be the correct one. When Kuraray sent to CERN as an example a new type of fibre spool, they put some clear fibre on it (the one we measured), without paying attention of which fibre it was.

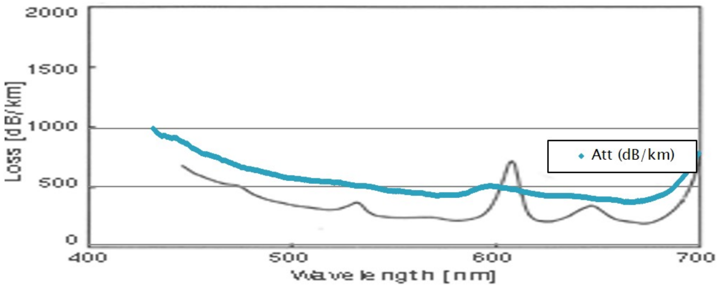

Figure 4.21: Comparison between the Kuraray catalogue (black) and the measured attenuation (blue).

As a conclusion we still cannot explain the diverging behaviour at short λs for the scintillating fibre's attenuation, if it is a real effect or a wrong measurement and, if it is correct, if it is due to the polystyrene or to the WLS. Even if our clear fibre couldn't solve the problem, according the Kuraray catalogue for the pure PS fibres, it seems that pure PS is not responsible of the extra absorption.

4.3.3 Irradiated Fibres

Emission and absorption spectra of irradiated fibres have been measured.

The same plexiglass test plate containing a standard Kuraray SCSF-78 1000ppm and irradiated in November 2012 was used (Fig. 4.11. Attenuation length and attenuation factor were obtained by the same procedure used for the non-irradiated fibre: UV LEDs for WLS excitation, ratio between light intensities at different distances from excitation to get the attenuation. We considered a single exponential to describe the attenuation for irradiated fibres: starting

from leg 3, the fibre is already ≈ 150cm long and we can neglect the short component of the double exponential model; moreover radiation is reducing attenuation lengths, making this approximation even more precise.
Concerning emission spectra, the experiment confirmed that radiation is not significantly harming the scintillation process and its spectral content is not modified.

The general attenuation length's reduction at all wavelengths (more dramatic in the blue region) is also confirmed. At 460 nm, were we had the

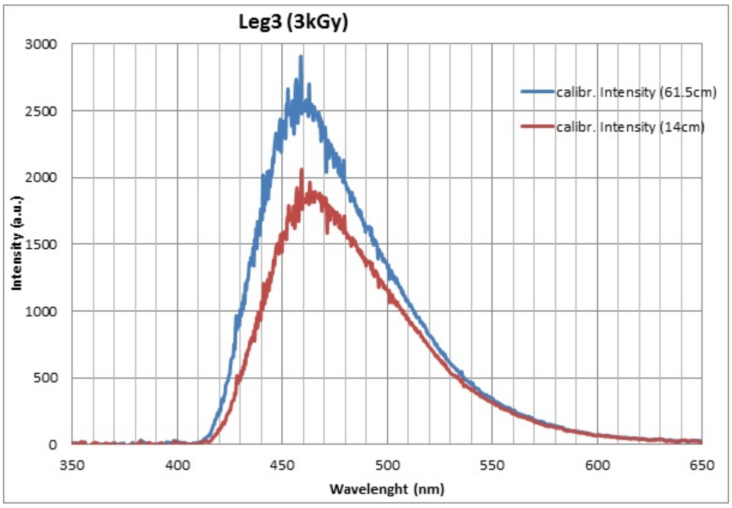

Figure 4.22: Emission spectrum of the 3kGy-irradiated fibre

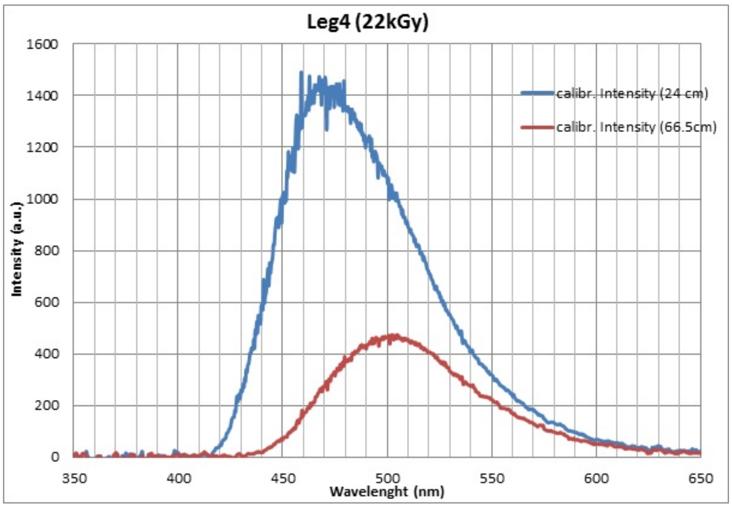

Figure 4.23: Emission spectrum of the 22kGy-irradiated fibre: the peak value has shifted to 500nm due to wavelengths' different absorption

emission peak, the attenuation length is passing from the ≈400cm of the non irradiated fibre to the 100cm at 3 kGy and to the ≈ 20cm at 22 kGy. The emission spectrum coming out at the fibre after propagation through leg4, leg3 and two background legs show a shifted peak at 500nm.

A dose dependency for attenuation has been searched. Empirically, without any physical explanation or simulated result, we found that a sublinear

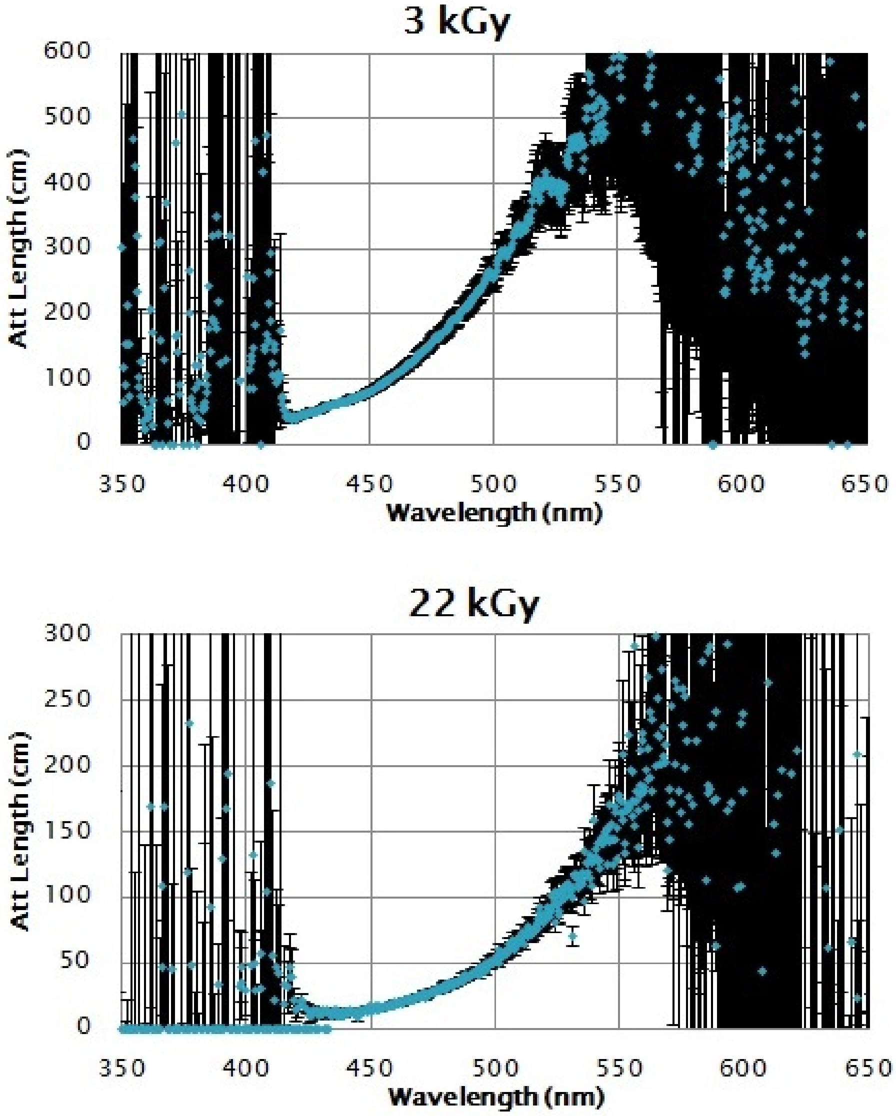

Figure 4.24: Attenuation length of fibres irradiated at 3 and 22 kGy

relation between the attenuation factor and the dose seems to exist:

$$AttFactor(\lambda) = C \cdot Dose^{\alpha} \tag{4.7}$$

Always empirically, if we express the dose in kGy, we found 0.85 as an optimal value for α (Fig. 4.25). Still, two measurement at two different doses only are not enough to trust this kind of sublinear relation. The next necessary effort will be, as already discussed, to discover the fibre's reaction to a low dose radiation (many points between 100-1000 Gy).

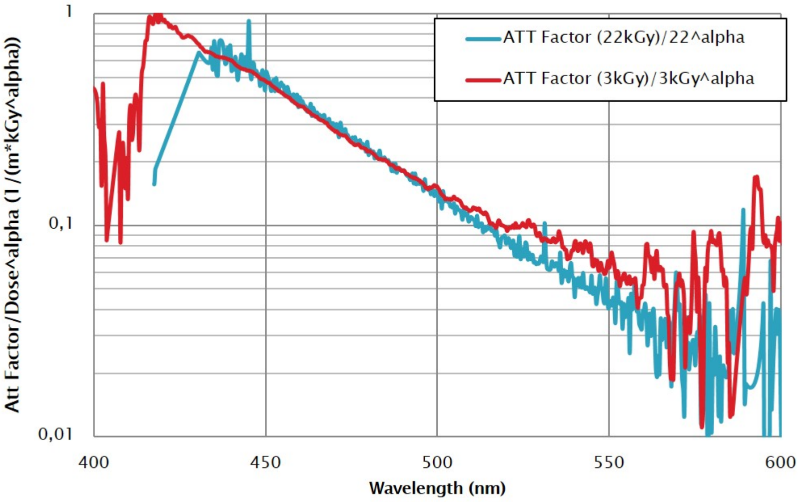

Figure 4.25: Sublinear relation between the attenuation factor and the radiation's dose. alpha = 0.85

4.4 Light Yield

Up to now, we never tested the scintillation properties of fibres.
We define Light Yield (LY) as the most probable number of photons (N_{pe}, that become Photo-Electrons in the photodetector) generated through scintillation mechanisms (when the fibre is traversed by a single charged particle) and propagating into the fibre until its end in front of the detector. LY isn't for us an absolute value, as N_{pe} depends on the distance between the excitation point and the detector's read-out (see attenuation lengths).
This quantity is part of the final figure of merit that will determine the best fibre to be installed in the LHCb SciFi tracker and is one of the key parameters that an accurate quality control will test for almost every fibre spool during the procurement phase.
We built an experimental set-up that can measure LY with good reproducibility and errors in the 10% range.
In the conception of this experiment, we kept in mind that LY measurements require:

- A reliable and controlled source of charged particles to simulate in a smaller scale the beam in LHCb.
- Sufficient light intensity for read-out.
- Extreme mechanical precision for the whole set-up.
- High quality photodetectors with low noise level.
- Efficient trigger system.
- A theoretical model to fit the signal's curve and obtain the N_{pe}.

4.4.1 Electron Monochromator

To produce the scintillation light in laboratory set-ups, electron sources are generally used, in particular the b emitting ^{90}Sr isotope [39], which in combination with the decay of the daughter nucleus Y-90 provides a continuous electron energy spectrum extending up to ≈ 2.2 MeV (Fig. 4.26). [37]
Electrons above ≈ 1 MeV can be considered MIPs (Minimum Ionizing Particles) and can traverse up to few mm of scintillating PS. Therefore, the goal is to prevent electrons of lower energy from reaching the fibre under test, which can be done by selecting the electron momentum using a magnetic field. We're going now to briefly describe how such a solution is implemented in the form of a compact electron monochromator.

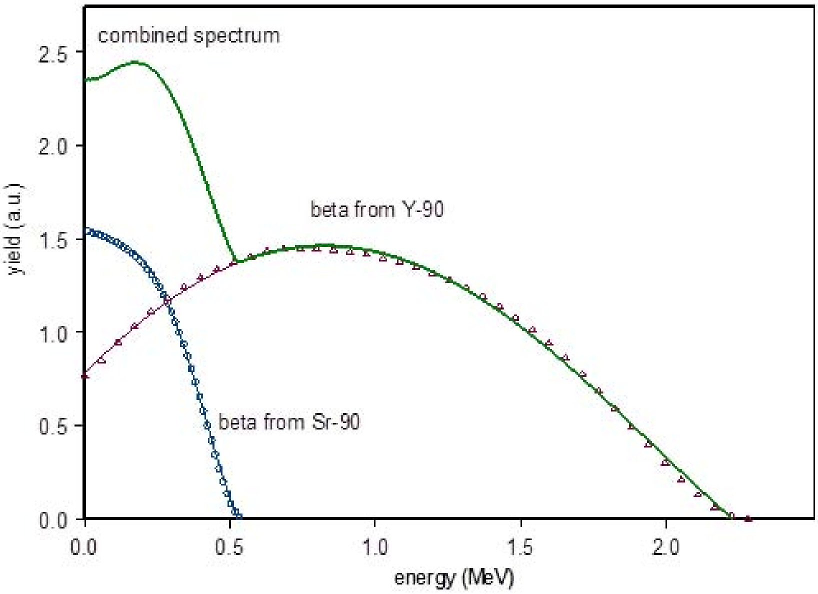

Figure 4.26: ^{90}Sr Emission spectrum

The device described here is based on the original design by the *Institut de Recherches Subatomiques, Strasbourg, France.* From their technical drawings, the manufacturing of the tungsten pieces was externally contracted, all other components were fabricated at CERN. The ^{90}Sr source itself was inserted by CERN's radioprotection group.

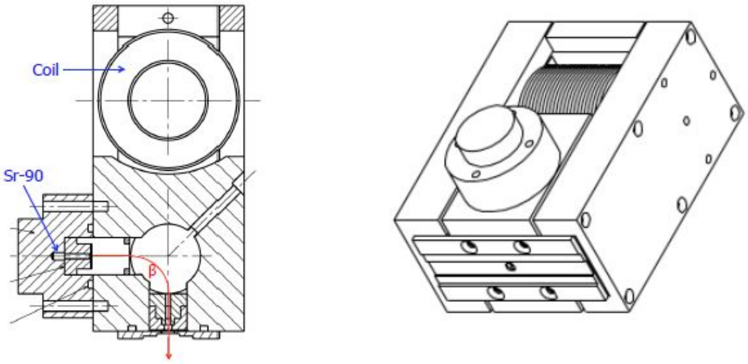

Figure 4.27: Electron monochromator

The electron monochromator, illustrated on Fig. 4.27, consists of three main parts. The body is made of tungsten which ensures efficient shielding in all directions. The source housing, which contains the ≈ 370 MBq ^{90}Sr

source, is also made of tungsten and is permanently bolted to the side of the main body. The solenoid coil, mounted on top of the main body, is made of 16 layers of 0.80 mm coated copper wires, arranged in 56 windings per layer. Moreover, the coil is equipped with an ARMCO soft iron core to enhance the generated magnetic field. A cavity inside the main body allows the electrons to travel from the source casing and, in the presence of a magnetic field, bend towards the exit hole on the bottom side of the body. The magnetic field is guided to the cavity via soft iron bars on the sides and additional soft iron cylinders on the level of the cavity. When no current is applied to the solenoid, the electrons coming out from the source casing are stopped inside the tungsten structure.
Proper use of the device requires to know the relation between the solenoid current and the electron momentum, as well as the emission rate of the selected momenta.

M1 and M2 monochromators

Two monochromators were built and equipped with two ^{90}Sr sources. The first (M1) was previously characterised and is currently used for experiments that don't involve the SciFi tracker. The second (M2) was firstly characterised and used for the LY measurements.
Nominally identical, the two monochromators show different responses when the same current is applied. Micro mechanical irregularities provide different magnetic resistances in the soft iron circuit for the $\vec{B}$ field and the ^{90}Sr sources are delivered with a 30% uncertainty on their radioactivity.
We chose the operating point of the monochromator in order to obtain the highest rate of emitted particles. Even if the source shows high radioactivity, only a small fraction of the 370 MBq can be used: the exit slot is narrow while the emission is over 4π and the magnetic field is selecting a little part of the emitted radiation.
For M1 and M2, we first determined the magnetic field corresponding at the highest emission rate (Fig. 4.28) and then searched the solenoid current that gives the desired Magnetic field (Fig. 4.29).
The maximum rate is reached for both M1 and M2 at $\approx$ 3-4 kGauss According to Fig. 4.30, this corresponds to a solenoid current of $\approx$ 1.1A for M1 and 0.8A for M2.

Looking at Fig. 4.30, this means a momentum of $\approx$ 1.65 MeV/**c**. Using the relativistic expression for the total energy, with m_0=511keV the electron's

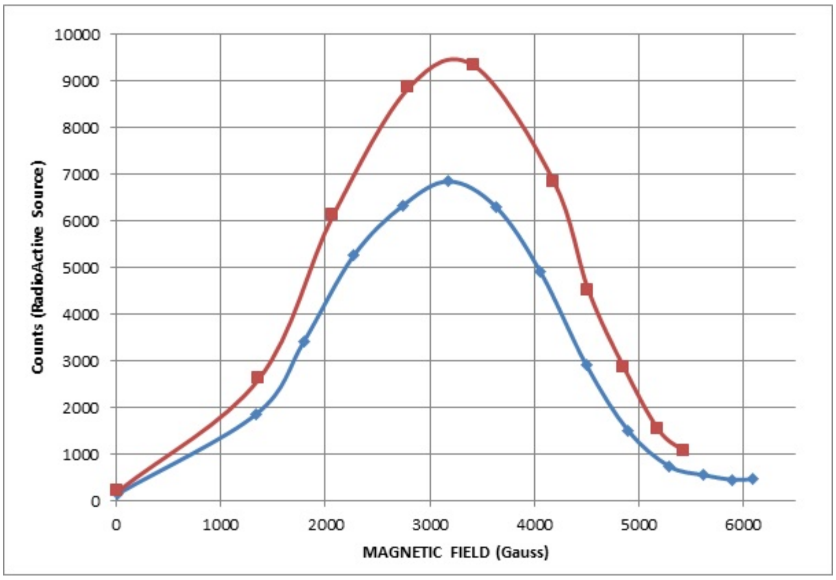

Figure 4.28: Emission rate for M1 (red) and M2 (blue) as a function of the magnetic field. The monochromator used for the LY measurements (M2) provides a rate on average $\approx 30\%$ lower than M1.

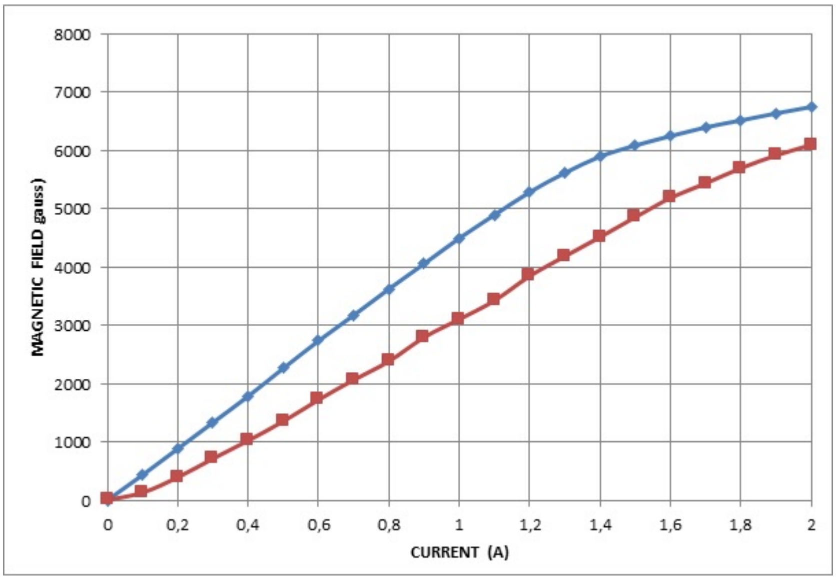

Figure 4.29: Magnetic field measured in the source housing as a function of the applied current for M1 (red) and M2 (blue).

rest energy:

$$E = m_0c^2 + K = \sqrt{p^2c^2 + m_0^2 + c^4} \tag{4.8}$$

and normalizing everything to c, we obtain:

$$p = \sqrt{(K + m_0)^2 - m_0^2} \tag{4.9}$$

Solving the quadratic equation, we obtain $K \cong 1.2$MeV. Electrons with such an energy are MIP. Those electrons formed the simulated beam we used for LY measurement.

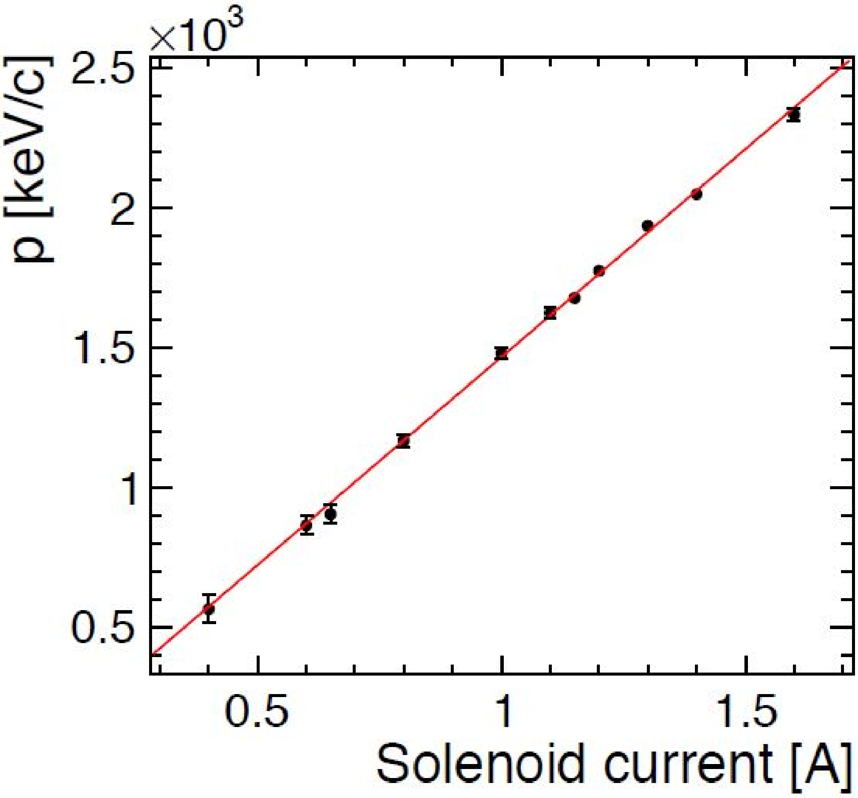

Figure 4.30: Electron momentum as a function of the solenoid current. The curve corresponds to M1 and is linearly fitted [37].

4.4.2 Experimental set-up for LY measurements

A complex set-up that involved realisation of extremely precise mechanical pieces, electronic circuits and optimized geometry was designed to provide reliable LY measurements.

Photodtectors

Hamamatsu PMT H7826 (Photo-Multiplicators Tubes) were chosen as photodetectors. The were preferred to SiPM for their extremely low dark noise. PMT's gain was controlled through a potentiometer appositely designed. When the PMT is supplied with $\approx$ 15V, it generates a 1.2V signal and asks for a control voltage from 0 to 1.2V (1.2V means maximal gain). We put a 10kΩ rheostat in the potentiometer and a sliding contact with 1000 positions to control the gain (see fig. 4.31).

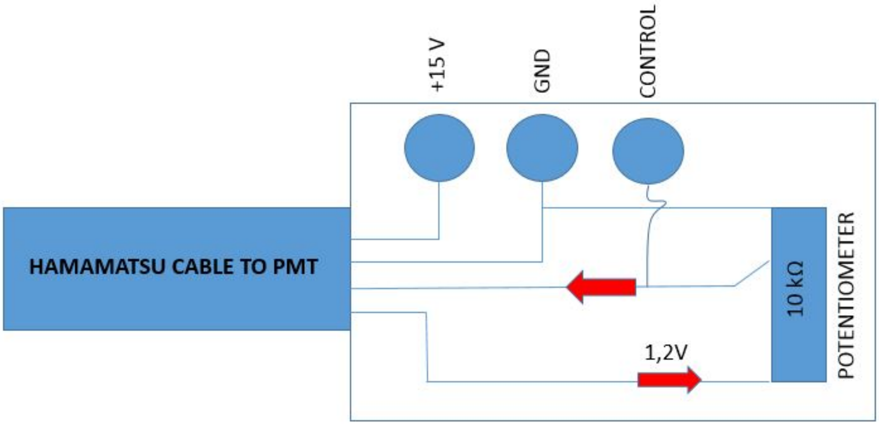

Figure 4.31: Control circuit for Hamamatsu PMTs

Geometry

PMTs are very sensitive detectors, but the light signal coming from a single fibre traversed by one charged particle is still difficult to recognize, especially if the distance excitation-detector increases (less than 1 photo-electron). To increase the signal four fibres were piled up. The four fibres are glued together (epoxy glue not attacking plastics) with an end-piece connected to the read-out PMT. We use two trigger fibres: one below and one above the 4 signal fibres. Every trigger fibre is read separately by a PMT (but the two trigger PMTs are controlled by the same potentiometer). Precise geometrical positioning of small objects (we remind that fibres have just 0.25mm diamater) is the greatest issue of this configuration. We want that every electron coming out from the monochromator passes through the 6 fibres . Precise alignment is maintained by a stack of 3 elements: the first and the last are housing the trigger fibres in groves while the central element is $\approx$ 1mm thick and made of two half elements. They leave, when mounted,

≈0.27mm between them creating a trench for the 4 signal fibres(Fig. 4.32). The signal and trigger fibres are optically isolated by a tape 0.04mm thick which is not blocking electrons.
The stack is then mounted on the monochromator's upper face(Fig. 4.33).

We wanted to measure LY at different distances excitation-detector to better simulate the ≈ 250cm height of the final fibre module in the SciFi tracker. To create reproducible conditions for fibre positioning, a disk of exactly 30 cm circumference was used to coil the fibres.

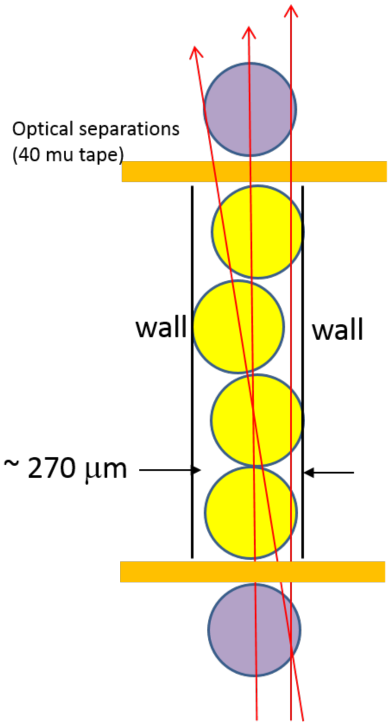

Figure 4.32: Layout of the fibre positioning in the LY measurements. Trigger fibres in purple, signal fibres in yellow. Electrons' trajectories in red.

Read-out

We collect the scintillation light from the 4 signal fibres and read on a digital oscilloscope the voltage signal coming from the dedicated PMT. The number of photo-electrons for each scintillating event can be determined integrating the PMT's signal: the total charge of the signal (normalized to the 50Ω resistance) is proportional to the PMT's gain for one single photoelectron

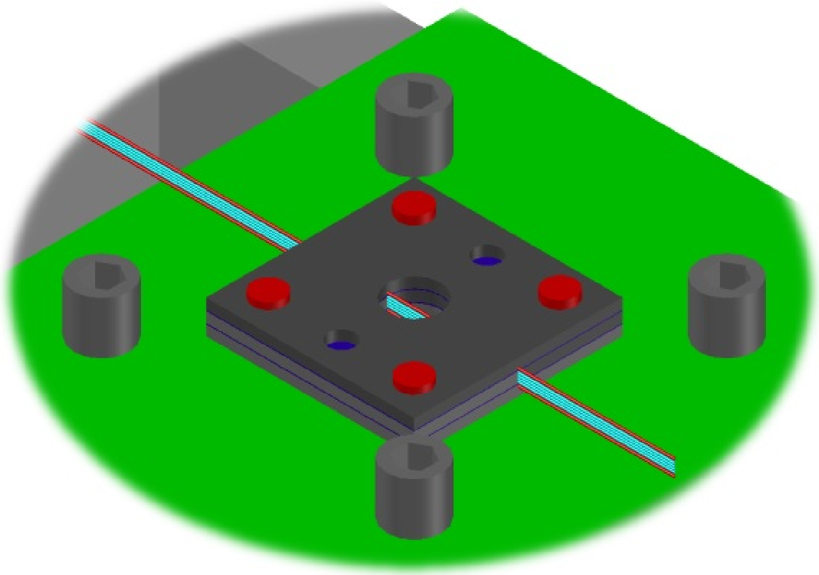

Figure 4.33: Signal (light blue) and trigger (red) fibres mounted on the top face of the electron monochromator

(G_{1pe}) and to N_{pe}.

$$\int_{-\infty}^{+\infty} S_{PMT} = G_{1pe} * N_{pe} \tag{4.10}$$

Once we know G_{1pe}, we collect a significant statistics of events to create a continuous spectrum and calculate the $\langle N_{pe} \rangle$.

To measure G_{1pe} the signal PMT was enlightened with a very low intensity pulsed LED. The read-out on the oscilloscope was triggered at every LED pulse. Normally, due to low light intensity, no photons were reaching the PMT (see Fig. 4.34) giving a pedestal peak in the spectrum. With lower probability, 1 photon could reach the PMT (negligible probability that 2 or more photons could be seen by the PMT). In the spectrum we recognize the 1 pe peak. The calibration spectrum was fitted with a sum of two Gaussian distributions; the centre of the second one corresponds to G_{1pe}. This value was fixed to ≈35 pV*s.

Trigger

The experiment takes place in a dark room and PMTs show low DCR. Still, without a properly designed trigger, the charge spectrum would be mostly polluted by noise events.

We must record the integral of the signal only when we're sure that it is due

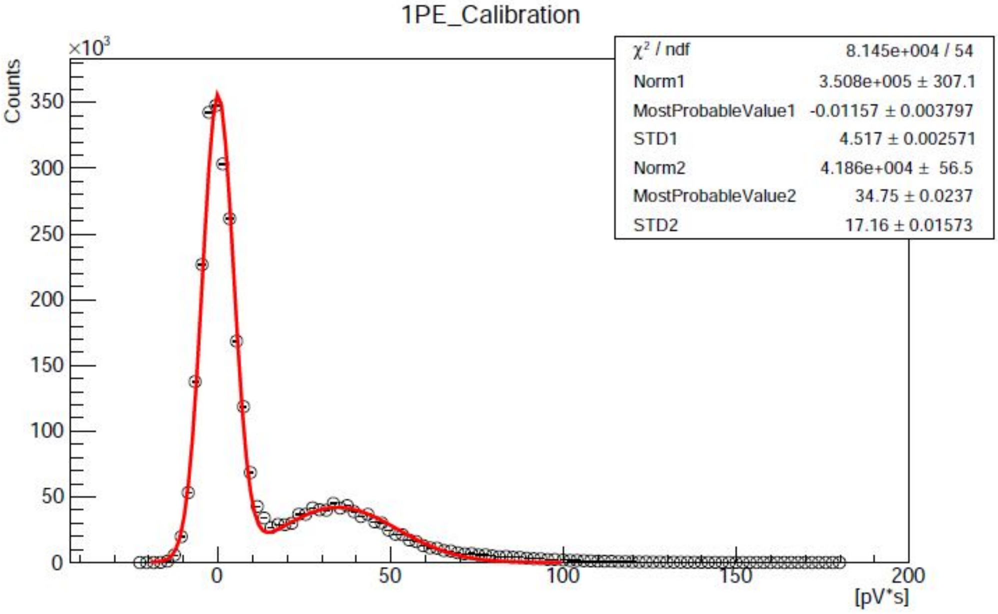

Figure 4.34: 1 pe calibration. $G_{1pe} = 34.75$ pVs. $\sigma_{1pe} = \sqrt{STD2^2 - STD1^2} \cong 16.6$ pVs

to a particle passing through all the 4 signal fibres. The geometry of the experiment was designed with this purposes: if both the trigger PMTs see a simultaneous event a particle must have passed through the upper and lower fibre of the stack (DCR $<$ 10-20 Hz make two simultaneous noise events improbable to occur), meaning that the electron necessarily traversed the signal fibres.
A logical trigger circuit was designed (taking inspiration from [38] and implemented: the trigger PMTs' signals are amplified and sent to a threshold discriminators with digital ouput signals (0 and 1). Those two signals are connected to a logical AND and whose output is the final trigger for the 4-fibre signal.

4.4.3 Statistical Model and Fits

The digital oscilloscope (Lecroy LT344) creates histograms of the integrated signals that can be further be analysed (Fig. 4.37).
We extract $\langle N_{pe} \rangle$ from histograms with two methods:

1. We consider $\langle N_{pe} \rangle$ as the Centre Of Gravity (COG) of the spectrum without the pedestal.

2. We look for a theoretical model describing the spectrum's shape with

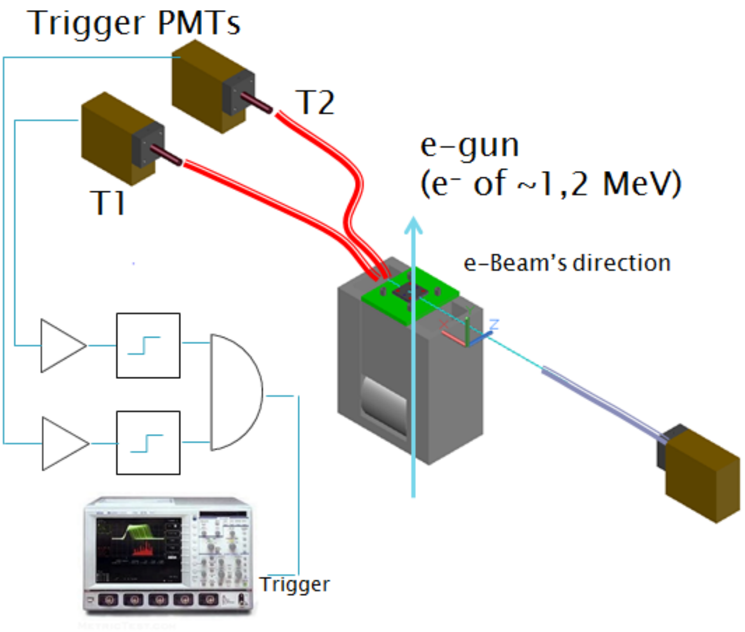

Figure 4.35: LY final set up and trigger circuit.

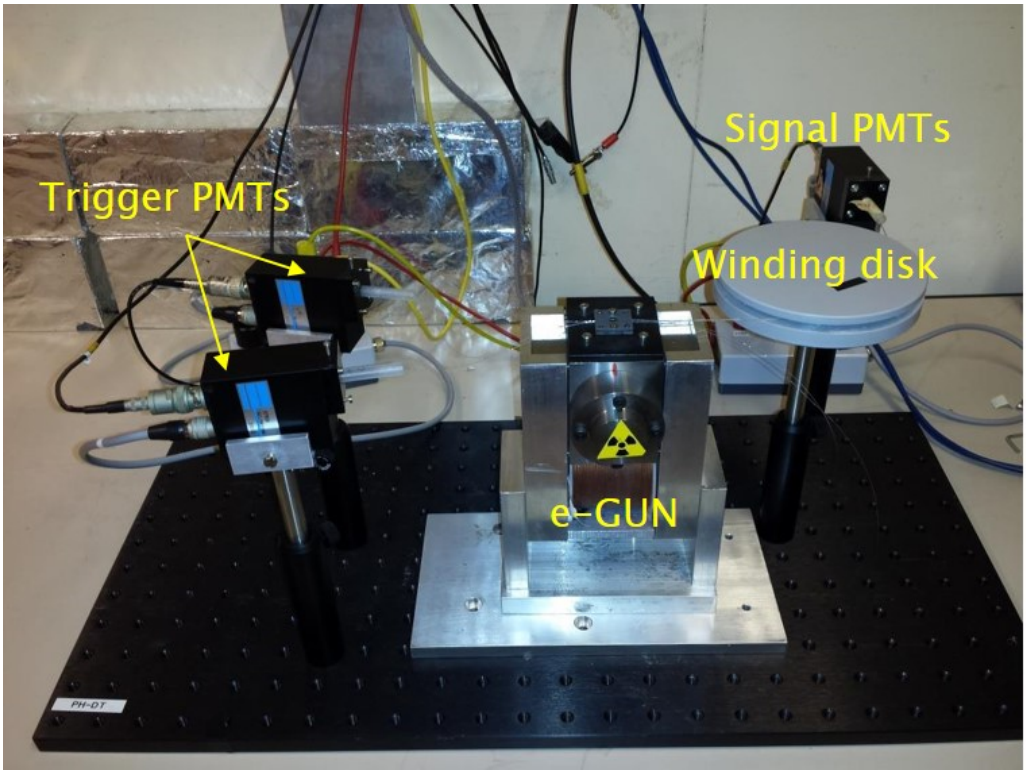

Figure 4.36: LY set-up

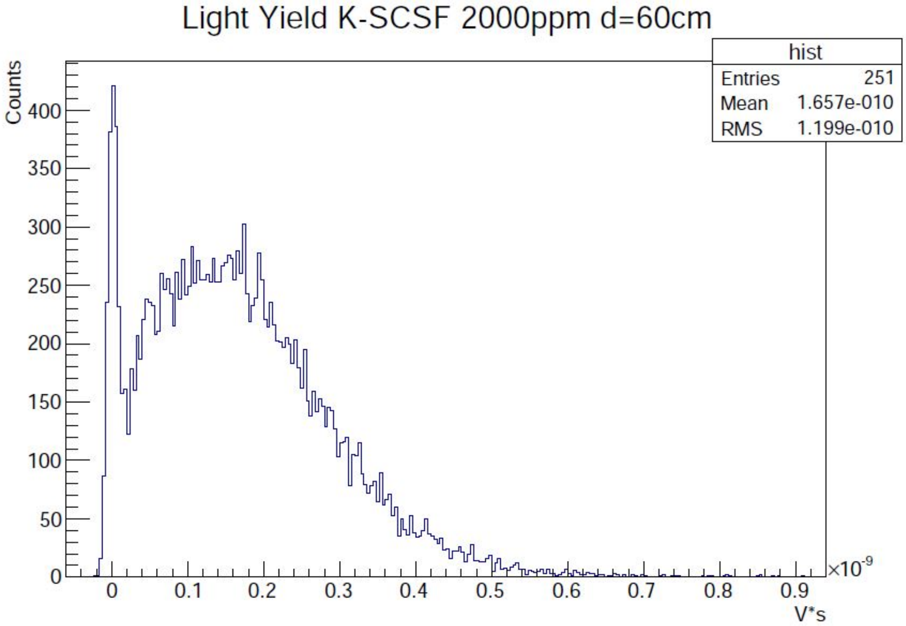

Figure 4.37: Example of a charge spectrum from a LY measurement: the pedestal peak is due to particles traversing the trigger fibres and not the signal fibres because of little misalignments.

$\langle N_{pe}\rangle$ free parameter of the model. The best fit of the theoretical curve with the experimental data will give $\langle N_{pe}\rangle$.

Centre Of Gravity (COG)

To obtain $\langle N_{pe}\rangle$ we eliminate the pedestal (made of zero counts), we calculate the spectrum's centre of gravity and we divide it by the 1 photoelectron gain G_{1pe}, previously measured and fixed (Q= charge):

$$\langle N_{pe}\rangle = \frac{\int Q \cdot Counts(Q)dQ}{\int Counts(Q)dQ} \cdot \frac{1}{G_{1pe}} \tag{4.11}$$

We add a linear correction to take in account the non-negligible signal under the pedestal.

The COG method for $\langle N_{pe}\rangle$ calculations is simple and sufficiently accurate for our two main purposes:

- Compare different fibres in terms of their LY.
- Definition of a threshold LY that every fibre spool must reach during the quality control before installation.

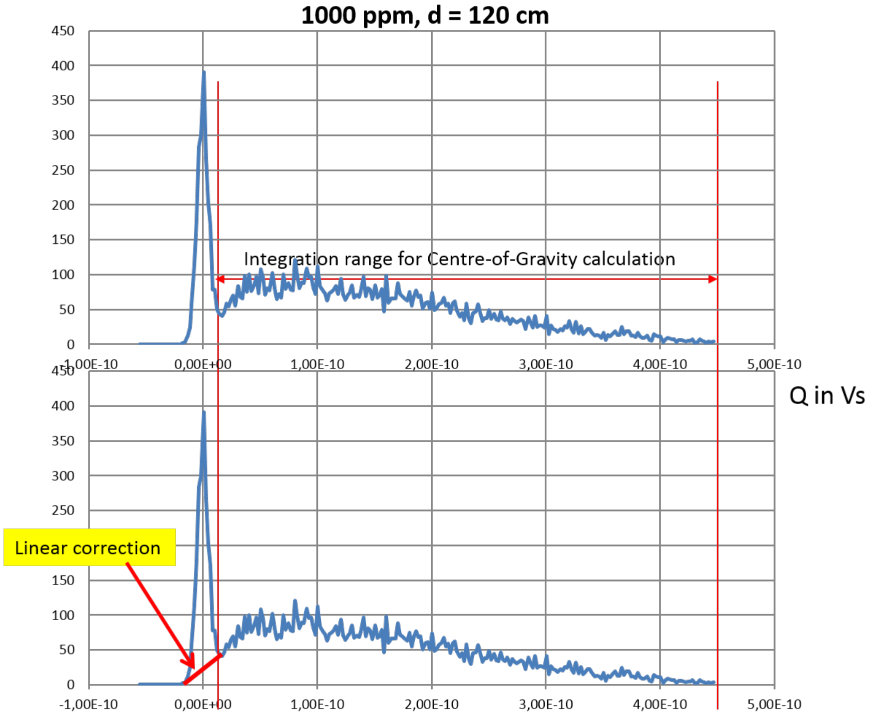

Figure 4.38: COG: range of calculation and linear correction for signal under pedestal.

This method is in any case still imprecise and is not describing any of the statistical processes involved in the generation of the final spectral shape. A more refined model is to be developed.

Statistical model

In the model we're now going to explain, we make some assumptions:

- The number of photons hitting the PMT's photocathode at every scintillation event is discrete and independent to the photons arrived in the previous event. Photons at the PMT's photocathode follow a Poisson law with $\langle N_{pe} \rangle$ as expected value [38, 39].
- Every discrete peak k in the spectrum, corresponding to a certain N_{pe} with relative height determined by the Poisson distribution $P(k, \langle N_{pe} \rangle)$, is widened due to electronic noise and assumes a Gaussian shape [39].
- Pedestal peak is a pure Gaussian coming from electronic noise: the Poisson contribution for $N_{pe} = 0$ is almost negligible.

The final spectrum is given by the sum of the shifting Gaussian distribution weighted by the Poissonian factors. Every Gaussian correspondent to the k-Poisson coefficient is centred at $k * G_{1pe}$. The standard deviation σ_k is given by:

$$\sigma_k = \sqrt{k * \sigma_{1pe}^2 + \sigma_{ped}^2} \tag{4.12}$$

where σ_{1pe}^2 is the intrinsic line widening measured in the 1pe calibration and σ_{ped}^2 is the pedestal peak's standard deviation representing a systematic noise due to the readout electronics(Fig. 4.34). The Gaussian functions are getting wider with increasing k since fluctuations in the electron multiplication through PMT increase with increasing incoming photons (conversion from N_{pe} to ADC channels); the overall SNR is anyway reduced when k is larger (SNR $\propto \sqrt{k}$).

A first fitting function $F(Q)$ could then be:

$$F(Q, \langle N_{pe} \rangle) = K \sum_{k=0}^{+\infty} P(k, \langle N_{pe} \rangle) \cdot G(Q, k \cdot G_{1pe}, \sigma_k) \tag{4.13}$$

This function doesn't take into any account the different paths that a particle can run through the fibres: N_{pe} must be higher for an electron passing through the centre of the signal fibres than tangent electrons just touching the non-scintillating cladding. We improve our model: $\langle N_{pe} \rangle$ is proportional to the electron's path length inside the fibre. Supposing a uniform spatial distribution for the electrons (uniform illumination) we have that the half path $L(x)$ inside the fibre of radius R (Fig. 4.39) is (considering just parallel electron's tracks) [38]:

$$L(x) = \sqrt{R^2 - x^2} \tag{4.14}$$

Adding this factor the fit function we obtain:

$$F^*(Q, \langle N_{pe} \rangle) = K^* \int_0^R \sum_{k=0}^{+\infty} P(k, L(x) \cdot \langle N_{pe} \rangle) \cdot G(Q, k \cdot G_{1pe}, \sigma_k) dx \tag{4.15}$$

where K^* is the new normalisation factor, automatically modified by the fit. F^* is the fit function we used as model in an implemented ROOT routine to calculate the best fit. We froze some fit parameters like the G_{1pe} and the σ_{1pe} to the measured values.

The fitting curve was still very imprecise, missing the fit especially in the low-charge part of the spectra (Fig. 4.40).

The reason of this missing fit has to be searched in the incomplete model function, that is describing a 1-fibre system, not including any correction for the 4-fibre geometry that we adopted. Two principle phenomena can explain this extra part of the spectrum:

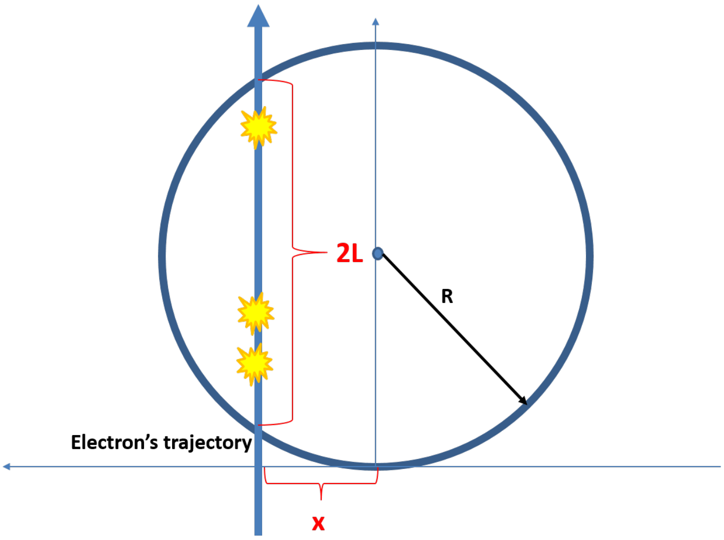

Figure 4.39: Electron's path inside the scintillating fibre

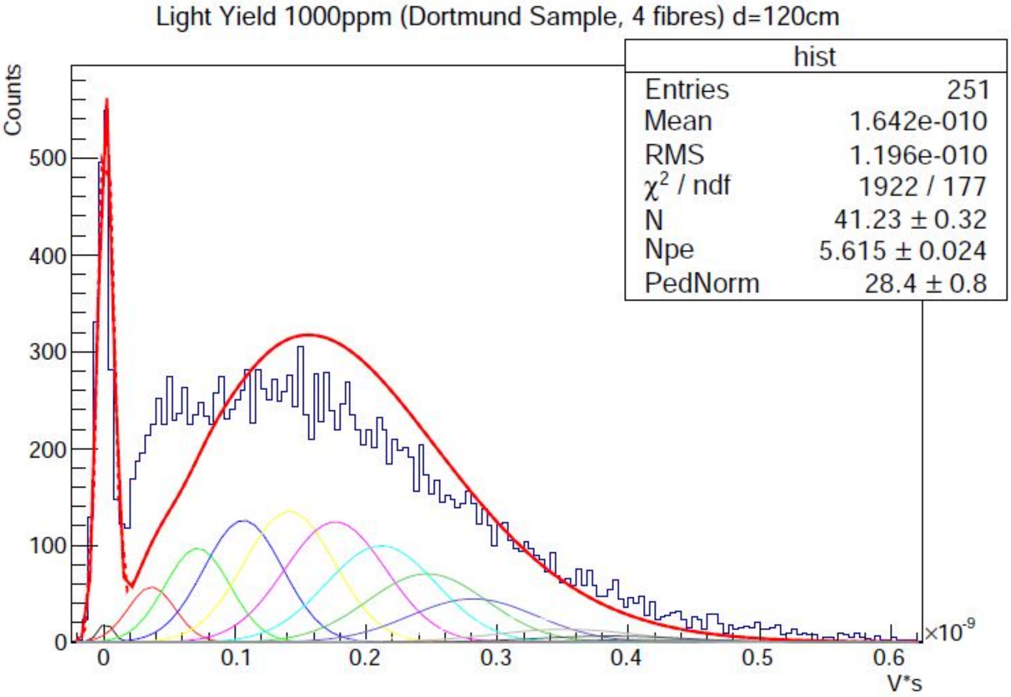

Figure 4.40: Charge spectrum with missed fit: the multicoloured curves under the spectrum represent the Gaussian functions. The sum of them gives the red fitting curve. We observe that the fit is underestimating the low photoelectrons contribution.

- Light leaking out from fibres, especially the cladding light responsible of the attenuation's fast component (helical modes), can be trapped by the next fibres if it satisfies the total internal reflection conditions (Fig. 4.41). This leads to some extra photons that, instead of being lost, are recuperated and become part of the spectrum. Even if we don't present any theoretical model for this phenomenon (almost impossible since fibres are rapidly entangled one to the other with high disorder in the winding disk), we can presume that it is affecting few photons. With the amount of light we normally have with 4 fibres ($\langle N_{pe} \rangle$ in the order of 6) it's probable that just 1 or 2 photons can escape from one fibre and be captured by another causing the extra photoelectrons in the low-charge region.

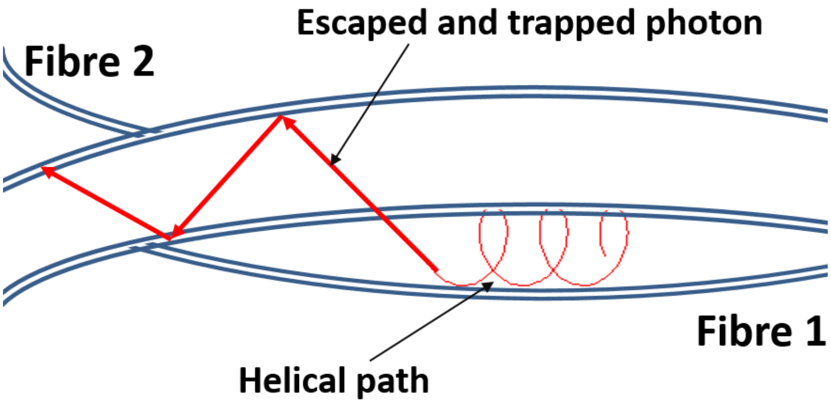

Figure 4.41: Twisted fibres: cladding light can pass from one fibre to the other

- Since the signal fibre trench is ≈ 0.270 mm wide, fibres can lye there partially misaligned. It can be that an electron is passing through the trigger fibres and just 1 or 2 signal fibres (Fig. 4.42): the relative weight of the low charge signal is going to be increased, explaining the impossibility for our model to correctly fit the spectrum, underestimating the low charge contribution.

To confirm this intuition we measured one-single-fibre's LY. We obtained lower signal and higher pedestals, but still possible to read and fit for short and medium distances (even up to 240cm for the 1000ppm Dortmund sample, the one with the highest LY, see the results section). Our model was perfectly able to fit the one-fibre experimental data (Fig. 4.43). We correctly remark that, if we multiply by 4 the LY obtained with the single-fibre measurement, we obtain slightly higher (≈ +10%) LY than what we get with the COG method from the 4 fibre measurement: the extra contributions for low charges

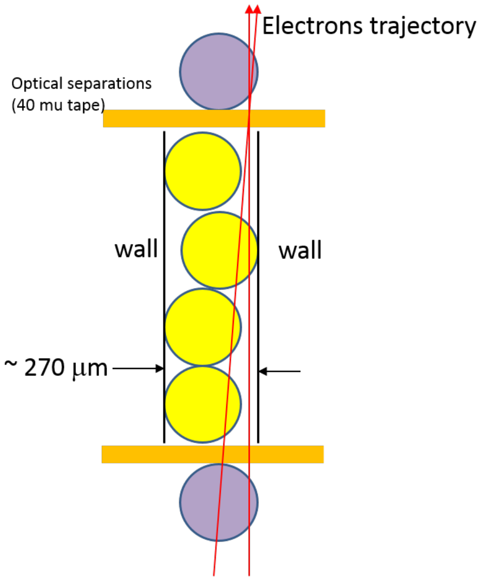

Figure 4.42: Fibres misalignment: some electrons that trigger the measurement could have not traversed all the signal fibres

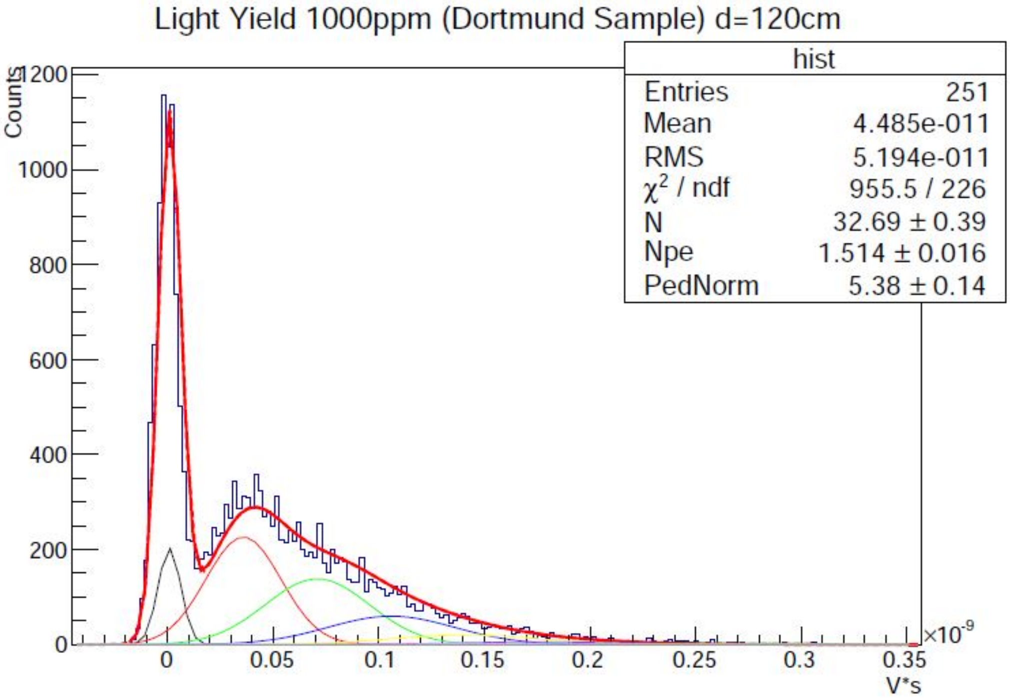

Figure 4.43: LY spectrum for one-single-fibre measurement: the ROOT routine can precisely fit the curve.

shift the spectrum's COG to the low photoelectrons.
In the further section, where we're going to discuss the results, we prefered the COG method to obtain $\langle N_{pe}\rangle$: the error made by overestimating low photoelectrons seems to be stable for all distances (Fig. 4.44) and therefore it doesn't affect a relative measurement between different fibres. On the other hand, COG allows signals of sufficient intensity at every distance even for the worst fibres in terms of LY thanks to the 4 fibres.

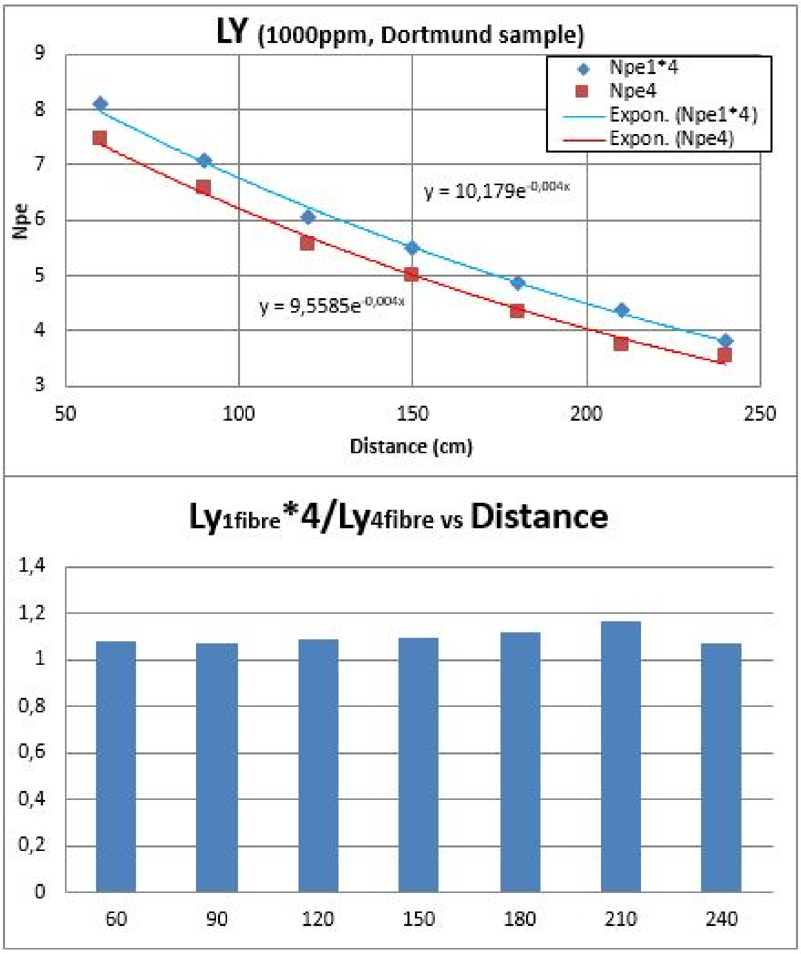

Figure 4.44: Compared LY SCSF78 1000ppm (Dortmund spool). The blue points represent $4 * LY_{1Fibre}$,$\langle N_{pe}\rangle$ extracted by the ROOT fit; red points represent LY_{4Fibre},$\langle N_{pe}\rangle$ extracted with the COG method

4.4.4 Results

The LY experimental set-up gives clear signals and reliable spectra. The geometrical stability guarantees sufficient reproducibility (tested in the range ±5%).

We measured and characterised our entire set of fibres: Kuraray SCSF78 with WLS concentrations of 500ppm, 1000ppm, 2000ppm, 5000ppm. LY was measured for every fibre at different distances detector-excitation: 60cm, 90cm, 120cm, 150cm.

We measured two samples for the 1000ppm coming from different spools: the first produced in 2010 and coming from Dortmund University (the so called *Dortmund Spool*), the other produced in Summer 2014. Since 1000ppm is the Kuraray standard and the fibre which was showing the best attenuation length, we measured the two 1000ppm even at 180cm, 210cm and 240cm. The final compared plot is presented in Fig. 4.45. One can see that, despite to some indications from Kuraray suggesting that a higher WLS concentration could significantly increase the LY, the 2000ppm and 5000ppm fibres show more or less the same LY, if not lower, as the 500 and the 1000ppm

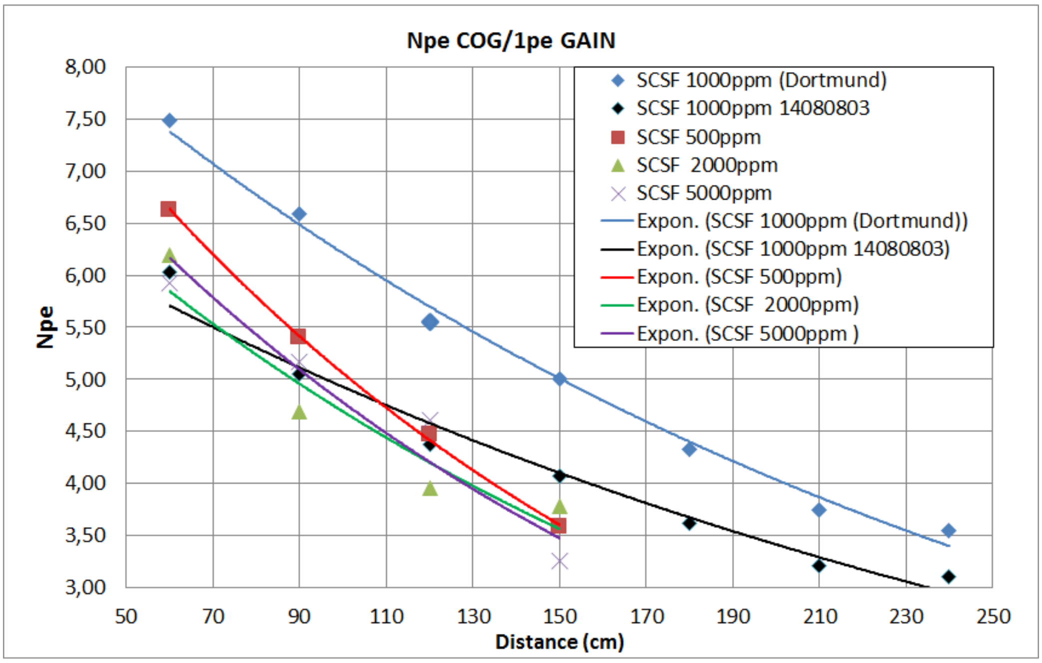

Figure 4.45: Final Compared LY results

(2014 batch). The Dortmund spool confirms itself as an exceptional sample, with LY 15-20% higher at every distance. Kuraray explains that technology for high WLS concentrations in 0.25mm fibres is not mature but still in a development phase; their suggestions were based on what experimented with 1mm fibres.

For the time being we can conclude that there is no reason to modify the Kuraray standard 1000ppm which, even if not exalting in 2014 as it was in the Dortmund spool, still shows the highest LY at 150cm (combination LY-attenuation length).

In terms of hardware equipment, the work successfully carried out to build the LY experimental set-up will stay and work permanently for the whole procurement phase (end 2016). One could try to introduce improvements in the theoretical model or study a solution for one fibre measurements.

4.5 Next R&D steps for Scintillating Fibres

Last part of 2014 will still be focused on R&D for scintillating fibres. CERN will stay as the most important research centre in charge of fibres for the LHCb SciFi tracker, helped principally by Dortmund and Aachen Universities.

The next aspect to be investigated will concern mirrors. Mirrors are to be installed at the end of every submodule of 2.5m height, corresponding to the coordinate y=0 (see Fig. 1.4 and 2.1). Light during scintillation is produced isotropically over 4π and just half of it will propagate in the SiPM direction: signal coming from events on the beam pipe's plane will be doubled thanks to good mirrors. Up to now, three mirror technologies compete:

- Aluminized Mylar
- Aluminium Thin Film Coating (Al TFC)
- Enhanced Specular Reflector (ESR)

Mirrors from every technology will be grown on test plates with glued fibres and reflectivity tests will be performed.

Fibre's geometry, especially diameter's profile, will also be a major point of interest. A laser-based machine for fibre's diameter profiling has already been built in Aachen. CERN is building a similar machine to discover diameter bumps (diameter > 0.3mm) and store their position in the spool. If the bumps' position in the spool is known, while de-winding it during fibre mats assembling, (Fig. 2.7) the bumped fibre pieces can be recognised, cut away and the necessary precision maintained.

For the end of the year every detail must have been discussed: fibre typology, mirror technology and glue to be used in mats are to be definitely decided. How LY, attenuation length and diameter profile will be checked will be defined in a quality protocol. At the beginning of 2015 the final design must be clear and definitive to let the procurement phase begin.

Chapter 5

Conclusions and Prospects

Some remarkable results were obtained and presented in this work. They are here summarised:

- An experimental set-up was built to provide Dark Count Rate, Cross-Talk and Gain measurements for SiPM; Matlab codes were written to analyse and interpret data. We found that the new KETEK technology mostly fulfilled CERN's requests on SiPMs.

- We used an existing set-up to perform several Photo-Detection Efficiency measurements on KETEK SiPMs. The new devices increased the peak PDE but still don't match perfectly fibre's emission spectrum.

- An experimental set-up was built to obtain a Temperature characterisation for SiPMs. The breakdown voltage's shift as well as the noise reduction with T was documented and quantified. KETEK devices show a satisfying noise reduction at low Temperatures.

- We improved the hardware of an existing set-up for fibre's attenuation lengths measurements and made it more automatic. We developed a Labview routine to provide rapid measurements and immediate fits for attenuation lengths. We measured that attenuation length is slightly decreasing with higher WLS concentrations.

- We built an experimental set-up for emission and absorption spectra measurements. We wrote several Excel sheets for data analysis and plots. We showed that blue and UV light is rapidly attenuated in scintillating fibres and that the output spectrum shifts towards green and red when the excitation is far form detection. We measured clear fibre's absorption spectrum to investigate the spectral response of pure Polystyrene.

- We built an experimental set-up for Light Yield measurements using a ^{90}Sr source and an electron monochromator. We designed and realised high precision mechanical pieces for fibre positioning. We designed and developed a trigger system as well as control circuits for PMT photodetectors. We developed a theoretical model to interpret charge spectrum obtained with LY measurements. We wrote a ROOT program to fit the model with experimental data. We found that LY is not increasing with higher WLS concentration and that fibre's production quality is not stable in time.

The work carried out on SiPM was useful and presented in several meetings. Our results were directly discussed in Munich with KETEK; the software and hardware developed at CERN will anyway not be constantly used in the next years, since EPFL took in charge the SiPM side of the LHCb SciFi Tracker project.

All the work carried out at CERN concerning fibres has been presented during meetings, conferences (especially during the LHCb week in Orsay, 15-19 September 2014) and described in official internal documents. This work remains: experimental set-ups especially will stay mounted and operational: they will be usefully used in the next years; the ROOT fitting routine and the Labview program will be constantly running in the quality control phase.

Bibliography

[1] Wikipedia, CERN page.

[2] "Why the LHC". CERN. 2008. Retrieved 2009-09-28.

[3] G. F. Giudice, A Zeptospace Odyssey: A Journey into the Physics of the LHC, Oxford University Press, Oxford 2010, ISBN 978-0-19-958191-71.

[4] (EN) LHCb Collaboration, The LHCb Detector at the LHC in Journal of Instrumentation, vol. 3, n° 8, 2008, pp. S08005, DOI:10.1088/1748-0221/3/08/S08005.

[5] P.R. Barbosa-Marinho et al., LHCb VELO, VErtex LOcator: Technical Design Report. Technical Design Report LHCb. CERN, Geneva, 2001

[6] S. Amato et al., LHCb magnet: Technical Design Report Technical Design Report LHCb. CERN, Geneva, 2000

[7] A. Pickford, The RICH system of the LHCbexperiment: status and performance, Nucl. Instrum. Methods Phys. Res. A 604(12), 297 (2009)

[8] S. Amato et al., LHCb calorimeters: Technical Design Report. Technical Design Report LHCb. CERN, Geneva, 2000

[9] P.R Barbosa-Marinho et al., LHCb muon system: Technical Design Report. Technical Design Report LHCb. CERN, Geneva, 2001

[10] LHCb Tracker, Technical Design Report. LHCb collaboration. CERN/LHCC 2014-001 LHCb TDR 15, 12th February 2014. Chapter 3.1.

[11] LHCb Tracker, Technical Design Report. LHCb collaboration. CERN/LHCC 2014-001 LHCb TDR 15, 12th February 2014. Chapter 3.2.

[12] G. Battistoni et al., The FLUKA code: Description and benchmarking, in Proceedings of the Hadronic Shower Simulation Workshop 2006 (M. Albrow and R. Raja, eds.), AIP Conference Proceeding 896, pp. 3149, 2007.

[13] A. Fasso et al., FLUKA: a multi-particle transport code, 2005. CERN-2005-10, INFN/TC05/11, SLAC-R-773.

[14] N. Lopez March and M. Karacson, Radiation studies for the LHCb tracker upgrade, LHCb-INT-2013-003. Public note in preparation.

[15] LHCb Tracker, Technical Design Report. LHCb collaboration. CERN/LHCC 2014-001 LHCb TDR 15, 12th February 2014. Chapter 3.3: Layout of the Scintillating Fibre Tracker.

[16] C. Joram, Technical specications of the scintillating fibres, LHCb-INT-2013-061. Public note in preparation.

[17] KETEK GmbH, Hofer Str. 3, 81737 Muenchen, Germany.

[18] KETEK SiPM. SiPM technology. Official webpage.

[19] Hamamatsu Photonics K.K., 325-6, Sunayama-cho, Naka-ku, Hamamatsu City, Shizuoka Pref., 430-8587, Japan.

[20] Y. Musienko, State of the art in SiPMs, Feb, 2011. Talk given at Industry-academia matching event on SiPM and related technologies.

[21] LHCb Tracker, Technical Design Report. LHCb collaboration. CERN/LHCC 2014-001 LHCb TDR 15, 12th February 2014. Chapter 3.4: Scintillating Fibres.

[22] LHCb Tracker, Technical Design Report. LHCb collaboration. CERN/LHCC 2014-001 LHCb TDR 15, 12th February 2014. Chapter 3.5: Silicon Photodetectors.

[23] C. Joram and E. Gushchin, Comparative Measurements of the Photon Detection Efficiency of KETEK SiPM Detectors for the LHCb SciFi Upgrade Project, LHCb-INT-2013-062.

[24] Kuraray Co., Ltd., Ote Center Building, 1-1-3, Otemachi, Chiyoda-ku, Tokyo 100-8115, Japan

[25] K. C. Ltd., Kuraray Plastic Scintillating Fibres, 2014. Official web page.

[26] T. White, Scintillating fibres, Nuclear Instruments and Methods in Physics Research Section A: Accelerators, Spectrometers, Detectors and Associated Equipment 273 (1988), no. 23 820.

[27] A.E. Baulin, Y.cao, A.E. Baulin, Y. Cao, J. Chan, B.P. Giesbrecht, A.K. Heinrichs, S. Katsaganis, D. Kolybaba, S.T. Krueger, B.D. Leverington, T. Li, M.J. Litzenberger, G.J. Lolos, Z. Papandreou, E.L. Plummer, H. Qian, M.D. Sauder, A.Yu. Semenov, I.A. Semenova ,L.M. Sichello, Y. Sun, L.A. Teigrob, K. Vuthitanachot, A.M. Watson, Y. Yongzhe. Attenuation length and spectral response of Kuraray SCSF-78MJ scintillating fibres. Nuclear Instruments and Methods in Physics Research A 715 (2013) 48-55.

[28] R. C. Ruchti, THE USE OF SCINTILLATING FIBERS FOR CHARGED- PARTICLE TRACKING, Annual Review of Nuclear and Particle Science 46 (1996), no. 1 281.

[29] K. Wyllie et al., Electronics Architecture of the LHCb upgrade, LHCb-2011-011.

[30] S. G. Ceramics and P. Inc., Saint Gobain Scintillating Fibres, 2014. Official webpage.

[31] N. Lopez March and M. Karacson, Radiation studies for the LHCb tracker upgrade, LHCb-INT-2013-003. Public note in preparation.

[32] C. Zorn, A pedestrian's guide to radiation damage in plastic scintillators, Nuclear Physics B - Proceedings Supplements 32 (1993), no. 0 377.

[33] K. Hara et al., Radiation hardness and mechanical durability of Kuraray optical fibers, Nucl. Instr. Meth. A411 (1998), no. 1 31 .

[34] S. Bruggisser, Literature study on the radiation damage on KURARAY fibers,https://twiki.cern.ch/twiki/pub/LHCb/ScintFiber/FiberSummaryNew.pdf, September, 2012.

[35] B. Leverington, C. Joram, and S. Baker, Scintillating Fibre Irradiation with 22.9 MeV Protons, Tech. Rep. LHCb-INT-2014-002. CERN-LHCb-INT-2014-002, CERN, Geneva, Jan, 2014. Public note in preparation.

[36] C. Joram et al., Measurements and radiation tests on scintillating fibres for the LHCb SciFi project, LHCb-INT-2013-002. Public note in preparation.

[37] S. Arfaoui, C. Joram, C. Casella, E. van der Kraaij: Characterisation of an 90Sr based electron monochromator. CERN-INT.

[38] C.M. Hawkes, M. Kuhlen, B. Milliken., R. Stroynowski and E. Wicklund: California Institute of Technology; T. Shimizu and O. Shinji: Kuraray. Nuclear Instruments and Methods in Physics Research A292 (1990) 329-336.

[39] T.D. Beattie, A.P. Fisher, S.T. Krueger, G.J. Lolos, Z. Papandreou, E.L. Plummer, A. Yu. Semenov, I.A. Semenova, L.M. Sichello, L.A. Teigrob, E.S. Smith. Light Yield of Kuraray SCSF-78Mj scintillating fibers for the GlueX Barrel Calorimeter. Public note in preparation.